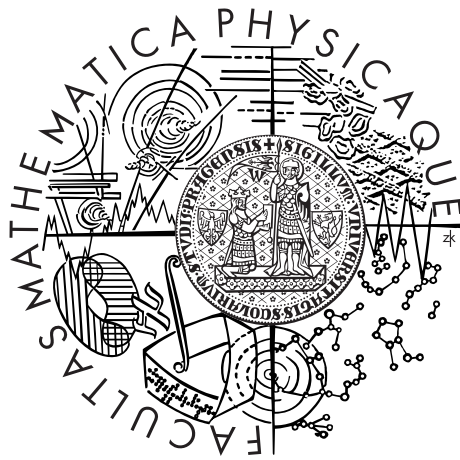


Charles University in Prague
Faculty of Mathematics and Physics

DOCTORAL THESIS



PAVOL JUSKO

NEGATIVE ION ASTROCHEMISTRY – A LABORATORY STUDY

Department of Surface and Plasma Science
Supervisor of the doctoral thesis: Prof. RNDr. Juraj Glosík, DrSc.
Study programme: Physics
Study branch: Physics of Plasmas and Ionized Media

« *C'est le temps que tu as perdu pour ta rose
qui fait ta rose si importante.* »

— *Le Renard*

ACKNOWLEDGMENTS

The presented work would not have been possible without the cooperation of my colleagues, namely Petr Dohnal, Michal Hejduk, Tomáš Kotrík, Dmytro Mulin, Peter Rubovič, Jozef Varju, and Illia Zymak under the excellent supervision of Radek Plašil and especially prof. Juraj Glosík. My special thanks also goes to Štěpán Roučka for all the time he has spent working on and thinking about the experiments. I sincerely thank all of you.

From people outside the Charles University I would like to thank prof. Dieter Gerlich¹ for introducing me into the field of rf particle trapping and for endless fruitful discussions.

I also thank Dr. Holger Kreckel² for giving me the opportunity to stay at the Max-Planck-Institut für Kernphysik and acquire new knowledge.

Na záver, ale o to viac, by som chcel pod'akovať všetkým mojim priateľom a mojej rodine, za ich všestrannú pomoc a podporu počas mojich štúdií.

¹ Member of Faculty of Natural Science, Technical University, Reichenhainer Straße 70, Chemnitz, Germany

² Member of Max-Planck-Institut für Kernphysik, Saupfercheckweg 1, Heidelberg, Germany

DECLARATION

I declare that I carried out this doctoral thesis independently, and only with the cited sources, literature and other professional sources.

I understand that my work relates to the rights and obligations under the Act No. 121/2000 Coll., the Copyright Act, as amended, in particular the fact that the Charles University in Prague has the right to conclude a license agreement on the use of this work as a school work pursuant to Section 60 paragraph 1 of the Copyright Act.

Prague, June 2013

Pavol Jusko

ABSTRAKT

NÁZOV PRÁCE: Astrochémia negatívnych iónov – Laboratórne štúdium

AUTOR: Pavol Jusko

VEDÚCI DOKTORSKEJ PRÁCE: Prof. RNDr. Juraj Glosík, DrSc.

ABSTRAKT: Predložená práca sa zaoberá experimentálnym štúdiom interakcie aniónov s neutrálnymi časticami pri teplotách relevantných pre astrofyziku. Zaoberali sme sa aniónom H^- , dôležitým pri tvorbe molekulárneho vodíka a aniónom O^- , ako možným zdrojom vody. Určili sme teplotnú závislosť rýchlostného koeficientu reakcie v rozmedzí teplôt 10 až 150 K pre reakcie $H^- + H \rightarrow H_2 + e^-$ a $O^- + H_2 \rightarrow H_2O + e^-$. Získali sme rozdelenie energií elektrónov produkovaných v druhej z menovaných reakcií pri teplote 300 K. Merania prebiehali na dvoch experimentálnych zariadeniach, v práci uvádzame ich princíp činnosti, konštrukciu, kalibráciu a podporné merania.

KLÚČOVÉ SLOVÁ: anióny, iónové pasce, astrochémia, asociatívne odtrhnutie

ABSTRACT

TITLE: Negative ion astrochemistry – A laboratory study

AUTHOR: Pavol Jusko

SUPERVISOR: Prof. RNDr. Juraj Glosík, DrSc.

ABSTRACT: Presented work focuses on experimental study of anion interaction with neutral particles at temperatures relevant for astrophysics. Anion H^- , important for molecular hydrogen creation, and O^- as a possible source of water are investigated. The temperature dependence of reaction rate coefficients from 10 to 150 K for reactions $H^- + H \rightarrow H_2 + e^-$ and $O^- + H_2 \rightarrow H_2O + e^-$ has been determined. The energy distribution of electrons produced in the latter reaction at 300 K has also been acquired. These studies have been performed on two experimental setups, which are presented together with the theory of operation, construction details, calibration, and supporting test measurements.

KEYWORDS: anions, ion traps, astrochemistry, associative detachment

CONTENTS

1	INTRODUCTION	1
1.1	Goals of the thesis	2
2	MOTION OF CHARGED PARTICLES	3
2.1	Homogeneous fields ($B \neq 0$)	3
2.1.1	$E = 0$	4
2.1.2	Finite E	4
2.1.3	Motion in $\nabla B \parallel B$ field and the magnetic moment μ	5
2.2	Magnetic mirror trap	8
2.3	Charged particles in electrostatic fields	9
2.3.1	Laplace equation	10
2.4	Charged particles in radio frequency fields	10
2.4.1	Adiabatic approximation	10
2.4.2	Effective potential V^*	11
2.4.3	Linear Multipoles	13
3	EXPERIMENTAL TECHNIQUES	17
3.1	Charged particle production	17
3.2	Particle detectors	19
3.3	H atom source	21
3.3.1	Theory of operation	21
3.3.2	Atomic beam velocity distribution	23
3.3.3	Determining the beam density in the trap	24
3.4	Reaction temperature	26
3.4.1	Thermometer for low temperature ions	27
3.4.2	Collision temperature for particles with different T	29
4	THE REACTION RATE COEFFICIENTS	31
4.1	The 22-pole trap apparatus	31
4.2	The $H^- + H$ system	33
4.2.1	Role of H^- in primordial astrochemistry	33
4.2.2	Determining the rate coefficient using the 22-pole trap	34
4.2.3	Comparison with theoretical calculations and previous measurements	38
4.3	Reaction of atomic oxygen anion with H_2 – water production	39
4.3.1	Comparison with previous measurements	43
4.3.2	The isotope effect	43

4.4	Is formation of H_3^-/D_3^- possible in the 22-pole trap?	44
5	ASSOCIATIVE DETACHMENT AND THE ELECTRON SPECTRA	47
5.1	Associative detachment	47
5.2	Theory of operation	48
5.2.1	MAC-E filter	49
5.2.2	Radiofrequency ion trap	51
5.3	Experimental setup	52
5.3.1	Thermionic emission as electron source	54
5.3.2	Anion photodetachment	58
5.3.3	Spectra of the photodetached electrons	61
5.4	Experimental results	62
5.4.1	Reaction rate coefficient	62
5.4.2	Energy distribution of detached electrons	65
5.5	Discussion	67
5.5.1	Improvements of the ES-MPT apparatus	67
5.5.2	Electrons produced in AD	69
6	FINAL REMARKS	71
I	APPENDIX	73
A	CAD DRAWINGS	75
B	ELECTRON AFFINITIES	77
C	SCRIPTS FOR EFFECTIVE POTENTIAL V^*	79
	BIBLIOGRAPHY	81
	LIST OF PUBLICATIONS	89
	LIST OF FIGURES	91
	LIST OF TABLES	92
	LISTINGS	93
	ACRONYMS	93
II	ATTACHED ARTICLES	95
	ARTICLE I	97
	ARTICLE II	105

NOMENCLATURE

Constants and scalar variables are written in italic (c , E , V , φ), vectors are written in bold (\mathbf{v} , \mathbf{F} , \mathbf{B}). Vector magnitude is usually written in italic variant of the corresponding symbol (v , F , B), occasionally notation $|\mathbf{v}|$ is used. Unit vectors are written with hats (e.g. \hat{x} , \hat{y} , \hat{z}). Dot notation is used for time derivation, e.g. $\mathbf{v} = \dot{\mathbf{x}}$, $\mathbf{a} = \dot{\mathbf{v}}$. Angle brackets $\langle \rangle$ are used for averaging. The number density is denoted using square brackets, e.g. $[H_2]$, $[D_2]$. Some common symbols used through the text, with their usual meaning, are listed below.

\mathbf{r}	radius vector
\mathbf{v}	velocity vector
v_{\perp}	velocity component perpendicular to \mathbf{B}
v_{\parallel}	velocity component parallel to \mathbf{B}
E	energy
E_{\perp}	energy associated with perpendicular motion
E_{\parallel}	energy associated with parallel motion
\mathbf{E}	electric field
\mathbf{B}	magnetic field
V_0	rf amplitude
U_0	DC potential
Ω	rf angular frequency
V^*	effective potential
Ω_c	cyclotron frequency
r_L	Larmor radius
T	temperature
q	electric charge
m	mass
u	atomic mass unit

INTRODUCTION

Astronomical observations of various particles in space have been done for several decades. Presence of the molecules from simple diatomic gases up to the fullerenes and PAHs (Polycyclic Aromatic Hydrocarbons) together with positive ions have been confirmed. However, the existence of negative ions in interstellar medium have not been confirmed by direct detection before the observation of C_6H^- done by McCarthy et al. (2006). Since then, several other carbon containing anions have been spectroscopically detected (Agúndez et al., 2010). These anions have high electron binding energy (higher than 2 eV) and are relatively easy identifiable in visible and infrared spectrum. The simplest anion H^- has not been identified directly yet, though transitions in the ultraviolet region exist (Ross et al., 2008).

With current availability of high precision spectroscopic measurements from instruments like the Herschel¹ telescope or the ALMA² observatory, the amount of data regarding the molecular composition of interstellar medium is increasing. In order to understand the processes taking place in such medium, with widely varying composition and temperature in its sub-domains, laboratory experiments are needed.

As an example of importance of accurate reaction properties knowledge the abundances of H_2 during the star formation in the early universe are discussed. According to Glover et al. (2006), the molecular hydrogen plays an important role in the cooling process of the primordial gas, almost exclusively composed of atomic hydrogen. If the cooling process is efficient enough, collapse of the primordial medium leads to protostellar formation. Different processes leading to the formation of H_2 have been studied by numerical modeling. The conclusion from the models was shown to be strongly dependent on the reaction rate coefficients used. Glover et al. (2006) shows that especially the uncertainties of rate coefficient of associative detachment of $H^- + H \rightarrow H_2$ influences the outcome of the model by several orders of magnitude. The discrepancy influence between the reaction rate coefficients has

¹ <http://www.sci.esa.int/herschel/>

² <http://www.almaobservatory.org/>

been resolved only recently by accurate laboratory measurement of the associative detachment by Kreckel et al. (2010).

This work is divided into chapters according to the topics. The chapter 2 deals with theoretical description of charged particle motion and methods of confinement using magnetic and electric fields in different configurations. In chapter 3 we describe experimental techniques in more detail from the practical point of view and show supplementary measurements proving the conditions attained in the actual measurement. Chapter 4 is devoted to the reaction rate coefficient measurements. Reactions involving H^- and O^- with molecular hydrogen/deuterium and atomic hydrogen at temperatures ranging from 10 K to 300 K are investigated. In chapter 5 we present a newly designed instrument for electron energy determination. Electrons are produced in the associative detachment of O^- with H_2 , D_2 , and CO .

1.1 GOALS OF THE THESIS

The focus of this work is experimental determination of temperature dependent reaction rate coefficients, which are needed to understand the complicated astrochemical reaction networks. Electron energy distribution of electrons produced in associative detachment has also been investigated in order to understand the distribution of energy released in the reaction. It is important to note that experiments presented need at least one charged particle as a reactant because of ease of trapping, guiding, and detection. Neutral-neutral experiments, though possible, are out of the scope of this work.

The main topics of the thesis are:

- Experimental investigation of reaction rate coefficients for ion-molecule reactions of H^- and O^- anions.
- Design, construction, and calibration of the new instrument for investigation of energy distribution of electrons produced in the associative detachment.

MOTION OF CHARGED PARTICLES

Accurate description of motion of objects in any given system is of fundamental importance for estimation of its behaviour. In general, this is a difficult task neither solvable analytically nor using computer modeling in situations with many elementary particles. Situation becomes even more complicated if inter-particle interactions are considered.

We are going to focus on conditions important for understanding processes appearing in this work, especially:

- Number density of charged particles is low. We assume that particle charge is negligible and does not alter externally introduced fields.
- Particles are slow, i. e., non relativistic.

Single particles are going to be immersed in different field configurations and analytical description of resulting motion is going to be explained. Since our experiments make use of geometries where particles are stored for long time, special emphasis is going to be given to traps and confinement.

If further interested, the reader is also strongly encouraged to take a look in the publications written by Chen (1974) and by Kivelson and Russell (1995) for charged particles (plasmas) in general, and by Gerlich (1992) and by Ghosh (1995) for particle confinement.

2.1 HOMOGENEOUS FIELDS ($B \neq 0$)

As we stated earlier, we are going to focus on describing the behaviour of charged particles. We immediately see that electrical and magnetic forces play significant role in equations describing the motion system.

Let us consider a particle with mass m and charge q moving with velocity \mathbf{v} in an environment consisting of magnetic field \mathbf{B} and electric field \mathbf{E} . The particle experiences the Lorentz force \mathbf{F}_L

$$\mathbf{F}_L = q\mathbf{E} + q\mathbf{v} \times \mathbf{B}. \quad (1)$$

In combination with first Newton law for balance of linear momentum of such particle we derive

$$m \frac{d\mathbf{v}}{dt} = \mathbf{F}_L + \mathbf{F}_G = q\mathbf{E} + q\mathbf{v} \times \mathbf{B} + \mathbf{F}_G, \quad (2)$$

where we introduce nonelectromagnetic forces \mathbf{F}_G (e. g. gravitational force). We immediately make an assumption that nonelectromagnetic forces are negligible $\mathbf{F}_G = 0$.

2.1.1 $\mathbf{E} = 0$

Let us solve the equation (2) in magnetic field only (i. e., $\mathbf{E} = 0$). Without the loss of generality, we assume that $\mathbf{B} = |\mathbf{B}|$ is along the \mathbf{z} axis

$$m\dot{v}_x = qBv_y, \quad m\dot{v}_y = -qBv_x, \quad m\dot{v}_z = 0,$$

$$\ddot{v}_x = \frac{qB}{m}\dot{v}_y = -\left(\frac{qB}{m}\right)^2 v_x, \quad \ddot{v}_y = -\frac{qB}{m}\dot{v}_x = -\left(\frac{qB}{m}\right)^2 v_y. \quad (3)$$

Equation (3) implies circular motion in clockwise direction for $q > 0$ and counterclockwise direction for $q < 0$

$$x = -i\frac{v_\perp}{\Omega_c}e^{i\Omega_c t}, \quad y = \pm\frac{v_\perp}{\Omega_c}e^{i\Omega_c t}, \quad (4)$$

where we introduce v_\perp , which is a component of \mathbf{v} perpendicular to \mathbf{B} and an angular frequency

$$\Omega_c = \frac{|q|B}{m}, \quad (5)$$

which is called cyclotron or gyro-frequency.

In equation (4) one can immediately identify the radius of such rotation, which is called Larmor or gyro-radius

$$r_L = \frac{v_\perp}{\Omega_c} = \frac{mv_\perp}{|q|B}. \quad (6)$$

It is important to note that cyclotron motion does not change the kinetic energy of the gyrating particle (from equation (2))

$$\frac{d\left(\frac{1}{2}mv^2\right)}{dt} = q\mathbf{v} \cdot (\mathbf{v} \times \mathbf{B}) = 0. \quad (7)$$

2.1.2 Finite \mathbf{E}

Let us add finite electric field intensity \mathbf{E} into our system. The resulting motion is going to be a superposition of the cyclotron motion and the drift of gyration center. For simplicity, but without the loss of generality, we assume that $\mathbf{E} = |\mathbf{E}|$ is oriented along the \mathbf{x} axis ($E_y = E_z = 0$).

To get the feel of Ω_c , for e^- in $B = 1 \text{ mT}$ cyclotron frequency is $\Omega_c = 1.8 \cdot 10^8 \text{ rad.s}^{-1} \dots$

\dots and with energy of 1 eV Larmor radius $r_L = 3 \text{ mm}$

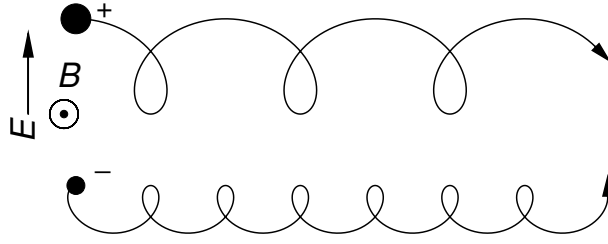


Figure 1: Motion of charged particle in nonzero homogenous perpendicular electric and magnetic field. \mathbf{E} is perpendicular to \mathbf{B} .

In this case, the velocity in z direction is again not coupled with the x, y directions (figure 1).

The equation of motion (1) can be written as

$$m \frac{d\mathbf{v}}{dt} = q (\mathbf{E} + \mathbf{v} \times \mathbf{B}), \quad (8)$$

in components

$$\begin{aligned} m \frac{dv_x}{dt} &= \frac{q}{m} E_x \pm \Omega_c v_y, \\ m \frac{dv_y}{dt} &= \mp \Omega_c v_x, \\ m \frac{dv_z}{dt} &= 0. \end{aligned} \quad (9)$$

For constant E

$$\begin{aligned} \frac{d^2}{dt^2} v_x &= -\Omega_c^2 v_x, \\ \frac{d^2}{dt^2} \left(v_y + \frac{E_x}{B} \right) &= -\Omega_c^2 \left(v_y + \frac{E_x}{B} \right). \end{aligned} \quad (10)$$

After substituting $v_y + \frac{E_x}{B}$ by v_y , we have the previous case and equation (3) can be rewritten as

$$\begin{aligned} v_x &= v_{\perp} e^{i\Omega_c t}, \\ v_y &= \pm v_{\perp} e^{i\Omega_c t} - \frac{E_x}{B}, \end{aligned} \quad (11)$$

where the Larmor motion is the same as in section 2.1.1 and for non zero E_x a drift velocity in the y direction appears.

2.1.3 Motion in $\nabla B \parallel B$ field and the magnetic moment μ

We are going to discuss one special non homogenous magnetic configuration shown in figure 2. The magnetic field is oriented along the

z axis in cylindrical coordinates r, z, θ and its intensity is changing (i. e., gradient in this direction is non zero). Such configuration is easily created using two coils (black outlined rectangles, upper panel in figure 2) with different diameter or current density.

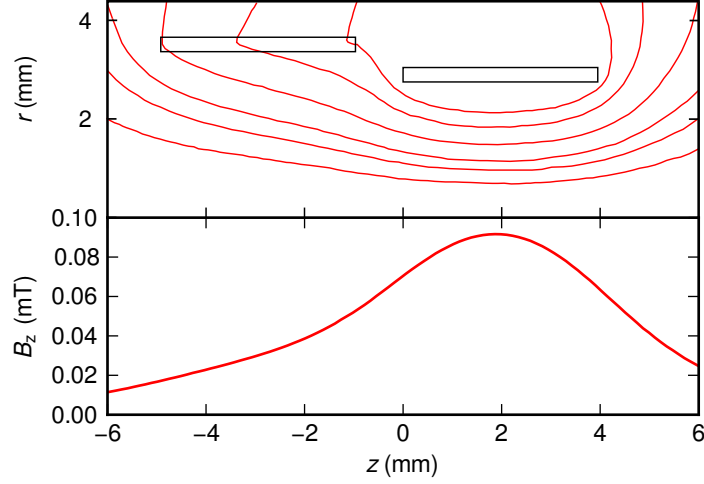


Figure 2: Magnetic field $\nabla \mathbf{B} \parallel \mathbf{B}$. Two current coils are used to produce the desired magnetic field. Upper panel shows the rotationally symmetric configuration in cylindrical coordinates ($r, z, \theta = 0$) together with magnetic field lines. Black outlined rectangles represent current coils. Lower panel shows the B_z field component on the z axis.

Since our setup is rotationally symmetric along the z axis $B_\theta = 0$ and all $\frac{\partial}{\partial \theta} = 0$. Gauss's law for magnetism states that $\nabla \cdot \mathbf{B} = 0$ which in cylindrical coordinates leads to

$$\frac{1}{r} \frac{\partial}{\partial r} (rB_r) + \frac{\partial B_z}{\partial z} = 0. \quad (12)$$

Assuming the $\nabla \mathbf{B}$ in z direction for $r = 0$ is known and only slowly varying the equation (12) can be rewritten as

$$\begin{aligned} rB_r &= - \int_0^r r \frac{\partial B_z}{\partial z} dr = - \frac{1}{2} r^2 \left| \frac{\partial B_z}{\partial z} \right|_{r=0}, \\ B_r &= - \frac{1}{2} r \left| \frac{\partial B_z}{\partial z} \right|_{r=0}. \end{aligned} \quad (13)$$

Lorentz force for such magnetic field configuration can be written in components as

$$\begin{aligned} F_r &= qv_\theta B_z, \\ F_\theta &= q(-v_r B_z + v_z B_r), \\ F_z &= -qv_\theta B_r. \end{aligned} \quad (14)$$

First two equations describe cyclotron rotation (terms $v_\theta B_z$ and $-v_r B_z$) and drift of gyration center along the magnetic field lines (term $v_z B_r$). Last equation can be rewritten using equation (13)

$$F_z = \frac{1}{2} qv_\theta r \frac{\partial B_z}{\partial z}. \quad (15)$$

In our field configuration depending on the q sign the assumption $v_\theta = \pm v_\perp$ holds. Averaging of this expression while using $r = r_L$ from equation (6) gives the average force acting on a moving particle

$$\langle F_z \rangle = \mp \frac{1}{2} qv_\perp r_L \frac{\partial B_z}{\partial z} = \mp \frac{1}{2} q \frac{v_\perp^2}{\Omega_c} \frac{\partial B_z}{\partial z} = -\frac{1}{2} \frac{mv_\perp^2}{B} \frac{\partial B_z}{\partial z}. \quad (16)$$

We define the magnetic moment of the rotating particle as

$$\mu = \frac{mv_\perp^2}{2B}. \quad (17)$$

The average force can be generalized, using the magnetic moment μ in the form

$$F_{\parallel} = -\mu (\hat{\mathbf{B}} \cdot \nabla) B, \quad (18)$$

where $\hat{\mathbf{B}}$ is the unit vector in the direction of \mathbf{B} .

The particle traveling in different magnetic intensities B changes its Larmor radius. It may seem that this particle may also gain energy by being accelerated along the field lines through this force. We will show that it is not true and that magnetic moment μ is an invariant.

Let us start from the motion equation of the gyrating radius. We are going to take a projection along \mathbf{B} (we again assume that fields are only slowly changing)

$$m \frac{d\hat{\mathbf{B}} \cdot \mathbf{v}}{dt} = -\mu (\hat{\mathbf{B}} \cdot \nabla) B. \quad (19)$$

We now define the parallel velocity $v_{\parallel} = \hat{\mathbf{B}} \cdot \mathbf{v}$ and modify the previous equation to

$$\begin{aligned} mv_{\parallel} \frac{dv_{\parallel}}{dt} &= -\mu (v_{\parallel} \hat{\mathbf{B}} \cdot \nabla) B, \\ \frac{d}{dt} \left(\frac{1}{2} mv_{\parallel}^2 \right) &= -\mu \frac{dB}{dt}. \end{aligned} \quad (20)$$

The left hand side can be understood as a derivative of kinetic energy and the right hand side as a convective derivative along the trajectory. Since the energy is conserved we can substitute v_{\parallel} for v_{\perp} by changing the sign of the derivative

$$\frac{d}{dt} \left(\frac{1}{2} m v_{\perp}^2 \right) = \mu \frac{dB}{dt}. \quad (21)$$

Finally substitution of magnetic moment μ (equation (17)) leads to

$$\frac{d}{dt} (\mu B) = \mu \frac{dB}{dt}, \quad (22)$$

from where

$$\frac{d}{dt} \mu = 0. \quad (23)$$

2.2 MAGNETIC MIRROR TRAP

Many effects are explainable by the fact that μ is an invariant. In chapter 5 we make use of conversion between v_{\perp} and v_{\parallel} in order to collimate particles' velocities, here we are going to introduce a concept of a magnetic trap.

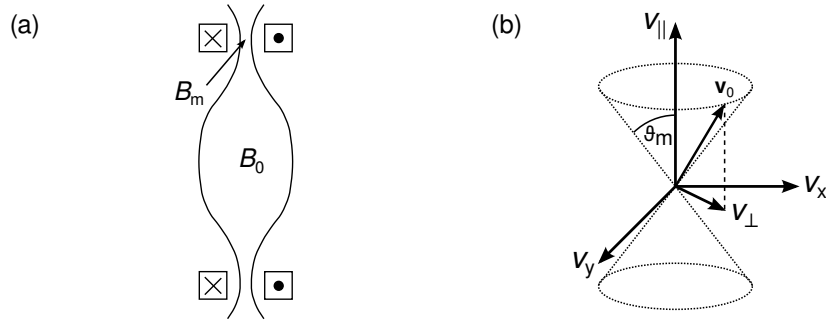


Figure 3: Panel (a) shows the rotationally symmetric magnetic field configuration for the magnetic mirror trap produced between two coils with minimal and maximal field intensity B_0 , B_m respectively. Panel (b) represents the graphical representation of the escape cone characterised by the angle ϑ_m (equation (26)) from the magnetic mirror trap (see text).

Consider the situation shown in figure 3 panel (a). Two coils are creating a magnetic field with maximum and minimum. If the particle during its movement is traveling from lower magnetic field intensity B_0 to the region with higher intensity B_m , its magnetic moment μ stays

constant, and v_{\perp} has to increase at the expense of v_{\parallel} . In the extremal point the v_{\parallel} component may become zero and the particle is reflected back to the lower magnetic field.

Let us find the conditions particle has to fulfill in order to stay confined. Particle in the B_0 region has a total velocity \mathbf{v}_0 with components $v_{\perp 0}$ and $v_{\parallel 0}$ (with respect to \mathbf{B}). In the reflection point, region with $B = B_m$, the particle's total velocity \mathbf{v}_0 stays the same due to the energy conservation and its components become $v_{\perp m}$ and $v_{\parallel m} \equiv 0$

$$\frac{1}{2} \frac{mv_{\perp 0}^2}{B_0} = \frac{1}{2} \frac{mv_{\perp m}^2}{B_m}, \quad (24)$$

$$\mathbf{v}_0^2 \equiv v_{\perp 0}^2 + v_{\parallel 0}^2 = v_{\perp m}^2. \quad (25)$$

Combining equations (24) and (25) we have

$$\frac{B_0}{B_m} = \frac{v_{\perp 0}^2}{v_{\perp m}^2} = \frac{v_{\perp 0}^2}{\mathbf{v}_0^2} = \sin^2(\vartheta_m). \quad (26)$$

Figure 3 panel (b) summarises this result graphically by introducing the escape cone characterised by ϑ in velocity space. All particles with velocity components ratio lower or equal than $\sin(\vartheta_m)$ are confined in the trap. Other particles are free to enter or exit the trap.

One interesting feature of the escape cone is that it is only defined by the ratio of B_0/B_m and it is not dependent on particle's mass or charge. The existence of the escape cone has also a consequence that velocity distribution of particles confined in the magnetic mirror trap is never isotropic.

2.3 CHARGED PARTICLES IN ELECTROSTATIC FIELDS

Let us start our discussion of electrostatic fields by introducing the Gauss's law

$$\nabla \cdot \mathbf{E} = \frac{\rho}{\epsilon_0}, \quad (27)$$

where \mathbf{E} is the electric field, ρ is the charge density, and ϵ_0 is the vacuum permittivity. The Gauss's law describes the relation between charge and the electric field in space. The electric potential φ is connected with electric field as

$$\mathbf{E} = -\nabla\varphi. \quad (28)$$

2.3.1 Laplace equation

Combining the Gauss's law with the electric potential and simple vector identity

$$\nabla \cdot \nabla \varphi = \Delta \varphi = -\frac{\rho}{\epsilon_0}, \quad (29)$$

one obtains the Poisson equation, which reduces to the Laplace equation in regions with no charged particles

$$\Delta \varphi = 0. \quad (30)$$

The Laplace equation has important consequences that can be summarised in two theorems:

Theorem 1 *If φ satisfies Laplace equation, the average value of φ over a surface of any sphere equals to the value of φ at the center of the sphere.*

Theorem 2 *If φ satisfies Laplace equation in a given volume, it has no extremal point inside the volume.*

These theorems can be proved using the divergence theorem¹ from vector calculus. The second theorem implies that it is not possible to construct the electrostatic configuration where the charged particle would remain stable.

In figure 4 we illustrate the use of the Laplace's equation. The Dirichlet problem for Laplace's equation consists of finding a potential φ on some domain while the value of φ is given on the boundary. In figure 4 the solution is shown for the cut perpendicular to the axis of an octopole. One can see that a saddle point appears in the center of the octopole where $\nabla \varphi = 0$. This is not in contradiction with theorem 2. Although there are no forces acting on a particle in the saddle point, any slight move will lead to forces accelerating the particle in the direction away from the saddle point. In section 2.4 we show that by introduction time dependent electric potentials configurations with true minima are becoming possible.

2.4 CHARGED PARTICLES IN RADIO FREQUENCY FIELDS

2.4.1 Adiabatic approximation

To describe the motion of one particle with mass m and charge q in an inhomogeneous electric field $E(\mathbf{r}, t)$, we first have to assume that:

¹ If \mathbf{F} is a continuously differentiable vector field defined on neighborhood of V , then $\int_V (\nabla \cdot \mathbf{F}) dV = \oint_{\partial V} (\mathbf{F} \cdot \hat{\mathbf{n}}) dS$.

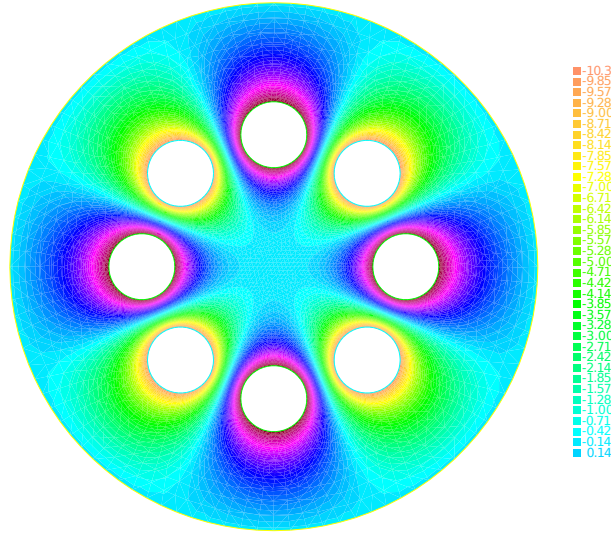


Figure 4: Solution of the Laplace equation (2D) with Dirichlet boundary condition using finite element method for a cut through an octopole in a grounded conducting tube. Potentials applied on two rod systems are ± 10 V.

- Quasistationary electric field $E(\mathbf{r}, t)$ is composed of a static field $E_s(\mathbf{r})$ and time dependent part $E_0(\mathbf{r}) \cos(\Omega t + \delta)$ where $E_0(\mathbf{r})$ is the field amplitude, $\Omega = 2\pi f$ is the constant angular frequency and δ is a phase.
- The motion is described by the differential equation

$$m \frac{d\mathbf{r}}{dt} = qE_0(\mathbf{r}) \cos(\Omega t + \delta) + qE_s(\mathbf{r}). \quad (31)$$

- The frequency is high enough for amplitude $a \cos(\Omega t)$

$$a = \frac{qE_0}{m\Omega^2} \quad (32)$$

to be reasonably low².

These assumptions reduce our task to describe the particle movement in the so-called adiabatic approximation.

2.4.2 Effective potential V^*

We will seek the solution of the equation (31) in the form of smooth drift term $R_0(t)$ and a rapidly oscillating motion $R_1(t) = a(t) \cos(\Omega t)$

$$\mathbf{r}(t) = R_0(t) + R_1(t) = R_0(t) + a(t) \cos(\Omega t). \quad (33)$$

² For quantification of "low" see end of the section 2.4.2.

We presume that slow spatial variation in E_0 allows us to keep only first two terms in cosine expansion

$$E_0(R_0 + a \cos(\Omega t)) = E_0 R_0 - (a \cdot \nabla) E_0(R_0) \cos(\Omega t) + \dots, \quad (34)$$

and that slow time variations imply $\frac{da}{dt} \ll \Omega a$ and $\frac{d^2 R_0}{dt^2} \ll \Omega \frac{dR_0}{dt}$. Combining equations (31)–(34) and assuming that amplitude a changes only by motion along R_0 , we have

$$m \frac{d^2 R_0}{dt^2} = -q (a(t) \cdot \nabla) E_0(R_0) \cos^2(\Omega t). \quad (35)$$

Using a time average of $\cos^2(\Omega t) = \frac{1}{2}$, vector identity³ and Faraday's law $\nabla \times E = 0$ we can write

$$m \frac{d^2 R_0}{dt^2} = -\frac{q^2}{4m\Omega^2} \nabla E_0^2, \quad (36)$$

which describes the time averaged motion of particle in the oscillatory field.

We still have to account for the static part of the electric field E_s , which according to equation (28) can be characterised by electrostatic potential φ_s . Let us define the effective potential V^* as

$$V^* = \frac{q^2 E_0^2}{4m\Omega^2} + q\varphi_s. \quad (37)$$

With such defined effective potential, the equation of motion (31) can easily be written as

$$m \frac{d^2 R_0}{dt^2} = -\nabla V^*(R_0). \quad (38)$$

This equation describes the motion of a particle in simple time independent potential. Moreover, it allows us to easily characterise the motion in complicated field geometries only by investigating the properties of the effective potential V^* .

Our definition of the effective potential would not be complete without specifying the conditions of validity. Therefore, we introduce the adiabaticity parameter η as

$$\eta = \frac{|2(a \cdot \nabla) E_0|}{|E_0|}, \quad (39)$$

which can be rewritten using equation (32)

$$\eta = \frac{2q |\nabla E_0|}{m\Omega^2}. \quad (40)$$

³ $(E \cdot \nabla)E = \frac{1}{2} \nabla E^2 - E \times (\nabla \times E) = \frac{1}{2} \nabla E^2$

The definition of the adiabaticity parameter is established as the condition that requires the change of the field E_0 over a full distance of oscillation to be smaller than the field itself

$$|2(\alpha \cdot \nabla) E_0| < |E_0|. \quad (41)$$

Because of the last inequality we demand $\eta \ll 1$ for justifying the use of the adiabatic approximation. The value of $\eta < 0.3$ is widely accepted as sufficient for most applications and is supported by numerical simulations and experimental observations (e. g. quadrupole fields Dehmelt and Walls (1968), rf traps Gerlich (1992)).

2.4.3 Linear Multipoles

Linear multipoles are systems composed of $2n$ long parallel cylindrical rods evenly spaced on a diameter with inscribed radius r_0 . The z axis is coincident with the multipole axis of symmetry. To describe the potential inside the multipole we use V_0 as amplitude and Ω to denominate angular frequency of the oscillatory voltage, and U_0 for the static voltage difference applied to the rods

$$\varphi_0 = U_0 - V_0 \cos \Omega t. \quad (42)$$

We also define the reduced radius

$$\hat{r} = \frac{r}{r_0}, \quad (43)$$

and the characteristic energy

$$\varepsilon = \frac{1}{2n^2} m \Omega^2 r_0^2. \quad (44)$$

Detailed description of deriving the effective potential V^* for this configuration is out of the scope of this work and can be found in Gerlich (1992).

We define the effective potential

$$V^* = \frac{1}{8} \frac{q^2 V_0^2}{\varepsilon} \hat{r}^{2n-2} + q U_0 \hat{r}^n \cos n\theta, \quad (45)$$

where θ is the cylindrical coordinate and the adiabaticity parameter η for the linear multipole

$$\eta = \frac{n-1}{n} \frac{q V_0}{\varepsilon} \hat{r}^{n-2}. \quad (46)$$

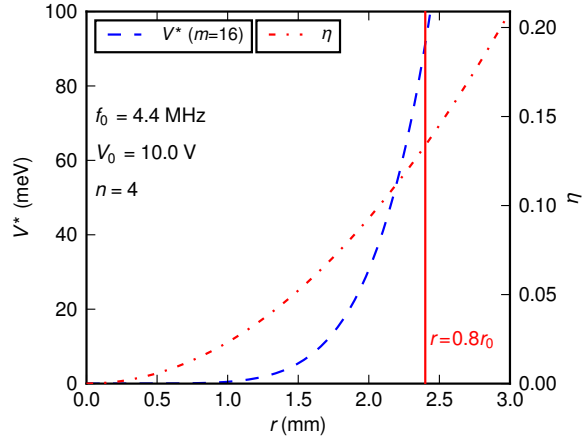


Figure 5: Effective potential V^* and adiabaticity parameter η in an octopole for singly charged mass 16 u ion. Vertical line represents the turning radius $0.8 \cdot r_0$.

In figure 5 we show V^* and η for an octopole ($2n = 8$; $\Omega = 4.4$ MHz; $V_0 = 10$ V; $U_0 = 0$ V) and singly charged oxygen anion⁴. It is established to require the turning radius for the particles moving in the effective potential to be $0.8 \cdot r_0$. As discussed in section 2.4.2 operating conditions which fulfill $\eta < 0.3$ can be safely described using the effective potential. Operating the multipole beyond the validity of the adiabatic approximation, or using the turning radius higher than $0.8 \cdot r_0$ may have several effects, which may not be apparent immediately. The best known is the effect of rf heating, where particles are still confined in the effective potential, but the energy of particles is not conserved. Instead, particles are gaining energy from the rf field, when they are present too close to the poles.

Let us finish our discussion with the best known $2n$ pole, which is the quadrupole with $n = 2$. Applying the adiabatic theory to this device, it can be described by introducing the Mathieu's parameters

$$q_2 = 4 \frac{qV_0}{m\Omega^2 r_0^2} \quad \text{and} \quad a_2 = 8 \frac{qU_0}{m\Omega^2 r_0^2}. \quad (47)$$

Mathieu equations can be generalized for higher order multipoles, although the quadrupole is the only $2n$ pole which has the q parameter not dependent on \hat{r} and that underlying differential equations are cou-

⁴ See listing 2 in Appendix C for script source.

pled and nonlinear for higher order multipoles. The Mathieu(a_2, q_2) stability diagram⁵ for the quadrupole is shown in figure 6.

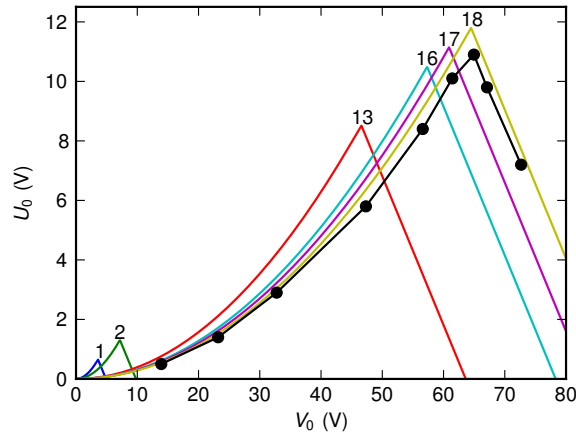


Figure 6: Mathieu stability diagram for a quadrupole (only the important lower zone). Stability regions for several masses between 1 to 18 are shown (full lines). Black points represents measured points where the transmission of the quadrupole for mass 16 dropped to 0. The amplitude V_0 was measured with uncalibrated probe, hence the error in V_0 is greater than 10%. Quadrupole parameters: $f = 1.72$ MHz, hyperbolic rods, $r_0 = 4$ mm.

Because of its unique properties amongst multipoles the quadrupole is often used as *Quadrupole Mass Spectrometer (QMS)*. It is usually operated in the tip of the diagram (figure 6), where high mass resolution can be achieved. However, high resolution is obtained at the expense of disturbing the kinetic energy distribution of the ions, because the adiabatic theory is only valid in the left part of the diagram, where V_0 is small.

Less known method of use is the low mass band pass and high mass band pass filter. The high mass filter uses high V_0 (right part of the Mathieu diagram) to discriminate low masses. Adiabatic theory is also not valid.

On the other hand, the low mass band pass filter operates in the range of the validity of the adiabatic approximation theory. It ensures the conservation of energy through the quadrupole and is thus well suited for guiding low energy ions for trapping.

⁵ See listing 1 in Appendix C for script source.

Equation for a threshold condition for a mass to be transmitted can be written as

$$m < \frac{qV_0^2}{\Omega^2 r_0^2 U_0}. \quad (48)$$

All lighter masses, up to the mass m , are transmitted.

EXPERIMENTAL TECHNIQUES

This chapter, focused on the components of our experimental setups, is going to give a short introduction into the field of experimental physics of ion-molecule reactions with emphasis on the radio frequency ion traps.

Charged particles production, detection and confinement is going to be discussed, together with determination and confirmation of conditions in the confinement area. A unique atomic beam source of H atoms is also going to be described with emphasis on determination of beam properties.

The reader is strongly encouraged to consult the publication by Gerlich (1992) if interested in rf trapping and technology in general.

3.1 CHARGED PARTICLE PRODUCTION

The cations and anions (charged particles) are created using the same device in our experiments. The *Storage Ion Source (SIS)* is an ion source described by Gerlich (1992), though it has been used almost exclusively for cation production until now.

The ions and anions are created at the same time from the suitable precursor gas (table 1) by electron bombardment (figure 7). Rhenium wire is used as a hot filament for thermionic electron production. Electrons are then focused into the cavity surrounded by rf plates (thick lines, left in figure 7), where the collisions with the precursor gas molecules take place.

Table 1: Precursor gases used in SIS, their approximate ionization cross sections, and corresponding electron energy. Compiled from Massey (1976) and Tawara et al. (1989).

GAS	ION	CROSS SECTION (cm ²)	ELECTRON ENERGY (eV)
H ₂	H ⁺	6 · 10 ⁻¹⁸	100
H ₂	H ⁻	4 · 10 ⁻²⁰	14.5
N ₂ O	O ⁻	1 · 10 ⁻¹⁷	2

In case of positive ion production, the electron energy has to be greater than 1st ionization potential, the main process of cation production is electron impact ionization. On the other hand, the dissociative attachment or polar ionization are the dominant processes of anion production (Massey, 1976). The produced cation/anion is trapped in the rf effective potential (section 2.4.1).

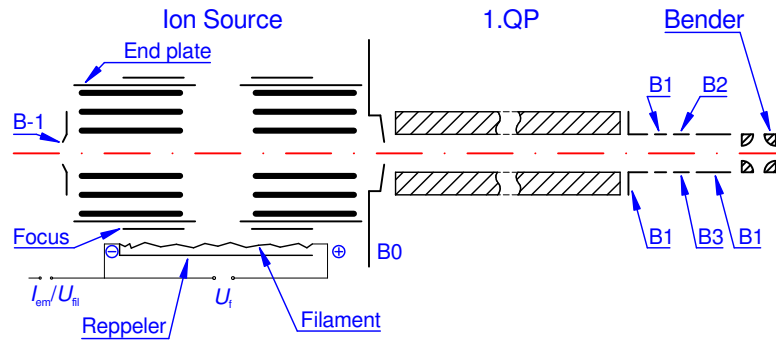


Figure 7: Storage ion source with quadrupole mass spectrometer (not to scale). Charged particles are created in the ion source (left), extracted and selected in QMS (center) and focused using the ion electrostatic optics (right). The bender at the end is used to bend the ion beam by 90° into the 22-pole trap setup (section 4.1, figure 19).

Using suitable electrostatic potentials, only cations or anions are extracted from SIS to the QMS. Since SIS works for wide ion mass range, the QMS is needed in order to select only the mass of interest. Figure 8 illustrates the transmission properties of the QMS. The f_0 and V_0 are constant and the U_0 is varied. In this particular case, H_2 is used as a precursor gas in the SIS and electric fields are set for cation extraction. The intensity on the ordinate represents the total number of ions (mass 1, 2, and 3 u corresponding to H^+ , H_2^+ and H_3^+ respectively) detected after passing through the QMS. The inner panel represents Mathieu equations (47) for this configuration as described in section 2.4.3. The calculated thresholds for selection for each mass (intersection of the dash-dotted line with respective full line in inner panel) are marked using triangles.

The last part of the charged particles production instrument is the electrostatic optics used to focus the cations/anions before injection into the next stage. If needed, the electrostatic “bending” quadrupole (most right part in figure 7) can be used to steer the ions by 90°. This feature is used in the 22-pole trap setup (figure 19).

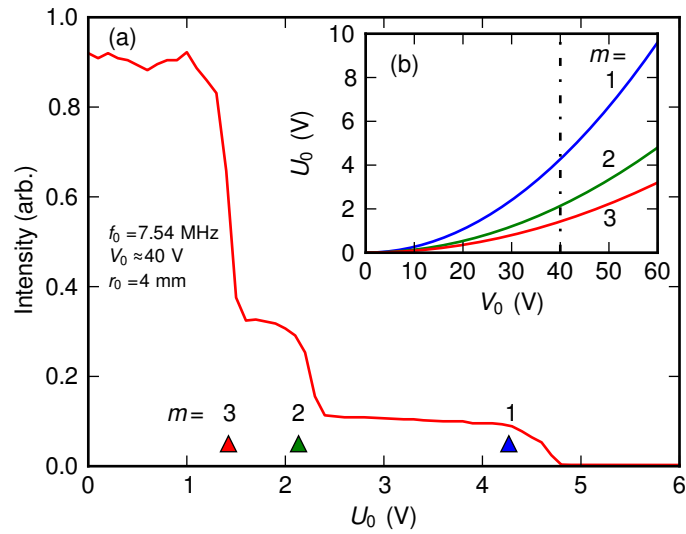


Figure 8: Transmission properties of the QMS used for mass selection of ions produced in SIS. Panel (a) – total number of ions passing through the QMS as a function of U_0 (see text). Triangles represents calculated position of first stable trajectory in the QMS according to equation (48). Panel (b) – graphical representation of Mathieu equations (47). Dash-dotted line shows the operation amplitude V_0 .

3.2 PARTICLE DETECTORS

The particle detection systems used in the 22-pole trap and *Electron Spectrometer with Multipole Trap (ES-MPT)* apparatuses will be described in this section. It is important to mention that only charged particles (cations, anions, electrons) are detectable in our setups and that every single detection event is converted to digital pulse and accounted for. The detection based on current measurement is not used.

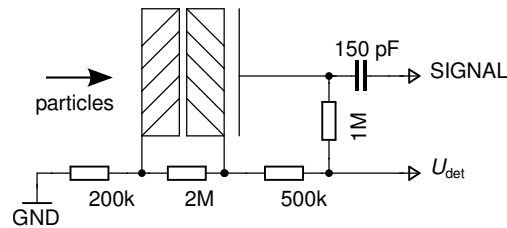


Figure 9: Schematic diagram of MCP electrical connection in configuration for detecting negative particles ($U_{det} \approx +2750$ V).

Three detection systems have been used, though only the *Micro Channel Plate* (MCP) is going to be described as the only detector suitable:

1. *Daly type detector* (described in Daly (1960)) used in experiments where H atom source has been characterised. The main disadvantage of this type of detector is its inability to detect negative anions.
2. *Channeltron* (Sjuts KBL20RS) was the first device we used for anion detection. The channel in this type of channeltron has multiple turns. We discovered that its amplification quickly decreases in magnetic field and is not suitable for our setup.
3. MCP (Hamamatsu F-4655-12) is used for cations, anions, and electrons. Works reasonably well with magnetic field intensities used in ES-MPT.

The schematic diagram of electrical connection of the MCP in configuration for negative particle detection is shown in figure 9. The 150 pF capacitor and 1 M Ω resistor are located inside the vacuum chamber close to the collector plate. The remaining resistors creating the voltage divider are located outside the vacuum and can be easily reconfigured for positive ion detection.

The output signal coupled through the 150 pF capacitor is directly connected to the discriminator (Phillips Scientific model 6904) from where it is fed to the counters and *Multi Channel Scaler* (MCS). The pulse height distribution of pulses on the output of the MCP (50 Ω termination) in zero magnetic field and H⁻ as primary particles being detected is shown in figure 10. The discriminator level is set to \approx 40 mV (according to figure 10).

The MCP has a different detection efficiency for ions, anions, and electrons. Furthermore, particles of the same type (e. g. ions) with different mass or energy have different detection efficiency (Gilmore and Seah, 2000). Direct comparison of absolute number of different particles detected is not an easy task. In all experiments presented in this work, only relative numbers of the same particles are measured – we do not need to worry about absolute detection efficiencies.

The magnetic field influences the MCP too. This phenomena is known and has been studied by Morenzoni et al. (1988), and Lehmann et al. (2009). The change in number of events detected, depending on different magnetic field configurations, is shown in figure 11. It is not known, whether these phenomena are caused by the MCP itself, or by

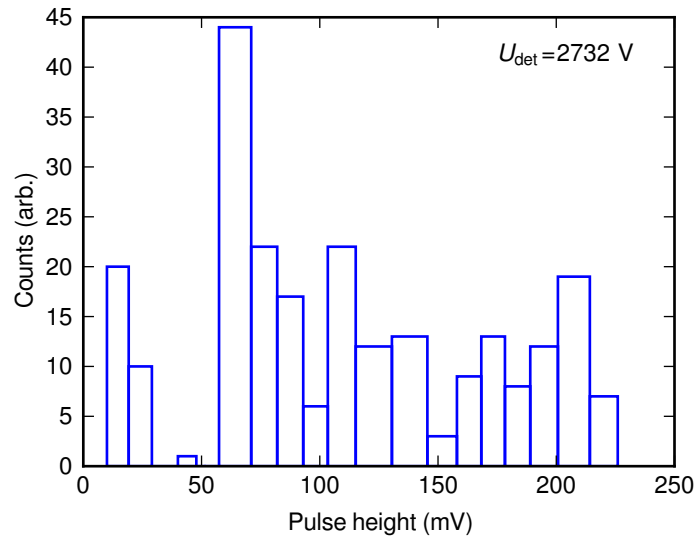


Figure 10: Pulse height distribution of pulses produced by H^- primary anion ($B = 0$).

magnetic field guiding and/or focusing of H^- anions. The fact, that all measurements where the MCP is operated in the magnetic field do use the same magnetic intensity in the detector area, has two consequences:

- the MCP has the same overall detection efficiency
- all individual measurements can be directly confronted between each other.

The experiment operator although must be aware of these caveats. These findings are also valid for electron detection in the electron spectrometer (chapter 5).

3.3 H ATOM SOURCE

3.3.1 Theory of operation

Schematic diagram of atomic H source used in this work is shown in figure 12. It is an atomic source based on dissociation of molecular hydrogen in an rf discharge (Slevin and Stirling, 1981). Special emphasis is given to accurate determination of thermal energy distribution of produced atoms and the beam effective number density of H and H_2 .

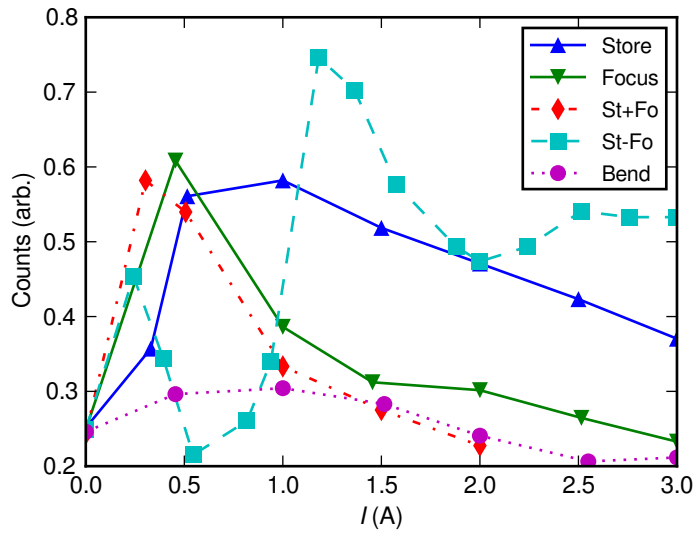


Figure 11: Influence of magnetic field on MCP relative overall detection efficiency (H^- anion). The current on the abscissa represents the current in the respective coil (figure 31 in chapter 5). Each symbol represents different coil configuration. Store – coils in the trapping area, Focus – refocusing coil, Bend – coil for bending the field of axis. St+Fo and St-Fo represent parallel and anti-parallel combination of Store and Focus coils.

Molecular hydrogen is leaked into the glass discharge tube (left side, figure 12). The tube is water cooled and immersed into the cavity, where rf radiation is fed. Mixture of discharge products is flowing through the glass tube into the copper block with thin “L” shaped channel. The Cu block is called accommodator and is connected to the cold head, its temperature can be varied between $T_{ACC} = 7$ and 300 K. The hydrogen pressure in discharge tube is in order of few 100 Pa, pressure in the vacuum chamber is in order of 10^{-3} Pa. The beam coming from the accommodator is skimmed and runs through several differentially pumped stages.

The main issue of the H atom source is to achieve high dissociation ratio and to keep the recombination as low as possible in the glass tube and on the accommodator walls. Our final solution involves thin *Polytetrafluoroethylene – Teflon (PTFE)* coating of the Cu wall.

The use of hexapole magnets to focus the diverging H atom beam was also considered and tested. The added magnets did not increase the beam density significantly. Moreover, the magnetic field disturbs the H atom velocity distribution (Borodi et al., 2009). Thus the H atom

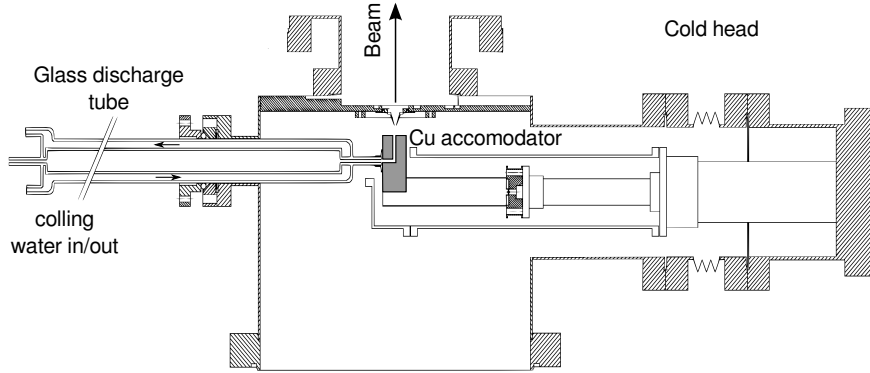


Figure 12: H atom source (schematic diagram). Glass discharge tube (left) is connected to the accommodator (center), cooled by a cold-head (right).

beam source was operated without additional focusing in presented experiments.

3.3.2 Atomic beam velocity distribution

The atomic beam velocity distribution has been measured using the *Time of Flight* (TOF) method. Wheel with slits was used to chop the beam. After passing the TOF free path, the beam was ran through the ionizer to convert the H atoms to H^+ ions, which could be consequently detected.

The TOF spectra of H atoms for two different accommodator temperatures are shown in figure 13. Recorded spectra are evaluated using the analytical function for the intensity

$$N(t) = N_0 + C \frac{L^3}{(t - t_0)^4} e^{-\frac{L^2 m}{2k_B T (t - t_0)^2}}, \quad (49)$$

where N_0 is the background intensity (intensity not influenced by the slits), L is the free flight length, k_B is the Boltzmann constant and m is the mass of H atom (N , C , t_0 and T are the free parameters of the fit). The beam source is effusive, thus we assume that the beam is Maxwellian in the equation (49). The temperature characterisation of the beam is in good agreement with the accommodator temperature T_{ACC} and differs by no more than 20 %.

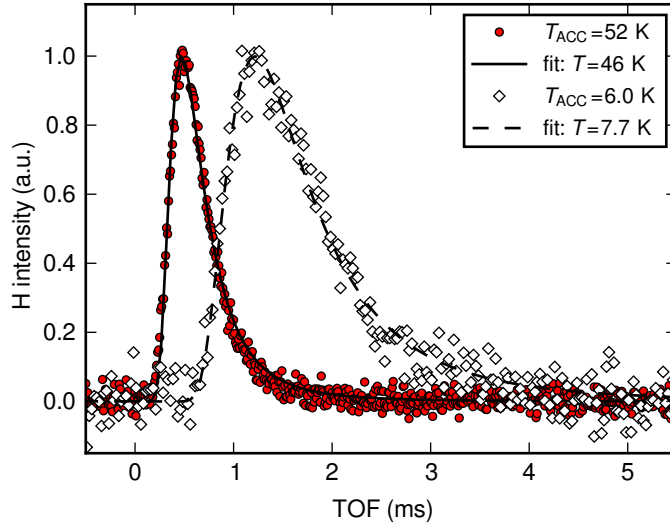


Figure 13: Time of flight (TOF) spectra of atomic H in the beam. Two accommodator temperatures are presented. Fits represent the Maxwell-Boltzman distribution convolved with the window function. Resulting temperature is in good agreement with the accommodator temperature.

3.3.3 Determining the beam density in the trap

First, let us repeat that the beam from the atomic H beam source is not composed of pure H atoms. The dissociation ratio α , defined as

$$\alpha = \frac{H_2^{\text{off}} - H_2^{\text{on}}}{H_2^{\text{off}}}, \quad (50)$$

where H_2^{off} and H_2^{on} represent H_2 density in the beam while the discharge is on and off respectively, is shown in figure 14. The operating conditions of the source are easily characterised using α . Figure 14 shows 30% dissociation in this case and huge decrease of α around $T_{\text{ACC}} = 25$ K. As a consequence the H atom source can be operated only in a suitable T_{ACC} range.

The best way of the in situ beam characterisation is the use of a chemical reaction for calibration. There are many suitable reactions to characterise atomic beam sources (for positive ions see Scott et al. (1997); Fehsenfeld and Ferguson (1971); Tosi et al. (1984), for reactions with negative anions Martinez et al. (2009)). The rate coefficients for the calibration reactions are usually known with high accuracy, although only for temperatures higher or equal to 300 K. We chose the reaction of CO_2^+ with atomic and molecular hydrogen to calibrate both

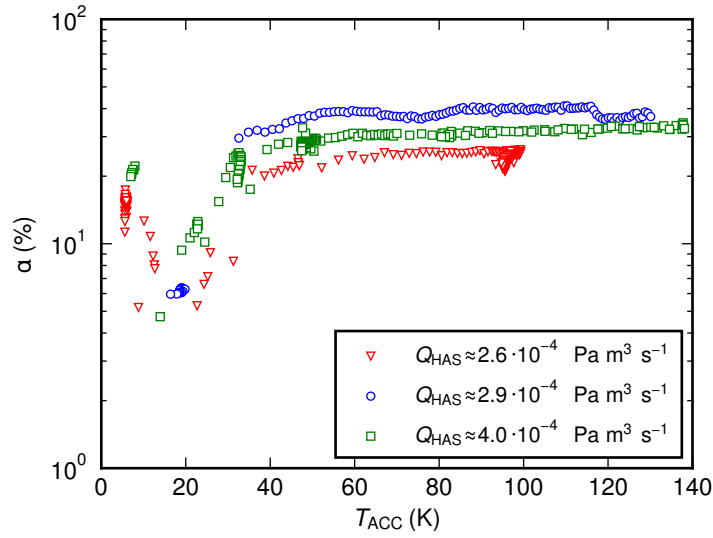
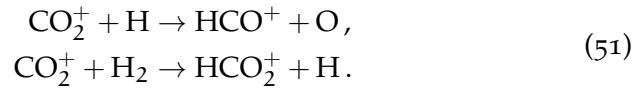


Figure 14: Dissociation ratio α of H to H_2 in the beam from the H atom source as a function of accommodator temperature. Discharge is operated with 60 W power at 27.12 MHz. The accommodator is equipped with PTFE tube in this case. Results with three different H_2 flows (Q_{HAS}) through the discharge tube are presented.

densities at once. This reaction was investigated by Borodi et al. (2009) even for temperatures in the range 25 to 300 K (the only disadvantage is the overall rate coefficient uncertainty of 40 %).

The chemical model of the calibration reaction is composed of two equations



Since the rate constants are known, only number densities are varied in the model and the best fit gives the values of number density $[\text{H}]$ and $[\text{H}_2]$ present in the trap.

Figure 15 shows one time evolution of number of ions present in reactions (51) in the trap. The CO_2^+ ions are created in the SIS from CO_2 gas using electron bombardment. The CO^+ ion is also created, the quadrupole is used to filter only mass 44 u before injection into the trap. The ratio of CO_2^+ number to other ions is better than 10^3 . The beam is aligned to the trap and the discharge is turned on and off to evaluate the presence of H atoms. The number densities (typical values) obtained from the reaction model (51) are $[\text{H}] \cong 1.0 \cdot 10^8 \text{ cm}^{-3}$ and $[\text{H}_2] \cong 5.5 \cdot 10^9 \text{ cm}^{-3}$.

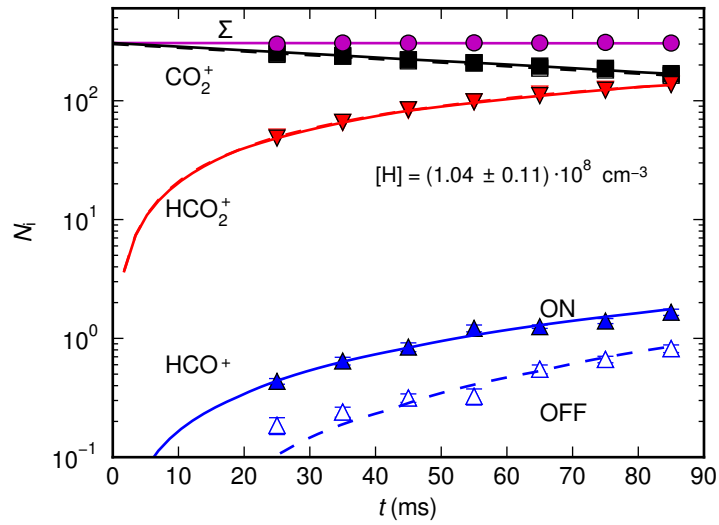


Figure 15: Number of CO_2^+ , HCO^+ , HCO_2^+ and the sum Σ of all particles detected in the trap as a function of storage time. The symbols represent measured data, solid and dashed lines represent results of a fitted chemical model. Measurements with the discharge turned on and off are shown using full and dashed lines respectively. The difference between HCO^+ lines is due to the presence of atomic H. The molecular H_2 is always present due to recombination on the walls and diffusion from the source.

Note that the measured number density shown in figure 15 does not take the uncertainty of the rate coefficients into account. Several other aspects need to be considered before using obtained number densities in other reactions, see section 4.2.2.

3.4 REACTION TEMPERATURE

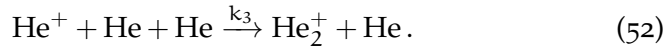
In our experiments, we are often studying the temperature dependences. The 22-pole trap is mounted on a cold head equipped with a heater and a silicon diode used as a thermometer. After adjusting the heating current, the temperature stabilises and the trap's wall temperature is known with high accuracy (better than 1 K). However, are the trap temperature and the temperature of gas and cations/anions in the trap the same? Moreover, what happens if anions in the trap are interacting with a beam of particles with different temperature injected into the trap? We will answer these questions in following sections.

3.4.1 *Thermometer for low temperature ions*

The neutral gas molecules in the 22-pole trap are in contact with walls with known temperature. Since the pressure in the trap is low enough to be in molecular regime, the gas molecules interact with walls more often than with each other and we can estimate that the neutral gas is in thermal equilibrium and has the same temperature as walls do.

The same cannot be stated for the ions, which are trapped in the rf field and do not interact with cold walls. The temperature equilibrium has to be achieved by collisions with cold neutral gas. Moreover, the ions can be subject to rf heating as discussed in section 2.4.3.

We decided to investigate the temperature in the trap using a ternary association of He^+ and He



This reaction can be used as a thermometer. Helium assisted association has been studied in various experimental setups e.g. liquid nitrogen cooled flowing afterglow (Johnsen et al., 1980), liquid helium cooled drift tube (Bohringer et al., 1983) and helium closed cycle cryostat cooled rf traps (Smith and Gerlich, 2008). Temperature dependence of k_3 in form $k_3 \sim T^{-\kappa}$ has been found.

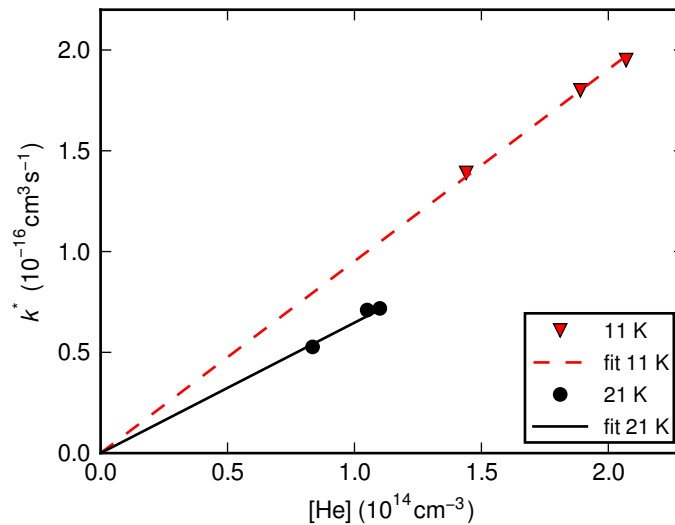


Figure 16: Apparent binary rate coefficient k^* dependence on number density of He buffer gas shown for two different temperatures. Lines represent linear fit through the axes origin.

In the 22-pole trap, we are only able to measure apparent reaction rate constant k^* , which is connected with ternary k_3 and binary (or radiative) k_2 rate coefficients as

$$k^* = k_3 [\text{He}] + k_2, \quad (53)$$

where $[\text{He}]$ is the He gas concentration. The easiest way of accurate k_3 determination is to vary the He density in the range where $k_2 \leq k_3 [\text{He}]$. In figure 16 we show the dependence of apparent rate coefficient k^* on the He density in the trap. The linear dependence of k^* on the density shows that we are not measuring in helium density range where the binary association is a significant contributor (we can neglect the k_2 term in equation (53)).

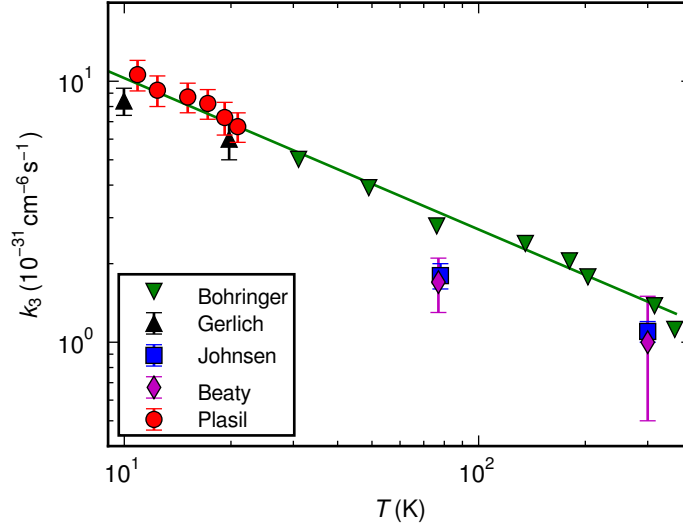


Figure 17: Ternary association rate coefficient k_3 as a function of temperature. Circles correspond to the rf 22-pole trap measurements (calculated from data plotted on figure 16). Triangles (down) – drift tube measurements (Bohringer et al., 1983). Squares – flowing afterglow measurements (Johnsen et al., 1980). Triangles (up) – older rf trap measurements (Smith and Gerlich, 2008). Diamonds – older drift tube measurements (Beaty and Patterson, 1965). Measured k_3 increases with constant exponent $\kappa = -0.56 \pm 0.1$ down to 10 K (full line ($k_3 \sim T^{-\kappa}$), Bohringer et al. (1983)).

In figure 17 we summarise our temperature dependence of k_3 measurement together with older results. The temperature on the abscissa is the temperature measured by a silicon diode connected to the trap copper wall. These results show that we are able to attain reaction tem-

peratures down to 10 K at least for ions of mass 4 u and higher. These results were published in Plašil et al. (2012).

3.4.2 Collision temperature for particles with different T

In the experiment with atomic H beam we study the interaction of particles with different mass and temperature m_1, T_1 and m_2, T_2 respectively. We will show that such situation is easily transferable to equivalent situation with particles at single temperature. For exact derivation see Roučka (2012).

Let us define the normal distribution $\mathcal{N}(x, \sigma^2)$ centered at zero with variance σ^2 . The Maxwell velocity distribution of particles with mass m_1 and temperature T_1 is $f(\mathbf{v}) = \mathcal{N}(\mathbf{v}, k_B T_1 / m_1)$. The relative velocity distribution f_{rel} is a convolution of the velocity distributions

$$f_{\text{rel}}(\mathbf{v}_{\text{rel}}) = \mathcal{N}\left(\mathbf{v}_{\text{rel}}, \frac{k_B T_1}{m_1}\right) * \mathcal{N}\left(\mathbf{v}_{\text{rel}}, \frac{k_B T_2}{m_2}\right) \quad (54)$$

Convolution of two normal distributions is a normal distribution with the sum of variances

$$f_{\text{rel}}(\mathbf{v}_{\text{rel}}) = \mathcal{N}\left(\mathbf{v}_{\text{rel}}, \frac{k_B T_1}{m_1} + \frac{k_B T_2}{m_2}\right). \quad (55)$$

If the system is in thermal equilibrium, i. e., $T_1 = T_2 = T$, the resulting variance is $\sigma^2 = k_B T (m_1 + m_2) / m_1 m_2$. We can write the equation (55) in the form

$$f_{\text{rel}}(\mathbf{v}_{\text{rel}}) = \mathcal{N}\left(\mathbf{v}_{\text{rel}}, k_B T_{\text{col}} \left(\frac{m_1 + m_2}{m_1 m_2}\right)\right), \quad (56)$$

where T_{col} defines the interaction (collision) temperature

$$T_{\text{col}} = \frac{T_1 m_2 + T_2 m_1}{m_1 + m_2}. \quad (57)$$

The effusive beam has a Maxwell distribution. Though only a conical subset of this distribution is available in the reaction region where it interacts with confined particles, the conclusion regarding the interaction temperature T_{col} also applies, due to the spherical symmetry (Roučka, 2012).

As discussed in section 3.3, and shown in figure 13, our H beam has a Maxwellian distribution with temperature T_{beam} . Therefore, when interacting with particles in the trap with temperature T_{trap} , the interaction temperature of the reaction can be written as

$$T_{\text{kin}} = \frac{T_{\text{beam}} m_{\text{trap}} + T_{\text{trap}} m_{\text{beam}}}{m_{\text{beam}} + m_{\text{trap}}}. \quad (58)$$

THE REACTION RATE COEFFICIENTS

Several positive ions have been observed and identified in the *Interstellar Medium (ISM)*, where they play an important role in space from evolution of interstellar clouds to the formation of stars. The same could not have been said for the negative ions before the article by McCarthy et al. (2006). Since then several other negative ions have been identified, with the lightest being CN^- (Agúndez et al., 2010). The simplest negative ion H^- has not been identified directly.

In this chapter, we are going to present a laboratory study of negative ions, focusing on the reaction rate coefficients. The rate coefficient characterises the reaction by establishing the rate at which it proceeds. In astrophysics, the coefficients are important for accurate models explaining the abundances in the constitution of interstellar matter (Glover et al., 2006).

4.1 THE 22-POLE TRAP APPARATUS

The reaction rate coefficients presented in this work are investigated using the rf ion *22-pole trap (22-pt)* (Gerlich, 1992; Gerlich and Horning, 1992; Gerlich, 1995) in combination with an effusive atomic hydrogen beam source (section 3.3). This apparatus was built in Chemnitz University of Technology as described in (Borodi et al., 2009; Plašil et al., 2011; Gerlich et al., 2011). The configuration used in our experiments is presented schematically in figure 18 (for full CAD drawing see figure 44 in Appendix A).

Ions are produced in a *SIS* (section 3.1) by electron bombardment of precursor gas. After thermalization in the *SIS* the ions with energies in order of 100 meV are mass selected using a quadrupole mass filter and injected into the 22-pole trap. The ion trap temperature $T_{22\text{pt}}$ is variable in the range $10 \text{ K} < T_{22\text{pt}} < 300 \text{ K}$. Ions are cooled down by collisions with buffer gas (He), close to the trap temperature. The agreement between the trap temperature and the ion temperature was studied by action spectroscopy for heavier ions (Glosík et al., 2006) and by numerical simulations for mass 1 u ions (Asvany and Schlemmer, 2009). The ternary association of $\text{He}^+ + \text{He}$ has also been used to confirm the ion (mass 4 u) temperature (section 3.4.1). The upper limit

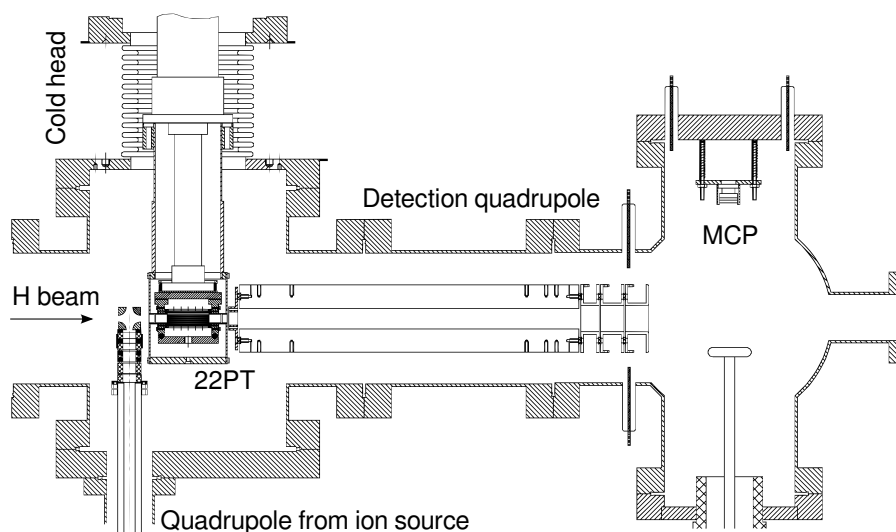


Figure 18: Cut through the 22-pole rf ion trap apparatus. Ions produced in SIS (left, bottom) are injected to the trap (center) using the bending quadrupole. Products are selected using the second quadrupole (center, right) before detection using an MCP (right, top).

for ion temperature is estimated to be 5 K above the measured trap wall temperature.

Ions are confined in the trap using inhomogenous rf field (see section 2.1) for confinement in the radial direction and electrostatic barriers in the axial direction. Neutral gas can be introduced to the trap volume, or an effusive particle beam can be aligned to pass through the trap. In the latter configuration, the *H Atom Source* (HAS) (section 3.3) is connected from the left side of the apparatus (figure 18) to form the *Atomic beam – 22-pole trap* (AB 22-pt) apparatus.

A standard experimental procedure for examining an ion-neutral reaction in the trap is used (Gerlich and Horning, 1992; Gerlich, 1995). Each single measurement starts with a pulsed extraction of the primary ions from the SIS. Ions of the desired mass are then selected using a quadrupole mass filter and injected into the 22-pole trap. The trap can be closed after injection by applying an electrostatic potential to the entrance electrode. After storing the ions for a defined trapping time, the ions are extracted from the trap using a pulse on the exit electrode and analysed using a second quadrupole mass filter. This procedure is applied repeatedly for different trapping times until a sufficient signal to noise ratio is achieved. The rate coefficients for a given conditions (e. g. T_{22pt} , T_{ACC} , number density of neutrals) are then

extracted from the time evolutions of charged reactants/products in the trap.

4.2 THE $H^- + H$ SYSTEM

4.2.1 Role of H^- in primordial astrochemistry

The evolution of primordial matter in the early universe toward the formation of the first stars is determined by atomic and molecular processes involving mainly hydrogen (H, D), helium (^3He , ^4He), electrons and radiation. The elemental composition of the medium remained unchanged during this period, one could have expected that the primordial chemistry is rather simple. However, up to 200 reactions can contribute to the abundance of 23 atomic and molecular species as pointed out by Lepp et al. (2002). The role of molecules as coolants (i. e., the conversion of translational energy into internal degrees of freedom via inelastic or reactive collisions), followed by radiative transitions, is important for star formation.

There has been significant progress in improving the models, which predict abundances of molecules and their role as coolants. However, all these models use only simple temperature dependent rate coefficients for characterising most of the chemical reactions. The uncertainty in the knowledge of these rate coefficient introduces uncertainties of several orders of magnitude into these models (e. g. uncertainties in formation of protogalaxies (Glover et al., 2006)).

Formation of a hydrogen molecule from two H atoms under early universe conditions requires a catalytic gas phase reaction such as $H^+ + H \rightarrow H_2^+ + h\nu$ followed by $H_2^+ + H \rightarrow H_2 + H^+$. Besides the proton, an efficient catalyst is the electron, as soon as the lifetime of H^- gets long enough. The sequence is radiative attachment $e^- + H \rightarrow H^- + h\nu$, followed by *Associative Detachment* (AD)



Despite direct observations of anions in the interstellar medium (first observation published by McCarthy et al. (2006), several more anionic species observed since then (Cernicharo et al., 2007; Brünken et al., 2007)) and its abundance, H^- has not yet been observed directly by its specific transition (in the UV region as stated by Ross et al. (2008)). Thought, indirect observations proving its presence in space exists (Heap and Stecher, 1974). The central role of H^- and AD in the primordial chemistry have been discussed by Glover et al. (2006);

Glover (2008). Investigation of the AD reaction on the AB 22-pt apparatus is going to be described together with comparison with previous measurements and theoretical calculations (section 4.2.3).

4.2.2 Determining the rate coefficient using the 22-pole trap

The geometry of the interaction region where the neutral beam interact with the trapped ion cloud is shown in detail in figure 19. Primary

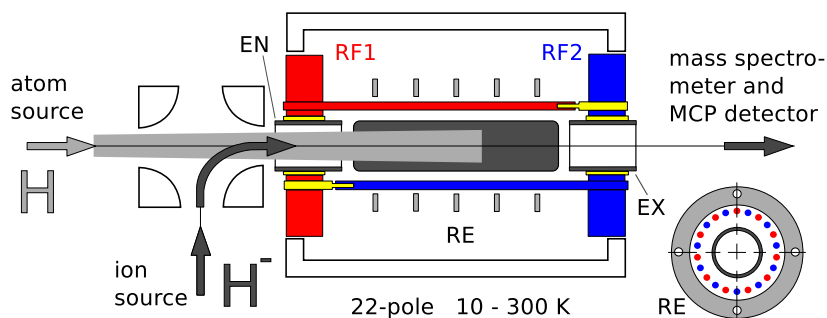


Figure 19: Detailed drawing of the central part of the 22-pole ion trap apparatus. H^- anions are injected into the trap via the electrostatic quadrupole bender. To the right, anions move via the quadrupole mass spectrometer towards the detector. The cold effusive H-atom beam comes from the left. The gray shaded areas indicate the overlap between the anion cloud and the neutral beam. For photodetachment studies, a laser beam is injected from the right (more in text). Adopted from Gerlich et al. (2012).

H^- ions are produced by electron bombardment of H_2 precursor gas in the SIS (section 3.1). After pre-thermalization in the source, the H^- anions are mass selected using a quadrupole filter, bent by 90° using an electrostatic quadrupole (figure 7) and injected into the 22-pole trap. In the radial direction, the ions are confined by the rf field created by two sets of 11 poles (RF1 and RF2) precisely mounted on both sides. The potential inside the trap can be corrected locally using the five ring electrodes (RE). The entrance and exit electrode (EN and EX) are used to open and close the trap with electrostatic barriers of approximately 10 meV. After various storage times, the ions are extracted from the trap by opening the exit electrode. Afterwards, the ions pass through the QP mass spectrometer to be converted into a short current pulse using an MCP, and finally accumulated in a counter.

The H atoms were produced in an rf discharge in H_2 operating at 20 Pa and a gas flow of $5 \cdot 10^{-4} \text{ Pa m}^3 \text{ s}^{-1}$. The H atom effective

Table 2: Diameter of the ion cloud (d_1 for H^- and d_2 for CO_2^+) for different kinetic energies E of the ions calculated from the effective potential (45). Adopted from Gerlich et al. (2012).

E meV	d_1 (H^-) (mm)	d_2 (CO_2^+) (mm)	$(d_1/d_2)^2$
100	9.21	8.17	1.271
10	8.21	7.28	1.272
1	7.32	6.49	1.272

Note: The 22-pole has been operated with $\Omega/2\pi = 18$ MHz and $V_0 = 50$ V and 25 V for mass 44 and 1 u respectively. Note that the inner free diameter of the 22-pole is 10 mm. As long as the kinetic energy distributions of CO_2^+ and H^- are the same, the volume of the CO_2^+ cloud is about 1.27 times the volume of the H^- anions. This can be seen from $(d_1/d_2)^2$, the ratio of the areas.

number density in the trap has been calibrated using the chemical probing with CO_2^+ ions as described in section 3.3.3 with a result

$$N_{\text{H}} = (1.3 \pm 0.6) \cdot 10^8 \text{ cm}^{-3}. \quad (60)$$

The estimated 45% error is caused mainly by the 40% uncertainty in the rate constant of the $\text{CO}_2^+ + \text{H} \rightarrow \text{HCO}^+ + \text{O}$ reaction (Borodi et al., 2009) in combination with 20% error estimate of our measurement. The presented result was measured at accommodator temperature $T_{\text{ACC}} = 50$ K. The value is corrected for different shapes of CO_2^+ and H^- ion clouds, so that it is valid for H^- ion cloud under the operating conditions used in this experiment (table 2).

The standard sequence of

1. filling the trap repetitively with a well defined number of primary ions ($N(t=0) \approx 100$),
2. storing them for various storage times t ,
3. detecting them,

is averaged over many iterations, to reduce the statistical errors. For comparison – typical raw data (the number of ions $N_i(t)$, normalized to the total number of ions in one iteration) is shown in figure 20. In the present experiment, the charged products from the AD reaction are electrons which cannot be detected in the current setup, thus only

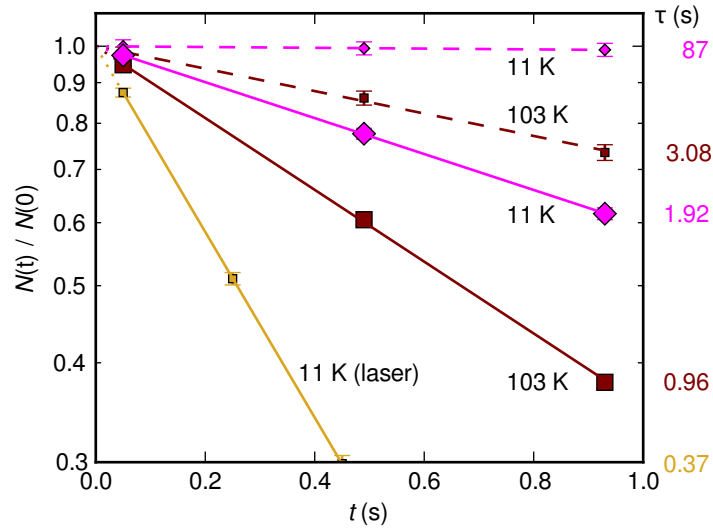


Figure 20: Relative number of H^- anions per filling as a function of storage time (ion trap temperature: $T_{22\text{pt}} = 11$ and 103 K, hydrogen beam temperature $T_{\text{ACC}} = 50$ K), small and large symbols correspond to H-atom beam OFF and ON, respectively. Yellow line corresponds to laser photodetachment (used for testing purpose only). The statistical errors are in the order of or smaller than the size of the symbols. Fitting the data with $\exp(-t/\tau)$ (solid and dashed lines) lead to the time constants τ shown on the right. Adopted from Gerlich et al. (2012).

the decrease of primary anion H^- is monitored. Single measurements have been repeated with period of 1 s. The number of ions in trap was first checked after 50 ms, when most of them have already been thermalized in collisions with cold ambient molecular hydrogen. Typical H_2 densities have been 10^{12} cm^{-3} , originating mainly from the ion source precursor H_2 . Higher densities have also been tested without any effect. Extracting the ions at later times reveals a more or less slow loss, depending on the temperature of the trap and on the presence of the H atom beam. The data have been fitted with exponential decay functions, resulting in time constants τ longer than 1 minute without H atoms and shorter than 1 s with H atoms (numbers on the right side of figure 20). The slow loss of primary ions, without H atoms, is caused by reactions with ambient background gas. At 11 K, cryopumping inside the trap leads to long confinement times. To extend the measurements toward higher temperatures, better vacuum conditions are needed. The rate coefficients of reaction (59) are simply

determined from the difference of the rates with the H beam ON and OFF and the effective number density of the H atoms.

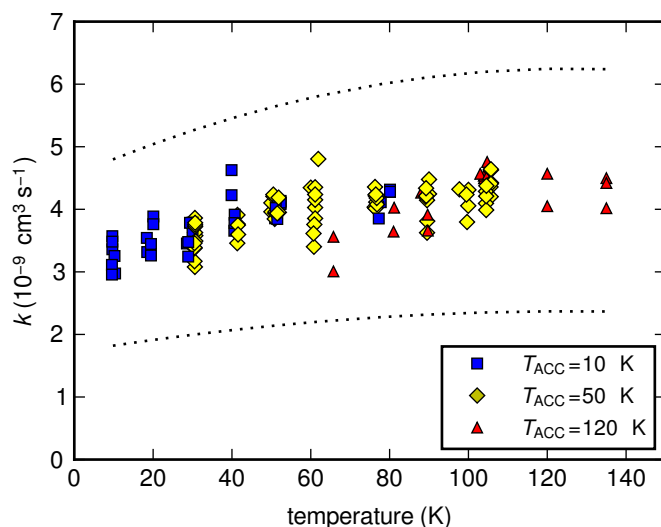


Figure 21: Measured rate coefficients (reaction (59)), shown as a function of the translational temperature. The data shown as squares, diamonds, and triangles have been measured at $T_{\text{ACC}} = 10, 50,$ and 120 K respectively. Variation of $T_{22\text{pt}}$ between 10 and 150 K covers each time a range of 70 K (in the center-of-mass system). The dotted lines indicate the systematic error estimate. Adopted from Gerlich et al. (2012).

The temperature dependence of the rate coefficient was measured by varying the 22-pole temperature in the range $10 \text{ K} < T_{22\text{pt}} < 150 \text{ K}$ with fixed accommodator temperature. The upper limit for $T_{22\text{pt}}$ is caused by the loss of H^- anion caused by the presence of impurities at temperatures over 150 K . Due to the kinematic averaging (section 3.4.2), the reaction temperature T is

$$T = \frac{T_{\text{ACC}} + T_{22\text{pt}}}{2}. \quad (61)$$

With single T_{ACC} , the rate coefficient can be measured in the range of 70 K . The total measurement range was extended by measuring at three different T_{ACC} ($10, 50,$ and 120 K). The effective density of atomic hydrogen N_{H} was obtained by chemical probing at $T_{\text{ACC}} = 50 \text{ K}$. The N_{H} at other accommodator temperatures was determined by least squares fitting of the uncalibrated rate constant measurements to the calibrated data in the region of their overlap. The results of this procedure are illustrated in figure 21, where the data measured

at different accommodator temperatures are represented by different symbols. The systematic error margin due to the H beam calibration is indicated by a dotted line in the figure. It has to be noted, that the systematic error is contained in a single multiplicative factor and hence does not affect the overall observed trend.

4.2.3 Comparison with theoretical calculations and previous measurements

In order to simplify the comparison with other measurements and theory, the calibrated data were reduced by binning. The result is plotted in figure 22. The errorbars represent the standard deviation of our data points. The figure shows, that our results are in a good agreement with the theory of Čížek et al. (1998). At higher temperatures, where the theory of Čížek et al. (1998) differs significantly from the theory of Sakimoto (1989), our data support the theory of Čížek. Since the theory of Sakimoto is specialized for energies below 10^{-2} eV this outcome has been expected.

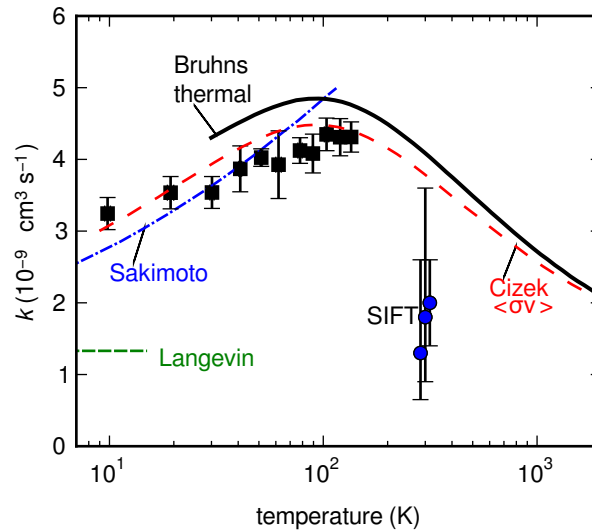


Figure 22: Comparison of our ion trap results (squares, bars indicate the statistical errors, the systematic uncertainty is larger, see text) with previous measurements and results from theory. The solid line indicates the thermal rate coefficient $k(T)$, derived from the merged beams data published by Bruhns et al. (2010). The theoretical results of Sakimoto (1989) and Čížek et al. (1998) are in good overall agreement, while the Langevin limit and the 300 K flow tube measurements are significantly smaller (from left to right: Schmeltekopf et al. (1967); Fehsenfeld et al. (1973) and Martinez et al. (2009) (shifted in temperature for better readability). Adopted from Gerlich et al. (2012).

Although our measurements cannot be directly compared to the older flow tube measurements (Schmeltekopf et al., 1967; Fehsenfeld et al., 1973; Martinez et al., 2009) due to the different temperatures, they are in good agreement with the recent merged beam experiment (Kreckel et al., 2010; Bruhns et al., 2010) in the overlapping temperature range.

4.3 REACTION OF ATOMIC OXYGEN ANION WITH H₂ – WATER PRODUCTION

Reactions of atomic oxygen anion O⁻ and molecular hydrogen have already been studied in the past by McFarland et al. (1973); Moruzzi and Phelps (1966). However, the reaction rate coefficient below 300 K remained unexplored until now (older data are measured from 0.04 eV and 0.4 eV respectively).

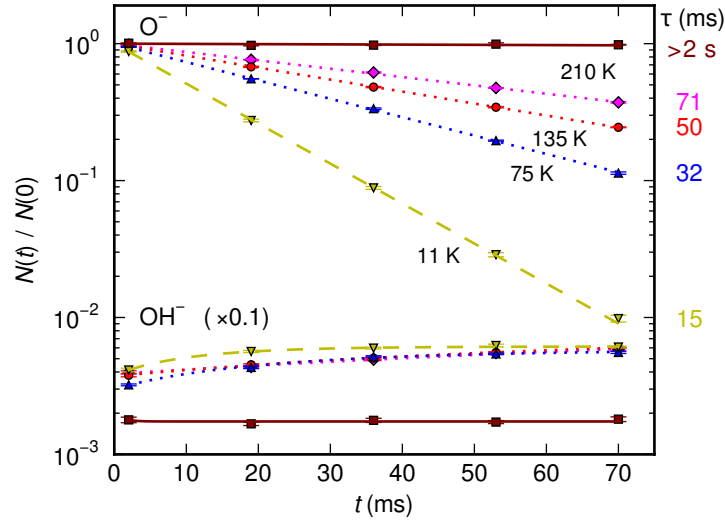


Figure 23: Relative number of O⁻ and OH⁻ anions per filling as a function of storage time (ion trap temperature: $T_{22pt} = 11, 75, 135,$ and 210 K), Upper lines correspond to the decrease of O⁻ anion relative number. Lower lines correspond to the increase of OH⁻ anion number (scaled by factor 0.1 for better readability). Maroon square symbols correspond to the measurement without H₂, remaining data are recorded with H₂ present in the trap. The statistical errors are smaller than the size of the symbols. Fitting the data for O⁻ relative number with $\exp(-t/\tau)$ (upper lines) leads to the time constants τ shown on the right.

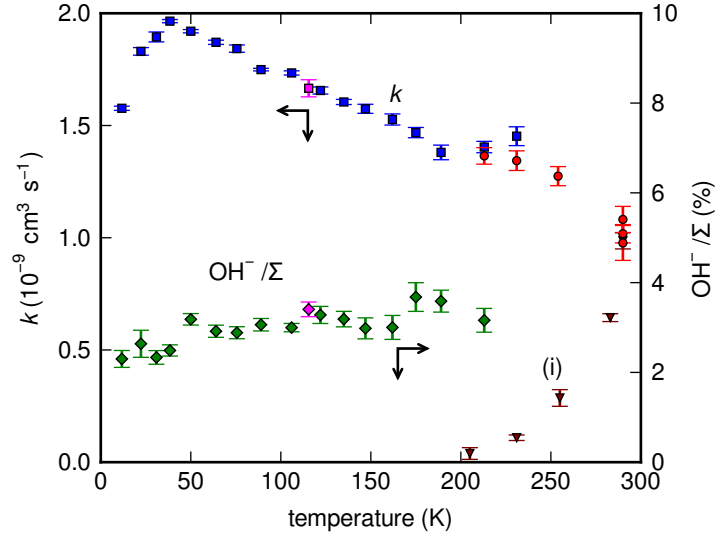
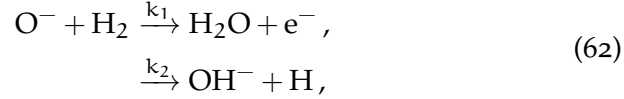


Figure 24: Measured rate coefficient k (reaction (62)), shown as a function of the temperature (squares). At higher temperature, the correction (red circles) for the losses induced by reaction with the background gas (triangles, (i)) is needed. The rate coefficient k_2 is expressed as a ratio of the number of OH^- ions produced to the number of O^- ions lost (diamonds, right ordinate).

The reaction has two possible exothermic channels for the products



of which only the second one produces ions, which are confined in the trap. We are not able to detect the produced water molecule and electron in the 22-pt apparatus, for detection of electron see section 5.4.1.

The O^- anions are produced in SIS from N_2O and after being mass selected in the first quadrupole, they are injected into the trap. The raw data, as plotted in figure 23, are interpreted as follows. First the total reaction rate k ($k = k_1 + k_2$) is calculated from the time evolution of the relative number of the primary O^- ions in the trap using a dependency in form of $N_{\text{O}^-}(0) \exp(-t/\tau)$, where t is the storage time and τ is the characteristic confinement time for a given temperature and number density of the molecular hydrogen (for number density determination in the 22-pole trap see Asvany (2004)). The increase of relative number of the OH^- ion in the trap is approximated by the function in form of $N_{\text{O}^-}(0) \frac{k_2}{k} (1 - \exp(-t/\tau)) + N_{\text{OH}^-}(0)$. If we assume that the detection efficiency for O^- and OH^- is the same,

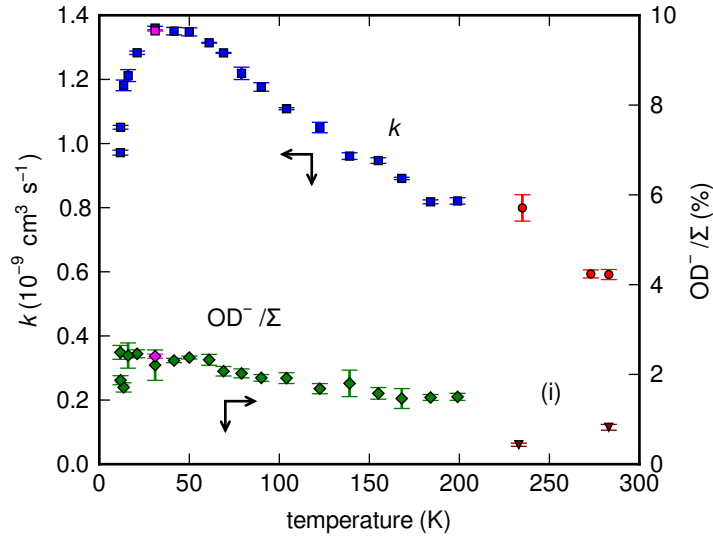
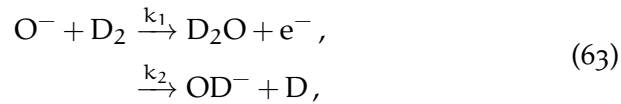


Figure 25: Measured rate coefficient k for the reaction of $O^- + D_2$, shown as a function of the temperature (squares). At higher temperature, the correction (red circles) for the losses by reaction with the background gas (triangles, (i)) is needed. The rate coefficient k_2 is expressed as a ratio of the number of OD^- ions produced to the number of O^- ions lost (diamonds, right ordinate).

then we can write $k_1/k = N_{OH^-}(t)/(N_{O^-}(0) + N_{O^-}(t))$. In this way the decoupling of k_1 , k_2 is possible even without the possibility of detection of electrons produced in AD reaction (62). The measured temperature dependences of k together with the branching ratio for reaction (62) are shown in figure 24.

The isotopic variant of the reaction (62) with D_2



has also been investigated. The results are plotted in figure 25. The reaction rate r is linearly proportional to the number density of the molecular reactant gas (figure 26). This leads us to the conclusion that the reactions (62) and (63) are a binary process. The temperature dependence of the reaction rate coefficients is not an apparatus effect (section 3.4.1).

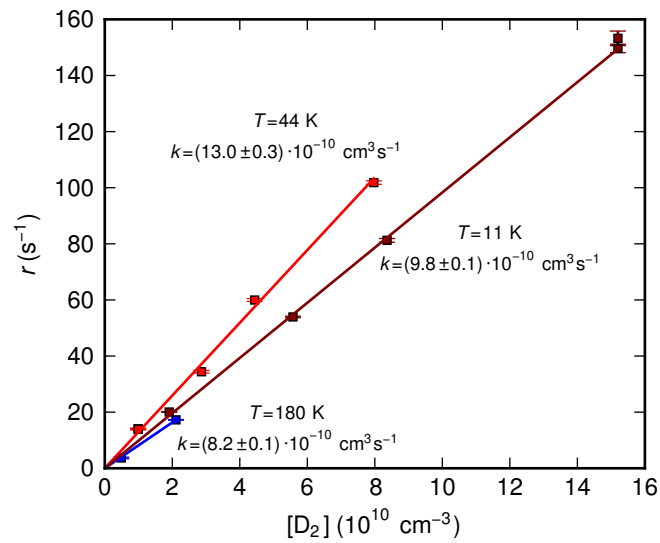


Figure 26: Measured $\text{O}^- + \text{D}_2$ reaction rate r as a function of D_2 number density for three different temperatures $T = 11, 44,$ and 180 K . Linear fit in form of $r = k[\text{D}_2]$ through axes origin reveals binary reaction rate coefficient k . We are also certain that the eventual condensation of the neutral gas on the [22-pt](#) walls is not significant.

4.3.1 Comparison with previous measurements

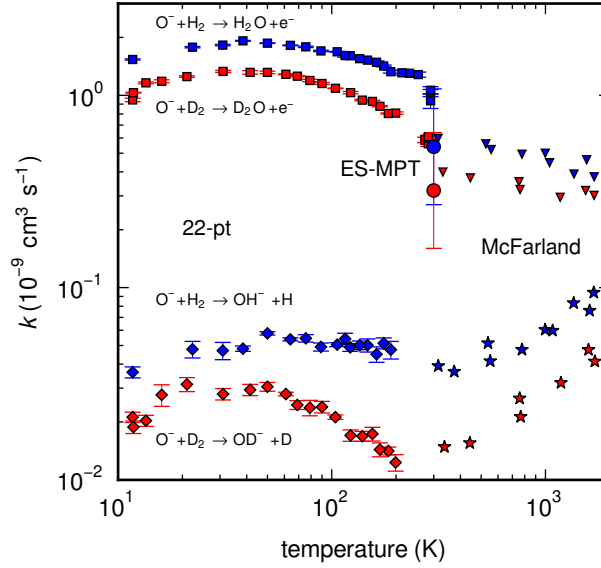


Figure 27: Comparison of our ion trap results (squares and diamonds, bars indicate the statistical errors) with previous measurements of McFarland et al. (1973) (stars and triangles) and measurements done at the ES-MPT apparatus (circles at 300 K, section 5.4.1). All three measurements overlap at approximately 300 K and are in overall good agreement.

The reactions (62), (63) have been studied by McFarland et al. (1973) using a flow-drift tube technique (from 0.04 to 0.5 eV). The apparatus described in chapter 5, though not primarily designed to measure the rate coefficients, has also been used to investigate the reactions (62), (63) at 300 K. These results are compared in figure 27 together with the data recently measured at the 22-pt setup (from 10 to 300 K). The data acquired at 300 K are also compared in table 4 in section 5.4.1.

4.3.2 The isotope effect

We summarise the isotope effect between H₂ and D₂ in the reaction with O⁻ in figure 28. To emphasize the effect, we show the data measured (figure 27) divided by the Langevin rate coefficient for corresponding ion neutral reaction in the form

$$k_{\text{Lang}} = 2\pi e \sqrt{\frac{\alpha_n}{\mu}}, \quad (64)$$

where e is the elementary charge, α_n is the neutral molecule polarizability, and μ is the ion-neutral reduced mass (Eichelberger et al., 2003). Polarizability α_n for H_2 and D_2 molecules at 77 K can be found in Milenko et al. (1972) (temperature dependence of polarizability is negligible).

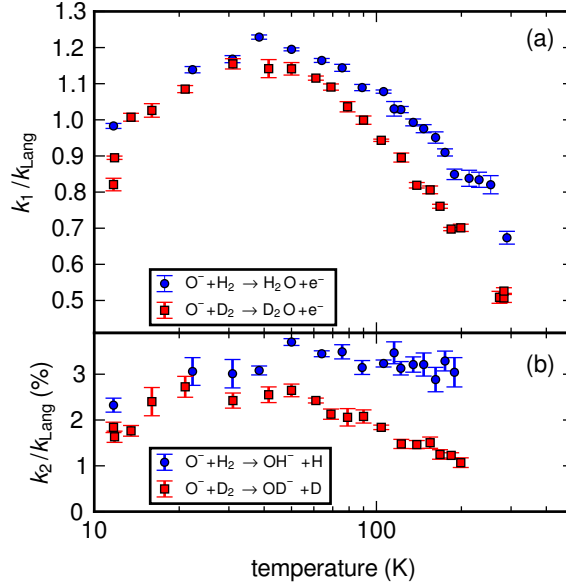


Figure 28: Isotope effect observed in the reaction of O^- with H_2/D_2 (reactions (62), (62)). The measured reaction rate coefficients are divided by the corresponding Langevin rate coefficients (see text). Panel (a) – associative detachment channel (k_1). Panel (b) – OH^- and OD^- production channel (k_2).

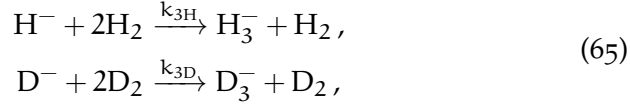
One can observe, that the isotope effect is not simply explainable by the change in reduced mass of reactants as suggested by Langevin’s simple point charge and point-polarizable neutral attractive model.

4.4 IS FORMATION OF $\text{H}_3^-/\text{D}_3^-$ POSSIBLE IN THE 22-POLE TRAP?

Negative triatomic anions H_3^- and D_3^- have already been produced in dielectric barrier discharge (Wang et al., 2003). The lifetime of such anions is infinite, although binding energy of such anions is in order of 0.013 eV (for H_3^-) according to Ayouz et al. (2010). Thus even collision at room temperature can lead to destruction and they have not been observed in the ISM yet. The H_3^- anion can not be formed directly by radiative attachment from unstable H_3 molecule, other processes have to be considered – *Radiative Association (RA)* or three body

(ternary) association. The radiative association rate coefficient of H^- with H_2 has been calculated by Ayouz et al. (2011), the result in order of $10^{-23} \text{ cm}^3 \text{ s}^{-1}$ at 10 K reveals that the process is many orders of magnitude slower than we are able to investigate in our experimental setup. However, the RA is probably more important than a ternary process in the ISM due to low H_2 density.

In this work, we focused on the ternary association reaction



which is a dominant process of creation according to Wang et al. (2003). We were not able to detect H_3^- or D_3^- directly as mass 3 or 6 u respectively in the mass scan. However, we can try to estimate the upper limit for reaction rate coefficients. Figure 29 shows a relative number

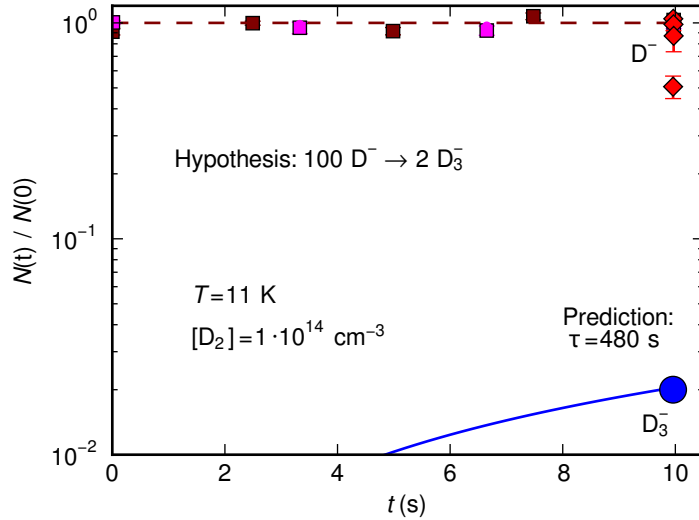


Figure 29: Relative number of D^- per filing as a function of storage time. Measured data are shown using squares and diamonds. Dashed line represents the exponential fit (essentially a constant). Blue full line and circle represent the hypothetical position of D_3^- (2% of $N(t=0)$) detected.

of D_3^- ions in trap as a function of storage time. This time we did not use the exponential decay fit to investigate the reaction rate, instead we formulate a hypothesis that if the reaction is proceeding we are able to detect at least 1–2% of the primary ions converted in product ions at the longest trapping time t_{max} used. We can reformulate this problem, taking into account that the sum of reactant and products is

constant, in relative number densities of reactants, we get a hypothetical time constant

$$\tau_H = \frac{-t_{\max}}{\ln(N(t_{\max})/N(0))}. \quad (66)$$

In figure 29 we used more than 10^4 D^- ions at storage time $t_{\max} = 9.97$ s, thus our requirement of 1–2% would lead to hypothetical detection of at least 100 D_3^- ions created. Using equation (66) we are able to calculate a time constant $\tau_H \geq 480$ s. We used the highest pressure of the molecular D_2 possible in our experimental setup, leading to number density $N_{D_2} \geq 1 \cdot 10^{14}$ cm^{-3} . Measured constraints lead us to the conclusion that the rate coefficient for the ternary creation of D_3^- is

$$k_{3D} < 1 \cdot 10^{-31} \text{ cm}^6 \text{ s}^{-1}. \quad (67)$$

Similar experiments have also been done for H^- and molecular hydrogen with the same conclusion for the hypothetical time constant and the reaction rate coefficient.

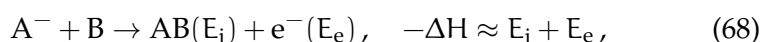
ASSOCIATIVE DETACHMENT AND THE ELECTRON SPECTRA

For the purpose of studying the associative detachment reactions, we have developed a novel experimental technique, which is capable of measuring the energy distribution of electrons produced in the associative detachment reaction of ions stored in an ion trap. The subject of this chapter is the description of the *Electron Spectrometer with Multipole Trap* (ES-MPT) instrument together with construction details, experimental characterization, calibration, and selected first experimental results.

The measurements presented in this chapter were submitted to IJMS (see Article II).

5.1 ASSOCIATIVE DETACHMENT

The associative detachment (AD) is an anion-neutral reaction which can be formally described as



where E_i is the energy of the internal excitation of the molecule and E_e is the kinetic energy of the electron. Thanks to the high mass of the molecule compared to the electron, the kinetic energy of the produced molecule can be neglected. The reaction proceeds via a compound state AB^- , which decays by autodetachment. The redistribution of the internal energy of AB^- between E_i and E_e is – within the kinematic constraints – determined by the internal structure of the AB^- complex (Čížek et al., 1998; Smith and Leone, 1983).

The importance of AD reaction studies, especially in the field of astrophysics, has been emphasized recently by Glover et al. (2006). Since then several experimental setups were used to measure the AD reaction rate coefficient (Martinez et al., 2009; Kreckel et al., 2010; Gerlich et al., 2012) exclusively. It has also been shown by Živanov et al. (2003) that the measurements of the energy of the detached electrons are a useful tool for benchmarking of the theoretical description of the AD process.

The reactions of O^- with H_2 (theoretical description in Claydon et al. (1971); Werner et al. (1987); Haxton et al. (2007))





their isotopic variants with D_2 , and the reaction of O^- with CO



are used in this work as a model systems to demonstrate the capabilities of the presented experimental setup. The exothermicities of the reactions with H_2 are given by Claydon et al. (1971) and the exothermicity of the reaction with CO by Abouaf et al. (1976). The uncertainty of these values is smaller than 0.1 eV. The product energy distributions of reactions (69) and (70) have been studied by Mauer and Schulz (1973) and partly by Esaulov et al. (1990). Furthermore, strong unexpected isotopic effects have been observed in the product energy distribution of reaction (70) with H_2/D_2 as reactants (Lee and Farrar, 1999).

5.2 THEORY OF OPERATION

The ES-MPT instrument is a combination of an electron spectrometer with an rf ion trap. These two devices are combined in such a way that the ion trap is located inside the input region of the electron spectrometer (see schematic diagram in figure 30 and CAD drawing of the apparatus in figure 45 in Appendix A).

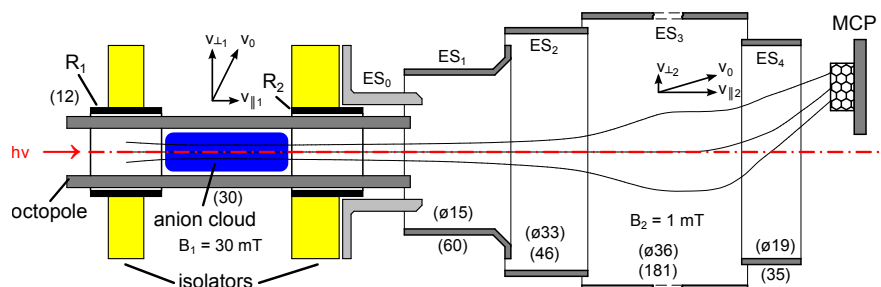


Figure 30: Schematic diagram of the ES-MPT apparatus (not to scale). The principle of combination of the radiofrequency ion trap (octopole on the left side) and the MAC-E filter (right side). Anions are injected into the octopole trap from the left and confined axially using the electrostatic ring electrodes (R_1, R_2). Laser radiation can be applied along the axis, reactant gas can be introduced into the trap between R_1, R_2 . Produced electrons are magnetically guided to the region with lower magnetic field (B_2) and refocused to the MCP detector. Cylindrical electrodes ES_0 – ES_4 create the electrostatic barrier (diameter and length in parentheses are in mm).

Thanks to the high mass ratio and different energies of the anions and electrons, we can choose such operating conditions that the an-

ions are governed mainly by the rf field of the trap and the produced electrons mainly by the magnetic field of the electron spectrometer.

Although the rf ion traps in magnetic field have been used in experiments such as Fourier transform mass spectrometers (Beu et al., 2011), magneto-optical traps (Rellergert et al., 2011), and photoelectron spectrometers (Moseler et al., 2003) before, we believe that our instrument is unique in its ability to extract and analyze the electrons produced in the rf ion trap.

5.2.1 MAC-E filter

One of the principal components of the ES-MPT setup is the MAC-E filter – *Magnetic Adiabatic Collimation combined with an Electrostatic filter*. This device guides the produced electrons using magnetic field and filters them according to their energy with good resolution regardless of their initial velocity direction. This type of instrument was first described by Beamson et al. (1980) and is used in many particle physics experiments (KATRIN collaboration, 2005), where the produced light charged particles have random initial velocity direction. In such cases, filtering of the particles by a retarding potential barrier is not directly applicable, because the barrier acts only on the randomly distributed projection of the velocity parallel to the electric field.

The principle lies in the adiabatic invariance of magnetic moment μ of electrons with mass m_e :

$$\mu = \frac{E_{\perp}}{B}, \quad (72)$$

where B is the magnitude of the magnetic field, E_{\perp} is the kinetic energy associated with the particle velocity perpendicular to the magnetic field vector. For detailed derivation of the magnetic momentum concept and invariance see section 2.1.3.

The magnetic field configuration of the MAC-E filter consists of two regions with magnetic field intensities $B_1 \gg B_2$. We will denote these regions as strong-B and weak-B in the text. The electrons are produced in the strong-B region (B_1) and guided along the magnetic field lines into the weak-B region (B_2). Thanks to the conservation of magnetic moment μ , the initial energy of the perpendicular motion $E_{\perp 1}$ is reduced to

$$E_{\perp 2} = E_{\perp 1} \frac{B_2}{B_1} \quad (73)$$

in the weak-B region and because of the energy conservation, the energy of the perpendicular motion E_{\perp} must be transformed into the

energy of motion parallel to the magnetic field (E_{\parallel} , associated with parallel velocity v_{\parallel}). The electron velocities become collimated and their energies can be analysed simply by placing a variable retarding potential barrier into the weak-B region.

Assume that an electron with charge q_e is produced in the strong-B region with velocity v_0 , energy E_0 , and velocity projection parallel to magnetic field $v_{\parallel 1}$ (figure 30). To pass through the potential barrier $E_B = q_e U_B$ in the weak-B region, the energy of the parallel motion must satisfy $E_{\parallel 2} > E_B$ (we set the reference zero potential in the center of the trapping area). This condition can be rewritten in terms of the initial values using equation (73) and the law of energy conservation:

$$\frac{v_{\parallel 1}}{v_0} > \sqrt{1 - \left(1 - \frac{E_B}{E_0}\right) \frac{B_1}{B_2}}. \quad (74)$$

We calculate the response of the MAC-E filter to a monoenergetic isotropic source of electrons analytically in order to understand the transmission properties of the MAC-E filter relevant for our experiment. The probability distribution of the velocity component $v_{\parallel 1}$ is uniform in the interval $[-v_0, v_0]$. Therefore, the fraction of particles satisfying (74) is simply calculated as

$$P_T\left(\frac{E_B}{E_0}\right) = \frac{1}{2} \left(1 - \sqrt{1 - \left(1 - \frac{E_B}{E_0}\right) \frac{B_1}{B_2}}\right). \quad (75)$$

The factor 1/2 accounts for the particles with initial velocity in the direction away from the spectrometer. We neglect it in the further discussion, since these particles can be reflected back to the spectrometer by placing a high electrostatic barrier on their escape path. Evaluation of the extreme cases leads to the transmission function of the spectrometer

$$P_T\left(\frac{E_B}{E_0}\right) = \begin{cases} 1 & \frac{E_B}{E_0} \leq 1 - \frac{B_2}{B_1} \\ 1 - \sqrt{1 - \left(1 - \frac{E_B}{E_0}\right) \frac{B_1}{B_2}} & 1 > \frac{E_B}{E_0} > 1 - \frac{B_2}{B_1} \\ 0 & \frac{E_B}{E_0} \geq 1. \end{cases} \quad (76)$$

The electron spectrum is obtained by differentiating the retarding curve. Hence the relative resolution ΔE of the filter can be calculated by differentiating the transmission curve for monoenergetic electrons (76). We define the relative resolution as the width of the support of the obtained energy distribution peaks

$$\Delta E = E_0 \frac{B_2}{B_1}. \quad (77)$$

The expression (76) is also useful in estimating the efficiency of extracting the electrons from the ion trap. A small potential barrier $U_T \approx -0.3$ V, which is used to trap the anions, can prevent some electrons from leaving the trap. Since the magnetic field in the trap is nearly constant, we can evaluate the extraction probability P_E by setting $B_1/B_2 = 1$ in equation (76). Expressing the result in terms of the electron energy E_e and trapping potential U_T leads to

$$P_E(E_e, U_T) = 1 - \sqrt{\frac{q_e U_T}{E_e}} \quad (78)$$

for $E_e > q_e U_T$, otherwise the probability is zero.

5.2.2 Radiofrequency ion trap

The radiofrequency (rf) multipole traps are well understood and widely used for trapping of charged particles as has been described in sections 2.4 and 4.1. Linear radiofrequency octopole is used to guide and trap the anions in the radial direction in the ES-MPT. In the axial direction, the ions are trapped by electrostatic barriers. To trap an anion of mass M and charge q , the rf field of an amplitude V_0 creating an effective potential V^* greater than the particle kinetic energy E is needed. In the adiabatic approximation (section 2.4.1), the effective potential of a linear octopole as a function of the reduced radius $\hat{r} = r/r_0$ is given by

$$V^*(\hat{r}) = \frac{n^2}{4} \frac{q^2}{M\Omega^2} \frac{V_0^2}{r_0^2} \hat{r}^6, \quad (79)$$

where Ω is the rf field angular frequency, r_0 is the inscribed radius of the octopole (3 mm in our case), r is the radial coordinate.

The minimal rf amplitude V_0 necessary for trapping the ions is given by a requirement that the turning radius of the ions must be within a safe distance from the rods, typically smaller than $0.8 \cdot r_0$, as discussed in section 2.4.3. This imposes a condition $V^*(0.8) \geq E$. Under the typical operating conditions in our experiments with trapped O^- anions, $\Omega/2\pi = 4.4$ MHz, $V_0 = 10$ V, and the effective potential at the safe turning radius is $V^*(0.8) = 0.05$ V. These conditions are just sufficient for trapping of thermal anions at 300 K and significant lowering of the rf amplitude is not possible without the decrease of the frequency. The adiabatic theory is not applicable to the interaction of electrons with rf fields in our conditions. The residence time of electrons in the rf field is comparable to the rf period and no simple analytic description is available. Therefore, we used a computer model

of the spectrometer described in Roučka (2012) to investigate potential problems with this interaction.

In the particular case of the ES-MPT instrument, the ion trap is operated in magnetic field. The problem of ion motion in such combined fields has been studied theoretically (Chun-Sing and Schuessler, 1981; Huang et al., 1997; Li, 1989; Dodin and Fisch, 2005; Dodin and Fisch, 2006). In our experimental conditions, the magnetic field is relatively weak, i. e., the cyclotron frequency is much smaller than the rf frequency. We have verified by numerical simulations that, in such cases, the adiabatic theory and equation (79) remain valid. The experimental confirmation is presented in section 5.3.2.

5.3 EXPERIMENTAL SETUP

The ES-MPT (figure 30) is an UHV apparatus with background pressures $< 1 \cdot 10^{-7}$ Pa. The storage ion source, trapping area, and MAC-E filter vacuum vessels are each pumped by its respective magnetically suspended turbomolecular pump (total of 3).

The anion part of the apparatus consists of the anion source (section 3.1), quadrupole mass spectrometer (section 3.1), guiding octopole, and the trapping octopole area (Glosík et al., 2000). The O^- anions are produced in the SIS by electron bombardment of the precursor gas (N_2O) and are mass selected in the quadrupole before injection into the trap.

The trapping area is enclosed in a scattering cell with a separate gas inlet system for introduction of a reactant gas. The octopole rods are 2 mm thick ($r_r = 1$ mm), spaced on a circle with 6 mm inner diameter ($r_0 = 3$ mm). The lowest usable rf amplitude for O^- is 10 V as discussed in section 5.2.2. The axial trapping barriers are created using ring electrodes R_1, R_2 located outside of the octopole (rings with inner diameter 12 mm and length 10 mm). The ring electrode R_2 is also responsible for the trapping potential U_T described by equation (78).

No cooling or heating of the reaction area is implemented, the experiments are conveyed at room temperature.

The apparatus is optically transparent along the axis of the octopole so that laser radiation can be used to photodetach the trapped anions. A microchannel plate (MCP) detector (section 3.2) is used for detection of ions and electrons. The detector is located off axis in order to retain the optical transparency of our setup.

The strong-B region of the MAC-E filter is coincident with the ion trap location and the field is parallel to the trap axis in order to ex-

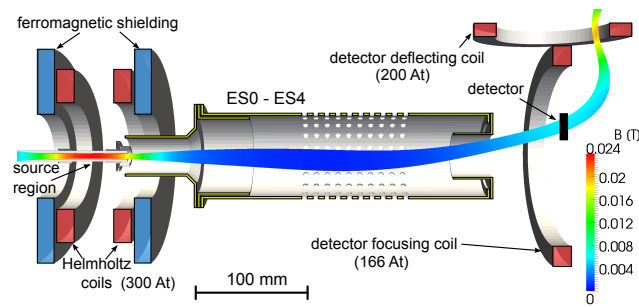


Figure 31: Configuration of the electrodes, coils, and ferromagnetic elements of the electron spectrometer. The calculated color-coded magnetic field intensity is projected on the calculated magnetic flux tube emanating from the ion trap. The flux tube approximately represents the possible electron trajectories. The number of ampere-turns (At) used for producing the magnetic field is indicated for each coil.

tract the produced electrons. The magnetic field for the MAC-E filter is produced with standard enamelled copper wire coils (4 in total) located outside of the vacuum chamber. Two coils in approximately Helmholtz configuration are used to generate the strong magnetic field in the trapping area. These coils are surrounded by ferromagnetic steel rings, which enhance the gradient of the magnetic field between the strong- and weak-B regions, thus reducing the dimensions of the filter. The other two coils are used to focus and deflect the filtered electrons to the off-axis detector.

The suitable configuration of coils and ferromagnets was designed using computer simulations with the FEniCS software (Logg and Wells, 2010; Logg et al., 2012) (figure 31, for details see Roučka (2012)) and verified by measurements with a Hall probe (figure 32).

The highest magnetic field intensity (in the trapping area) is $B_1 = 30 \text{ mT}$, the lowest magnetic field in the electrostatic barrier region is $B_2 = 1 \text{ mT}$. The theoretical resolution of the MAC-E filter is thus approximately 3 %.

All electrodes are made from austenitic (non-magnetic) stainless steel. The MAC-E filter parts were newly designed for this setup. The shape of the electrodes ES0–ES4 was optimized to provide an accurate potential barrier coincident with the minimum of the magnetic field intensity. The calculated inhomogeneity of the barrier is smaller than 1 %. The optimization was carried out using the Elmer software¹.

¹ URL: <http://www.csc.fi/english/pages/elmer>

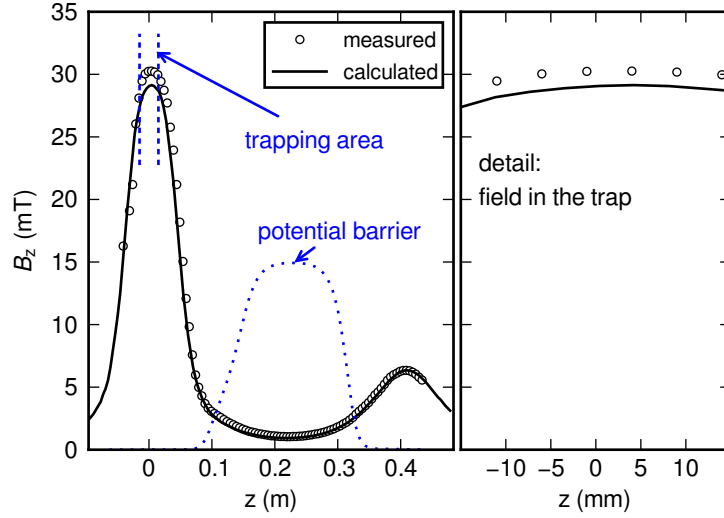


Figure 32: Measured magnetic field generated by the Helmholtz coils and the focusing coil with 4.5 A current (using a hall probe). The zero on z axis is set into the center of symmetry of the Helmholtz coils. The area between the end electrodes, is indicated in the left panel and it is shown in detail in the right panel. The shape of the retarding electrostatic barrier (located in $z \approx 0.2$ m) is indicated by the dotted line.

The measurement of electron spectrum proceeds by measuring the electron flux I_e (number of detected electrons per second) as a function of the electrostatic barrier height U_B . This way we directly measure the integral spectrum and the differential spectrum is obtained by numerical differentiation with smoothing using the Savitzky-Golay filter. Unless stated otherwise, the differential spectra are always normalized to unit area.

The ES-MPT is highly modular and several configurations have been used to obtain the results presented. These modifications are going to be described in the text when relevant.

A number of test measurements in different configurations were performed in order to understand the properties of this unique instrument and in order to properly calibrate the energy resolution. The following subsections document these auxiliary measurements.

5.3.1 Thermionic emission as electron source

In order to analyze the resolution of the MAC-E filter without the influence of the rf field, the electrons produced by thermionic emission

were used. The anion producing part was disconnected and a thin tungsten filament was placed into the center of the octopole (radially and axially with respect to the ring electrodes). The potential of the ring electrodes was set to 0 V with respect to the reference DC potential of the octopole rods.

The filament was heated by ohmic heating and the heating current was turned on and off with repetition frequency ≈ 100 Hz and duty ratio 0.5. We ensure by gating of the detector that the electrons are counted only in the phase with zero heating current. In this way the filament surface potential is well defined and can be biased to desired value without the influence of voltage drop due to the filament resistance.

The electrons emitted from the hot filament originate from the high-energy tail of the Fermi-Dirac distribution of electrons in the metal, which can be approximated by the Boltzmann distribution. The electron flux distribution is obtained by multiplying the Boltzmann velocity distribution with electron velocity component perpendicular to the metal surface. After integration over the angular coordinates this leads to the energy distribution of the emitted electrons

$$f(E_e) dE_e = (k_B T)^{-2} E_e \exp\left(-\frac{E_e}{k_B T}\right) dE_e, \quad (80)$$

where k_B is the Boltzmann constant and T is the filament temperature. The offset on energy scale of the measured spectrum is determined by the bias voltage applied to the filament and by the difference of work functions between the spectrometer electrodes and the filament. Several measurements were performed at different bias voltages with respect to the trap potential and the obtained integral and differential spectra are shown in figure 33. The differential spectra were analyzed by fitting a convolution of the theoretical spectrum (80) and a Gaussian function. The position μ , standard deviation σ , and temperature T were used as free parameters. We have determined that the work function of the filament is approximately 0.1 eV higher than the work function of the electrodes. The effective potential barrier is approximately 2 % higher than the applied electrode potential with respect to the octopole due to the filtering properties of the MAC-E filter in combination with the inhomogeneities of the electrostatic field, which is in agreement with our numerical calculations. The estimated temperature of the filament is $T = (1080 \pm 40)$ K.

The fitted standard deviation as a function of electron energy is shown in figure 34. The same analysis was also carried out on simulated data under equivalent conditions and the results are also shown

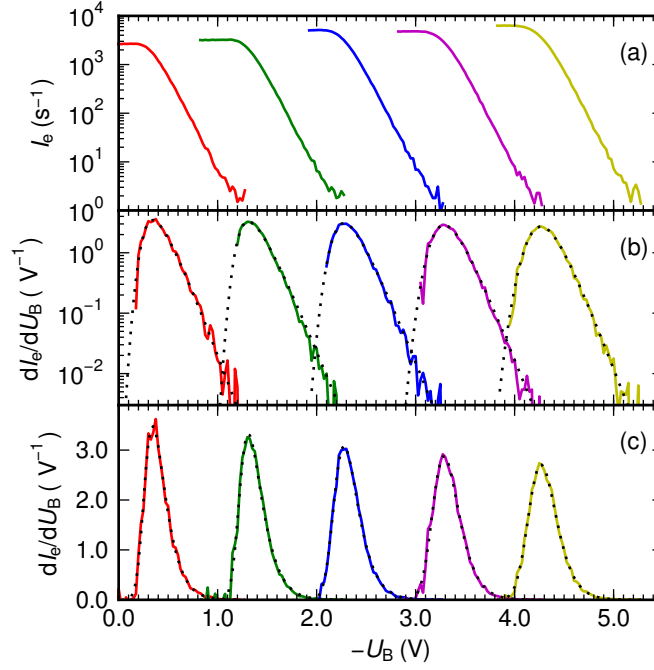


Figure 33: The measured spectra of electrons produced by thermionic emission from hot filament. Panel (a) — Integral recorded spectra. Panels (b), (c) — Differential spectra (normalized) obtained from the integral spectra in logarithmic and linear scales respectively. Cathode bias voltages -0.1 , -1.1 , -2.1 , -3.1 , and -4.1 V were used to provide electrons of 5 different energy distributions (full lines). Fits of the theoretical spectrum (80) convolved with a Gaussian function and offset by the bias voltage are indicated by the dotted lines.

therein. The figure demonstrates the broadening of the peaks at higher electron energies, which is also apparent in figure 33(c). This observation is in accordance with equation (77), since the MAC-E filter resolution is proportional to the energy. The broadening σ , which consists of a constant part σ_c and a proportional part $\sigma_p E_e$, can be expressed as $\sigma^2 = \sigma_c^2 + (\sigma_p E_e)^2$. The constant part is comparable to the expected variation of the work function on the filament surface (between 0.01 and 0.1 eV according to Darling et al. (1992); Rossi and Opat (1992)) and it is not relevant for our analysis. The proportional part determined by fitting of the experimental data is $\sigma_p = (2.0 \pm 0.1) \%$ and it is compatible with value determined from the simulation $\sigma_p = (1.6 \pm 0.1) \%$. The measured value is of the same magnitude as the

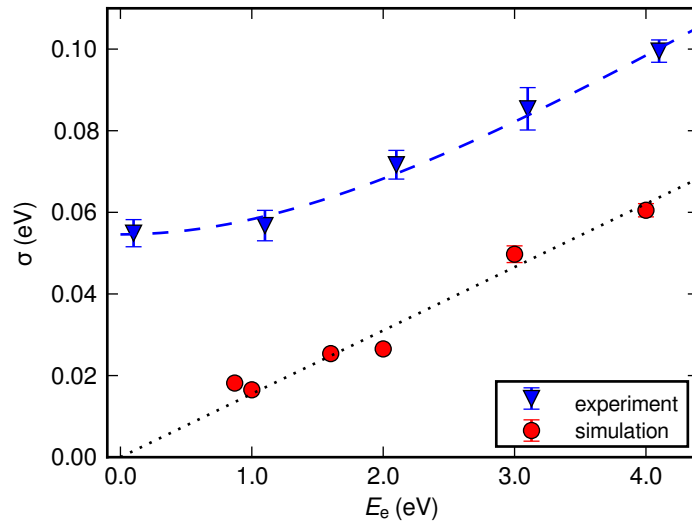


Figure 34: Resolution of the MAC-E filter as a function of electron energy. Triangles correspond to the resolution determined from the measurements with electrons from thermionic emission (figure 33). Circles represent the computer simulation of the spectra (Roučka, 2012). The instrument function is approximated with a Gaussian and its standard deviation σ is shown on the ordinate.

theoretical peak width $B_2/B_1 = 3.3\%$ (equation (77)), although it is not directly comparable, because the peak is not Gaussian and other effects such as potential inhomogeneity contribute to the experimental and simulated values.

The electrons from the thermionic emission can also be used to investigate the influence of the octopole rf field on the measured spectra. The distortion of the measured spectra for bias voltage -1.1 V and different rf amplitudes applied to the octopole is indicated in figure 35. This effect of the rf field on the electrons from the filament is not directly comparable to the effect on electrons from the trapped anions, because the potential of the filament is well defined by the applied bias in contrast to the potential at which the electron is detached from the anion. The actual position of the detaching anion in the rf field determines the potential (section 2.3.1). We deduce that the effects presented in figure 35 are caused by rf multipole field interacting with the electrons flying through the octopole after leaving the filament surface.

The influence of the magnetic field intensity inside the trap on the measured spectra was also investigated in the configuration with ther-

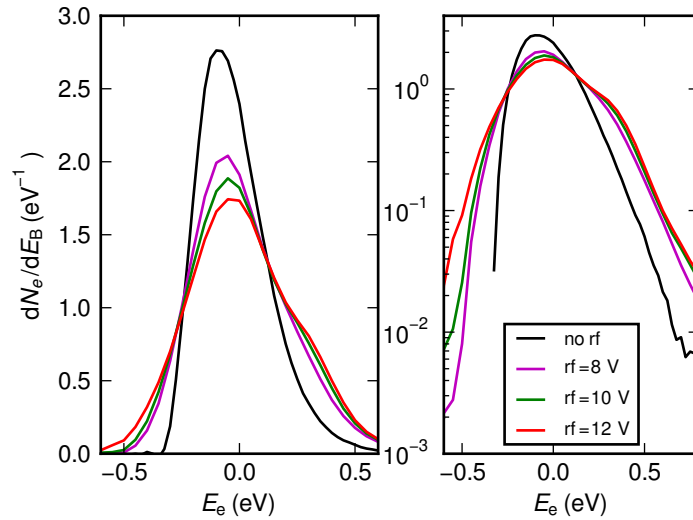


Figure 35: Influence of the rf field to the measured spectra of cathode emitted electrons. Spectrum measured with and without rf field present (cathode bias is -1.1 V, this corresponds to 0 eV energy on the abscissa).

mionic filament. The results for two different intensities are plotted in figure 36, although the interpretation of such measurements is not straightforward because the refocusing and bending coils magnetic intensities had to be also adjusted. Therefore the ES-MPT was operated at single spatial magnetic intensity configuration in all remaining experiments.

5.3.2 Anion photodetachment

For further tests with trapped O^- anions, the MCP detector was placed closer to the trap replacing the ES2 electrode in order to allow simultaneous detection of ions (focused by electrostatic fields) and electrons (focused by magnetic fields directly to the detector without adiabatic collimation). The experiment was operated in two distinct modes:

1. The ions were repeatedly injected into the trap, stored for a certain trapping time, then extracted to the detector and counted. In this mode the detector was gated in order to detect only the ions after the trap opening. A similar technique was previously used by Hlavenka et al. (2009) to measure absolute photodetachment cross sections of O^- and OH^- anions.

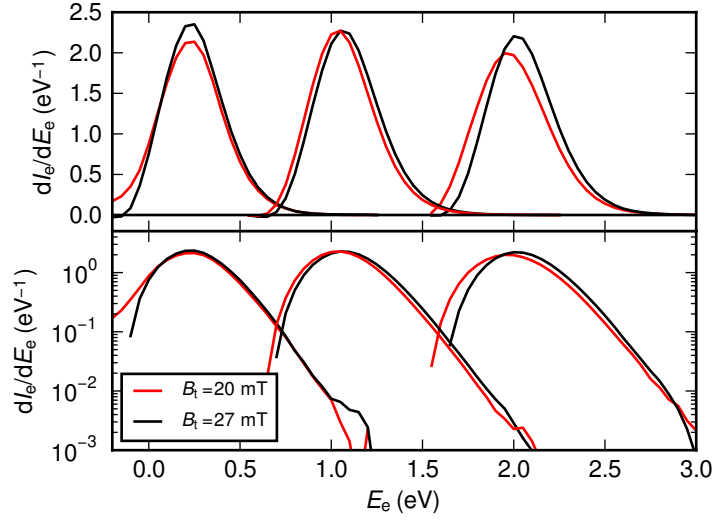
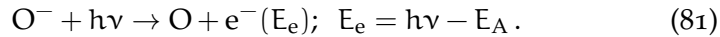


Figure 36: Influence of the magnetic field intensity inside the trap to the measured spectra of cathode emitted electrons.

2. A long fixed trapping time was used and the detector gate was open continuously between the ion injection and extraction. In this mode, the electrons produced in the trap were detected and their arrival times were recorded using a multichannel scaler.

In this configuration, in mode 1., we have verified that the presence of the magnetic field of the spectrometer does not influence the confinement time τ (the time constant of the ion loss from the trap) in figure 37. The confinement time in our experiment is limited by reactions with background gas and by eventual evaporation of anions due to the rf heating. For numerical simulations of the latter phenomena see Asvany and Schlemmer (2009).

Irradiating the trap with laser with photon energy $h\nu$ higher than the electron affinity E_A of the atomic oxygen causes photodetachment



The loss of the ions due to the photodetachment was observed in the mode 1. of our measurement. In the mode 2. we were able to detect the photodetached electrons under the same conditions. The results of these measurements with a pulsed laser beam with 660 nm wavelength are summarized in figure 38. The laser wavelengths and photon energies used in this work and corresponding energies of the photodetached electrons are summarized in table 3. The figure 38 clearly in-

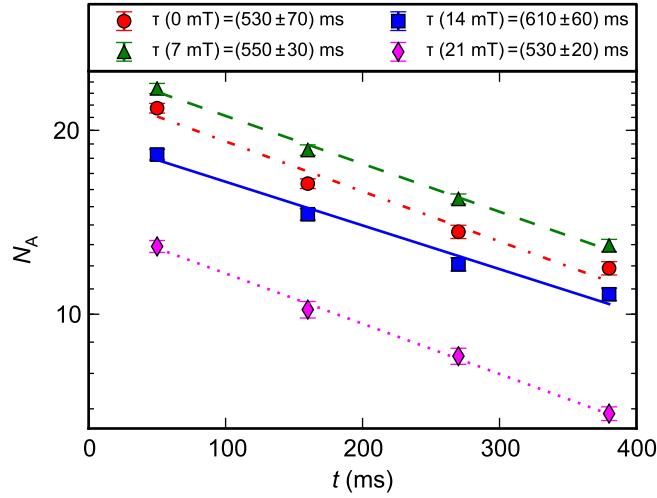


Figure 37: Measured number of O^- anions as a function of storage time t . The data shown as circles, triangles, diamonds and squares have been recorded using different magnetic field intensity inside the octopole trap. The statistical errors are smaller than the size of the symbols. Number of O^- is not normalized, various intensities at different magnetic field intensities are caused by the change of overall detection efficiency. The confinement time is independent on the magnetic field intensity.

indicates the increased rate of electron production related to the laser pulse. Order of magnitude smaller flux of electrons is observed even after the laser is switched off. This is caused by trapping of a fraction of the photodetached electrons in the ion trap as explained in section 5.2.1. These electrons reside in the trap until their velocity is sufficiently disturbed by the rf field and they leave the trap towards the detector or to the octopole rods.

In figure 38 we compare the measured total number of produced electrons (integral of the electron flux in time) and the expected number of electrons calculated from the decrease of the number of O^- anions as a function of storage time. The lines are in a remarkably good agreement after introducing normalization due to different overall detection efficiency for electrons and O^- anions.

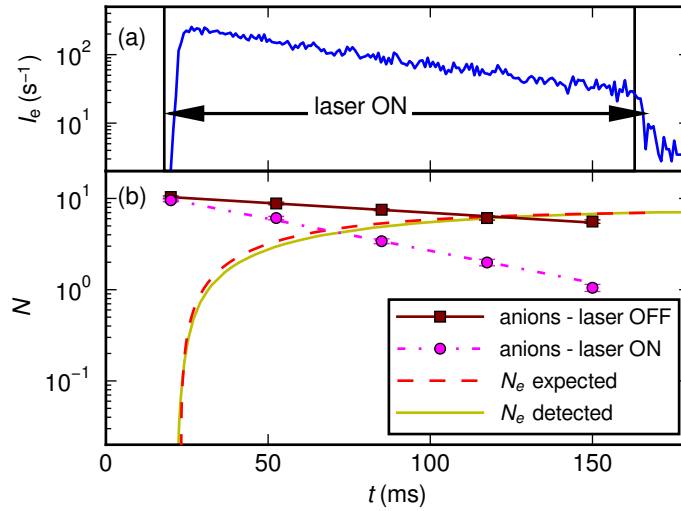


Figure 38: Number of detected electrons and O^- anions as a function of storage time (t) during a pulsed laser photodetachment experiment (using red laser, see table 3). Panel (a) — the measured electron production rate with the laser pulse ON. The duration of the laser pulse is indicated. Panel (b) — squares and circles indicate the number of O^- with the laser pulse OFF and ON respectively. Exponential fits of the ions counts are also indicated. The dashed line shows the expected number of produced electrons calculated from the fits. The expected number is in good agreement with the measured number (solid line) obtained by integrating the electron production rate corrected for the differences in electron and ion detection efficiencies.

5.3.3 Spectra of the photodetached electrons

The spectra of photodetached electrons were measured in the full ES-MPT setup (figure 30). The integral spectra are obtained by measuring the electron count rate on the detector as a function of the retarding potential U_B . The laser is switched on after filling the trap with approximately 20 ms time delay, during which the ions are cooled by collisions with the helium buffer gas. The spectra of photodetached electrons were measured with four lasers, the wavelengths and corresponding electron energies are summarized in table 3. The differential spectra obtained with the Savitzky-Golay smoothing filter are plotted in figure 39. The standard deviation of the measured data is indicated by the error bars.

A similar experiment was carried out also with a mixture of H_2 and He in the trap. In this case, only the violet (405 nm) laser was used. The

Table 3: Overview of the laser wavelengths and corresponding photon energies used in the photodetachment experiments. The right column shows the energy E_e of electrons produced by photodetachment of O^- . The electron affinity of O is $E_A = 1.4610$ eV (Appendix B).

COLOR	λ (nm)	$h\nu$ (eV)	E_e (eV)
red	660	1.88	0.42
green	532	2.33	0.87
blue	445	2.79	1.33
violet	405	3.06	1.60

number of Langevin collisions between O^- and H_2 before switching on the laser was varied by changing the H_2 concentration in the trap and the delay of the laser pulse after trap filling. The obtained spectra are shown in figure 40. Depending on the average number of Langevin collisions between O^- and H_2 before switching on the laser, we can observe two peaks with varying intensities in the spectra. These peaks can be attributed to the electrons produced by photodetachment of O^- and OH^- , the anion product of the reaction (70). The peak positions are in good agreement with the electron energies expected from the O and OH electron affinities (Appendix B).

5.4 EXPERIMENTAL RESULTS

Although the ES-MPT apparatus is primarily designed to study the energy distribution of the electrons produced from the associative detachment reaction, it is also in principle usable to measure the reaction rate coefficients. The reaction rates of associative detachment were studied by adding a mixture of helium buffer gas with the reactant into the scattering cell. The typical ratio of the reactant to the buffer gas number densities was approximately the same for all reactions $[H_2]/[He]$, $[D_2]/[He]$, and $[CO]/[He] \approx 1/3$.

5.4.1 Reaction rate coefficient

The electron production rate dN_e/dt in the presence of a reactant gas is proportional to the number of ions in the trap and to the number

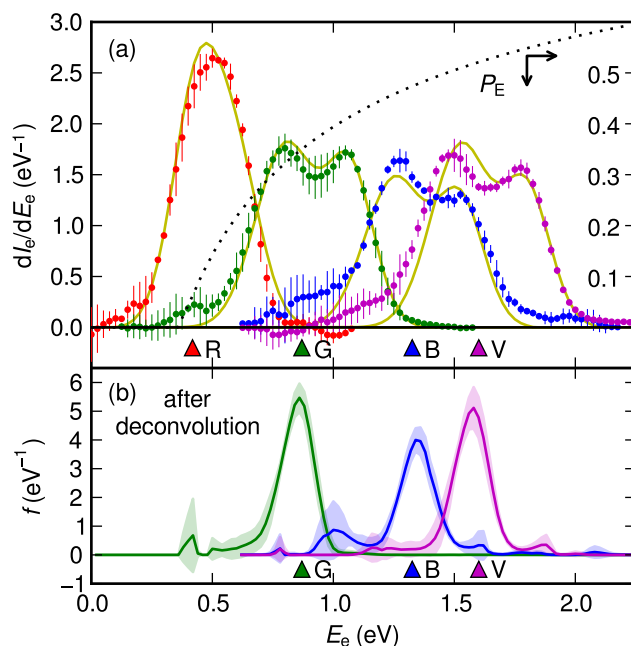


Figure 39: Measured spectra of electrons photodetached from O^- anions. Photon wavelengths used are 660 nm (R), 532 nm (G), 445 nm (B) and 405 nm (V) (table 3). Panel (a) — points correspond to measured data with wavelengths red, green, blue, and violet respectively (from left). Triangles indicate the expected electron energies according to table 3. The right axis corresponds to the extraction probability $P_E(U_T)$ (dotted line), where the trapping potential U_T is determined from the fit. The smooth full lines represents the convolution fitted on the theoretical spectrum using the instrument function. Panel (b) – the spectra obtained from the measured data after deconvolution with the instrument function.

density of the reactant. In the case of trapping N_O of O^- ions in the trap with reactant H_2 (concentration $[H_2]$), we derive

$$I_e = s \frac{dN_e}{dt} = sk_1[H_2]N_O, \quad (82)$$

where I_e is the number of detected electrons per unit time (electron flux) and s the detection efficiency of our instrument for electrons. The detection efficiency is constant for electrons at our electron energy scale, therefore we are allowed to investigate the disappearance of O^- after filling the trap by recording the electron flux in time using the multichannel scaler. Examples of the measured I_e for different H_2 number density are shown in figure 41. In this measurement the

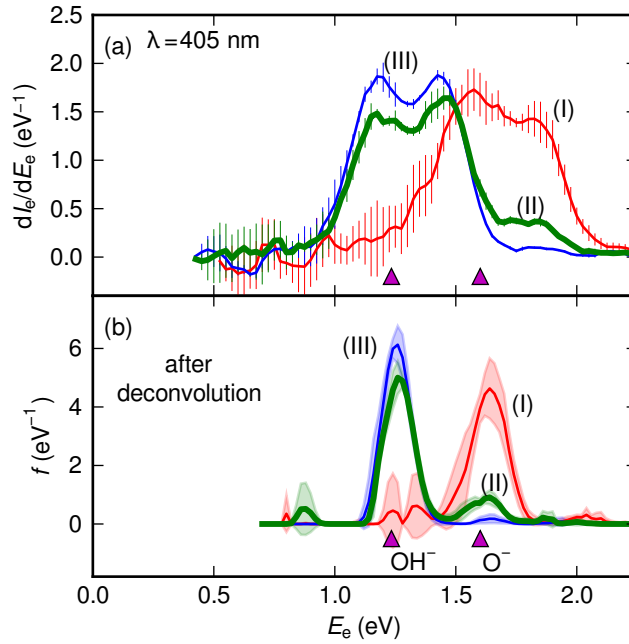


Figure 40: Panel (a) – measured spectra of the photodetached electrons from O^- and OH^- using the violet laser. The trapped O^- ions interact with H_2 in the trap. The average number of Langevin collision of O^- with H_2 before the laser is switched ON is 0, 2, and 7 for the curves (I), (II), and (III) respectively. The peaks in the spectrum, obtained from the measured data after deconvolution, can be attributed to the electrons produced from OH^- and O^- (panel (b)). The expected positions of the peaks are indicated by the triangles.

retarding potential U_B is set to zero – all produced electrons are contributing to I_e .

When the reactant gas is not present in the trap, the number of ions in the trap as a function of time can be probed using short laser pulses (≈ 10 ms). The number of observed photodetached electrons is proportional to the number of ions in the trap (figure 42).

The number density of the reactant is estimated from the geometrical configuration, pumping speed and ion gauge pressure measurement. Our estimates account for the differences in the ion gauge sensitivities and vacuum conductivities between different gases. The calculated total reaction rate coefficients $k = k_1 + k_2$ for reactions of $\text{O}^- + \text{H}_2$ and $\text{O}^- + \text{D}_2$ (reaction (62) and its isotopic variant) are compared with the previous measurement done at the 22-pt and measurements done by McFarland et al. (1973) in table 4. Despite the good

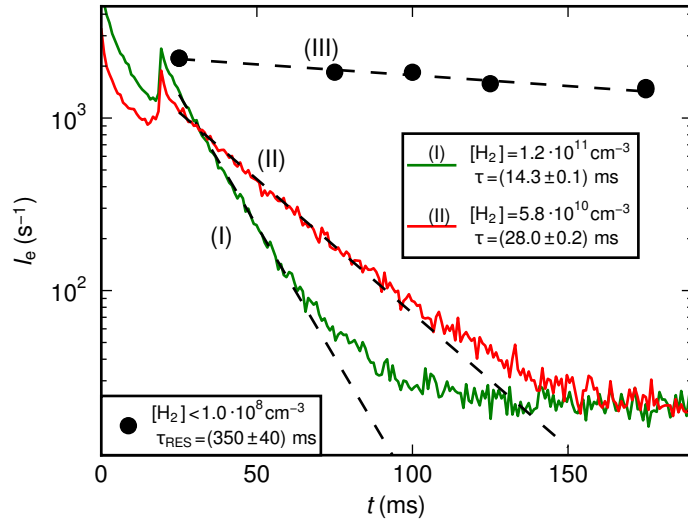


Figure 41: Measured electron production rate in reaction (69) as a function of trapping time measured at two H_2 number densities (full lines (I) and (II)). The trap is filled with O^- at $t = 0$ ms. At $t = 20$ ms, the axial trapping barrier is lowered to allow the low energy electrons to escape. The circles indicate a data proportional to the number of trapped ions without added H_2 . The number of ions is probed by illuminating the ions with short laser pulses and detecting the photodetached electrons (also see figure 42). Dashed lines correspond to exponential decay fits in form $\exp(-t/\tau)$, obtained τ at given $[\text{H}_2]$ are indicated (τ_{RES} corresponds to confinement time without added reactant).

agreement with the results of McFarland et al. (1973), we estimate that the error of the calculated number density could be up to a factor of 2 caused by the simplifications in the geometric model of the instrument and because of the limited accuracy of the ionization pressure gauge. However, the geometric factors cancel if we calculate the ratio of the isotopic variants of the reaction coefficients $k(\text{H}_2)/k(\text{D}_2) = 1.7 \pm 0.1$ (the same for ES-MPT and 22-pt section 4.3), where only the statistical error is given. This value is slightly higher than the isotopic effect observed by McFarland et al. (1973), $k(\text{H}_2)/k(\text{D}_2) = 1.4$.

5.4.2 Energy distribution of detached electrons

The technique of acquiring the energy distribution of electrons from the associative detachment reaction is the same as for the photodetached electrons. The difference is that the electrons are produced con-

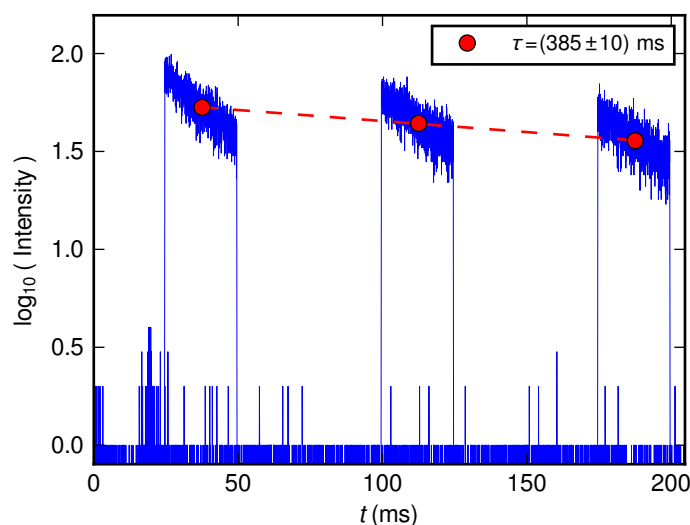


Figure 42: Indirect method of probing number of anions in the trap at different storage times (t). Electrons produced using short laser (≈ 10 ms) pulses to induce photodetachment of trapped O^- anions are counted using MCS. Sum of electrons produced at one particular time is proportional to the number of anions in the trap at that time.

tinuously. The electrons are selected by gating of the detector, so that only the electrons produced from cold O^- (thermalized by collisions with He buffer gas) are accounted.

Figure 43 shows the measured electron energy distributions for the associative detachment reactions of O^- with H_2 , D_2 , and CO . The energy distributions have been investigated up to the maximum energy allowed by the reaction exothermicity, which was given in section 5.1. The differential spectra were obtained by differentiating and smoothing the integral spectra using the Savitzky-Golay filter with the same parameters as the photodetachment spectra in figures 39 and 40. The differential spectra were deconvolved with the Gaussian kernel $\mathcal{N}(0, \sigma_3)$ using the Lucy Richardson algorithm (Lucy, 1974; Richardson, 1972) with a constraint on the positive value of the data and then divided by the extraction probability P_E (equation (78)). The data measured by Esaulov et al. (1990) are used as a reference for the normalization of our data with H_2 reactant. The same normalization factor was used afterwards for the data measured with D_2 and CO reactants, assuming a similar behavior in the inaccessible low-energy part of the spectrum. For the AD with H_2 , there is a good agreement between our results and the spectra obtained by Esaulov et al. (1990) in the over-

Table 4: Total reaction rate coefficient estimated from temporal evolutions of electron production at 300 K (figure 41) compared with previous measurements.

REACTION	k (ES-MPT) ($10^{-10} \text{ cm}^3 \text{ s}^{-1}$)	k (22-pt) ($10^{-10} \text{ cm}^3 \text{ s}^{-1}$)	k (Drift tube) ($10^{-10} \text{ cm}^3 \text{ s}^{-1}$)
$\text{O}^- + \text{H}_2$	5.4 ± 0.2	10.2 ± 0.6	6.4
$\text{O}^- + \text{D}_2$	3.2 ± 0.1	5.9 ± 0.2	4.6
ratio	1.7	1.7	1.4

Note: For reaction rate coefficient measurement on the 22-pt see section 4.3, for drift tube measurements see McFarland et al. (1973).

lapping region, despite the fact that his measurement was carried out at 1 eV collision energy. The measured spectra of electrons from the three studied reactions show similar features – we can conclude that the excess energy of the reactions is stored mainly in the internal excitation of the produced molecule. In figure 43, one can observe that there is no significant structure in the electron spectrum at energies above approximately 1.5 eV.

5.5 DISCUSSION

We outlined the possibilities of the ES-MPT apparatus together with first experimental results. Despite problems encountered, the instrument has sufficient resolution to obtain general characteristics of the energy distribution of electrons produced in AD. In the following sections we are going to discuss plausible improvements of the ES-MPT and several consequences for AD of O^- that have been discovered during our work on the apparatus.

5.5.1 Improvements of the ES-MPT apparatus

Our measurements with the electrons produced by thermionic emission (figure 33 and 34) demonstrate that the properties of the spectrometer itself are in accordance with the design. The measurements with electrons produced by thermionic emission and by photodetachment with applied rf trapping field indicate that the rf field influences the electrons and causes splitting of initially monoenergetic electron energy distribution (figure 35 and 39). According to our knowledge,

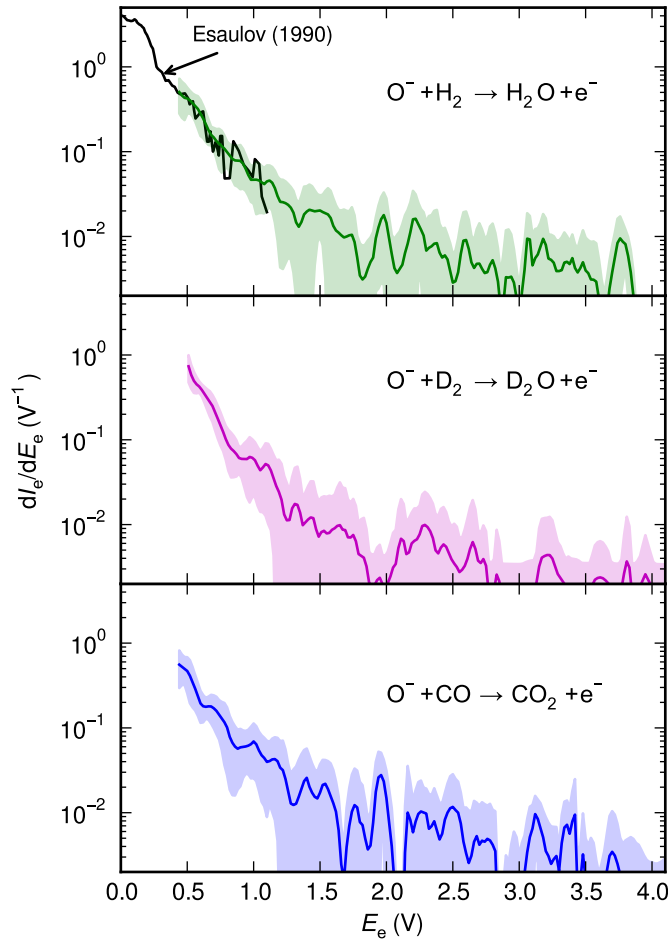


Figure 43: Measured electron energy spectra in the reactions of $\text{O}^- + \text{H}_2$, D_2 and CO (solid lines in panels (a), (b), and (c) respectively). The data of Esaulov et al. (1990) are shown for comparison and are used to normalize the spectra. The standard deviation of multiple measurements is indicated in the graph. At electron energies above 1.5 eV, the signal intensity is below the noise level and the results should be interpreted as an upper bound of the actual probability.

supported by computer model of Roučka (2012), such effects are not expected in the rf field of an ideal multipole. In the non-ideal conditions, where rf field in the trap is not symmetric (e. g. due to misalignment of the rods), the resulting spectra are possibly shifted/splitted depending on the location of origin of the electrons.

Since further decrease of the amplitude V_0 is not feasible in our setup as has been discussed in section 5.2.2, the obvious solution

would be to use a higher order multipole. The field decreases much faster towards the axis thus eliminating the variances in V_0 better.

The spectrometer threshold at low energies can in principle be improved by lowering the O^- energy, i. e., by cooling the trap. If the O^- anions have lower temperature, their kinetic energy is also lowered, thus a smaller axial barrier on ring electrodes would be needed to confine them, effectively improving the extraction probability P_E .

5.5.2 *Electrons produced in AD*

The spectra of electrons produced from the AD of O^- with H_2 , D_2 , and CO were measured at 300 K. In case of the reaction with H_2 , our results agree with the results of Esaulov et al. (1990), providing a supporting evidence in favor of Esaulov et al. against the results of Mauer and Schulz (1973). To our knowledge, the spectra for the reaction with D_2 and CO were not measured in the corresponding energy range up to now.

Our results indicate that for the studied AD reactions, the excess energy is stored mainly in the internal excitation of the molecule. There are two mechanisms responsible for this result. Firstly, a high rotational excitation is expected due to simple kinematic constraints – a collision system with nonzero impact parameter has nonzero angular momentum and this angular momentum is stored mainly in the molecular rotation because of the low mass of the ejected electron. Higher rotational excitation is statistically favored (Smith and Leone, 1983; Živanov et al., 2003) up to a certain J_m , which is limited by the energy conservation and by the corresponding centrifugal barrier. Secondly, the vibrational product distribution depends on the coupling between the bound and continuum states of the detaching electron. If this coupling is strong and the electron detaches early during the interaction at higher internuclear separation, the product will have high vibrational excitation according to the Franck-Condon principle (Smith and Leone, 1983; Živanov et al., 2003; Lee and Farrar, 1999).

FINAL REMARKS

In this work we presented several experimental techniques useful for anion–molecule reaction investigation. Apparatuses [AB 22-pt](#) and [ES-MPT](#) were described and supporting measurements have been shown to demonstrate their capabilities. Several new experimental results have been obtained and are going to be discussed together with the future planned improvements of the two instruments in this chapter.

ATOMIC BEAM – 22-POLE TRAP

The description of the [AB 22-pt](#) apparatus can be found in section [4.1](#). The apparatus has been used to investigate the associative detachment reaction $\text{H}^- + \text{H} \rightarrow \text{H}_2 + \text{e}^-$ (section [4.2](#)) and $\text{O}^- + \text{H}_2 \rightarrow \text{H}_2\text{O} + \text{e}^-$ (together with OH^- channel, section [4.3](#)).

In case of H^- , our measurements of reaction rate coefficient are in good agreement with previous results of Kreckel et al. ([2010](#)) in the overlapping temperature region and also with theory of Čížek et al. ([1998](#)). Our measurements in the range 10 to 40 K are unique, though do not show any unexpected behaviour. The greatest source of uncertainty is the 40 % estimated error of the reaction rate coefficient used to calibrate the H beam number density. These results have been published (Gerlich et al., [2012](#)), see Attached articles, [Article I](#).

On the other hand, results of O^- associative detachment reaction rate coefficient have smaller overall uncertainty (expected below 20 %), because of higher accuracy of number density determination of directly leaked molecular gas in our setup. The results obtained at 300 K are directly comparable with previous measurements of McFarland et al. ([1973](#)) and are slightly higher. The measurements down to 10 K are unique and are showing a similar unexpected maximum at temperature close to 50 K as has been recently observed by Otto et al. ([2008](#)) for the $\text{NH}_2^- + \text{H}_2$ system. These results are being prepared for submission.

ELECTRON SPECTROMETER – MULTIPOLE TRAP

Whole chapter 5 is devoted to the ES-MPT. The ion part of the setup is a well known guided ion beam configuration. However, the spectrometer part of the instrument has been built from the very beginning, thus we made several calibration measurements, which were then confronted with the design to properly and undoubtedly characterise the ES-MPT.

Electrons produced from thermionic emission (section 5.3.1) and photodetachment (section 5.3.3) have been used as an energy calibration standard. The spectrometer resolution is close to the projected, including the problems associated with low energy electrons due to axial barriers used for anion trapping. The ES-MPT is ideally suited for associative detachment reaction studies of cold trapped anions and in contrast with previous measurements even allows measurements with beams (e. g. atomic H), not only molecular gas as a neutral reactant in the reaction.

The measurements of energy distribution of electrons produced in associative detachment reaction $\text{O}^- + \text{H}_2 \rightarrow \text{H}_2\text{O} + \text{e}^-$ are in agreement with previous measurement of Esaulov et al. (1990) in the overlapping region. Even though energy in the Esaulov's experiment was close to 1 eV (our measurements are thermal). The electron energy distributions for reactions $\text{O}^- + \text{D}_2 \rightarrow \text{D}_2\text{O} + \text{e}^-$ and $\text{O}^- + \text{CO} \rightarrow \text{CO}_2 + \text{e}^-$ measured up to 4 eV are unique and have not been acquired before according to our knowledge ($\text{O}^- + \text{CO}$ has been studied by Mauer and Schulz (1973) up to 0.6 eV). There is no significant structure in the electron spectrum for any of the AD reactions studied at energies above 1.5 eV. Results presented in chapter 5 served as a basis for the article submitted on 28. May 2013 (Attached articles, Article II).

Future improvements of the ES-MPT include active cooling of the anions below 300 K, in order to decrease the anion axial trapping barrier, effectively improving the spectrometer response at lower electron energies. The spectrometer would also benefit of use of higher order multipole because of faster rf field decrease towards the axis.

Part I

APPENDIX

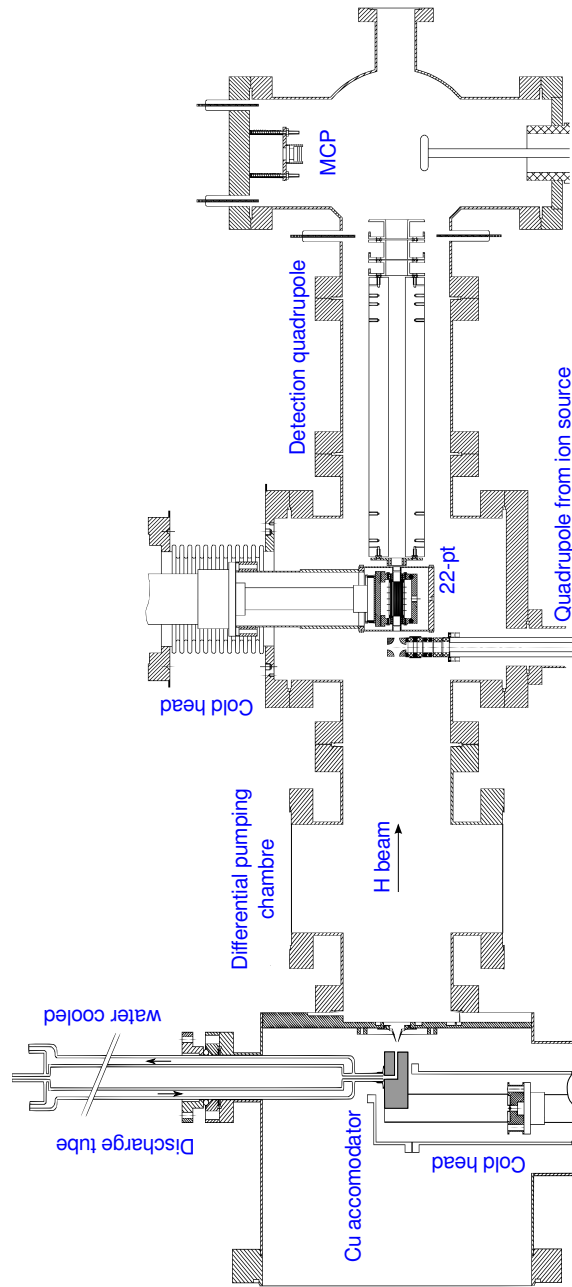


Figure 44: AB-22-pt apparatus CAD drawing (in scale). From left: H atom source, differential pumping chamber, 22-pole trap, MCP detector.

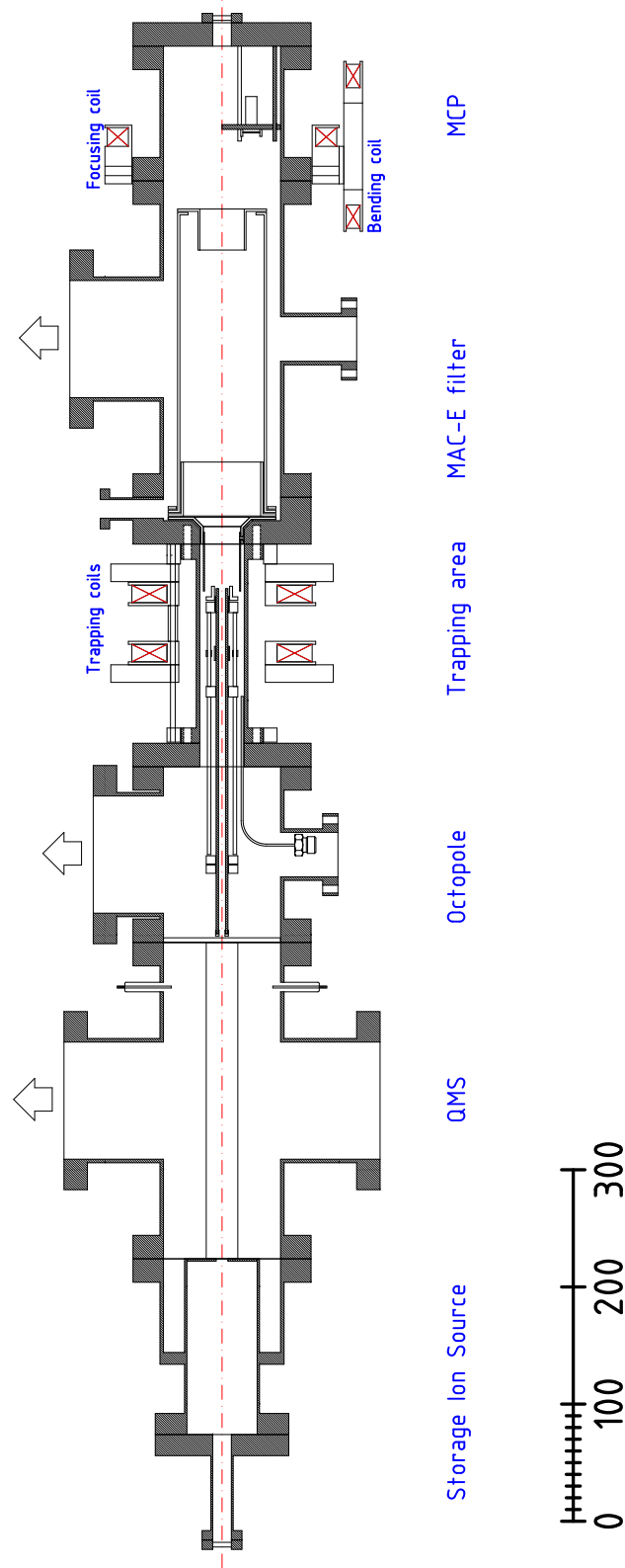


Figure 45: ES-MPT apparatus CAD drawing (in scale). Red crosses represent the coil windings. Arrows at the top represent turbomolecular pumping.

B

ELECTRON AFFINITIES

ATOMIC ANIONS

Table 5: Electron affinities of the elements in eV.

	I.A	II.A		III.A	IV.A	V.A	VI.A	VII.A
1	H -0.76							
2	Li -0.62	Be		B -0.28	C -1.27	N	O -1.43	F -3.41
3	Na -0.55	Mg		Al -0.46	Si -1.39	P -0.75	S -2.08	Cl -3.62
4	K -0.5	Ca	...	Ga -0.31	Ge -1.25	As -0.80	Se -2.02	Br -3.37
5	Rb -0.49	Sr	...	In -0.31	Sn -1.26	Sb -1.05	Te -1.97	I -3.06
6	Cs -0.47	Ba	...	Tl -0.31	Pb -1.14	Bi -1.14	Po -1.87	At -2.8

Compiled from
NIST Chemistry
WebBook. <http://webbook.nist.gov/>

SELECTED MOLECULAR ANIONS

Table 6: Electron affinities of selected molecules in eV.

H/D	H ₂ O	C+H	C+O	N	N	O
OH -1.83	H ₂ O -1.20	CH -1.24	CO -1.33	N ₂ O -0.22	NO -0.02	O ₂ -0.45
OD -1.83	H ₂ O · H -1.53	C ₅ H -2.42	C ₂ O -2.31	H ₂ N -0.77	NO ₂ -2.27	O ₃ -2.10

SCRIPTS FOR EFFECTIVE POTENTIAL V^*

Listing 1: Script for evaluation of quadrupole transmission properties

```
#!/usr/bin/python2.7
import numpy as np, pylab as plt

#Quadrupole parameters
f0 = 1.723e6           #in Hz
r0 = 0.004           #in m
V0max = 80.0         #in V
U0max = 0             #in V; 0 for "auto"

masses = [1,2,13,16,17,18] #masses to be plotted
#-----

a_ideal = 0.237
q_ideal = 0.706
q = 1.602177e-19
Omega, amu = 2*3.14159265 * f0, 1.67262158e-27
x_vec = np.arange(0.0, V0max, 0.1)
ax = plt.subplot(111)

for m in masses:
    y_vec = np.minimum(q*x_vec**2/(m*amu*Omega**2*r0**2),
                       m*amu*Omega**2*r0**2/(8.0*q) - x_vec/2.0)
    U0max = max(max(y_vec), U0max)
    ax.plot(x_vec, y_vec)
    ax.text(x_vec[y_vec.argmax()], max(y_vec)+0.06, '%d' % m,
            horizontalalignment='center', verticalalignment='bottom')

ax.set_ylim([0.0, 1.08*U0max])
ax.set_xlim([0.0, V0max])
ax.set_xlabel(r"\it{V_0}$ (V)")
ax.set_ylabel(r"\it{U_0}$ (V)")
plt.show()
```

Listing 2: Script for effective potential evaluation

```
#!/usr/bin/python2.7
import numpy as np, pylab as plt

#Multipole parameters
f0 = 4.4e6           #in Hz
V0 = 10             #in V
q = 1.602177e-19
r0 = 0.003          #in m
n = 4
Omega = 2*3.14159 * f0
mass = 16           #in amu

def epsilon(m):
    return 1.0/(2.0 * n**2) * m*1.67262158e-27 * Omega**2 * r0**2

def Ve(r, eps):
    return 1.0/(8.0 * eps) * q**2 * V0**2 * (r/r0)**(2*n-2)

def eta(r, eps):
    return (n - 1.0)/(eps* n ) * q * V0 * (r/r0)**(n-2)

#-----
x = np.arange(0, r0, 0.00001)
fig = plt.figure()
ax = fig.add_subplot(111)
ax.plot(x*1000, Ve(x, epsilon(mass))/q*1000, ls = "--",
        label = '$\it{V*}$ ($\it{m}$=%d)' % mass)

ax.set_ylim([0, 100.])
ax.set_xlim([0.0, r0])
ax.set_xlabel(r'$\it{r}$ (mm)')
ax.set_ylabel(r'$\it{V*}$ (meV)')
ax2 = ax.twinx()
ax2.plot(x*1000, eta(x, epsilon(mass)), ls = "-.", c='r',
        label = r'$\it{\eta}$')

plt.axvline(x=0.8*r0*1000, c='r', label = None)
ax2.set_ylim([0, eta(r0, epsilon(mass))])
ax2.set_ylabel(r'$\it{\eta}$')
ax.text(0.02, 0.7, r'$\it{f_0}$ = %.1f MHz' % (float(f0)*1.0e-6),
        transform = ax.transAxes)
ax.text(0.02, 0.6, r'$\it{V_0}$ = %.1f V' % V0, transform = ax.
        transAxes)
ax.text(0.02, 0.5, r'$\it{n}$ = %d' % n, transform = ax.transAxes)
ax.text(0.81, 0.1, r'$\it{r} = 0.8 r_0$', color='r', transform =
        ax.transAxes)
ax.legend(loc=2), ax2.legend(loc=9)
plt.show()
```

BIBLIOGRAPHY

- Abouaf, R., R. Paineau, and F. Fiquet-Fayard (1976). "Dissociative attachment in NO_2 and CO_2 ." In: *Journal of Physics B: Atomic and Molecular Physics* 9.2, p. 303. DOI: [10.1088/0022-3700/9/2/017](https://doi.org/10.1088/0022-3700/9/2/017) (cit. on p. 48).
- Agúndez, M., J. Cernicharo, M. Guélin, C. Kahane, E. Roueff, J. Kłos, et al. (2010). "Astronomical identification of CN^- , the smallest observed molecular anion." In: *Astronomy & Astrophysics* 517, p. L2. DOI: [10.1051/0004-6361/201015186](https://doi.org/10.1051/0004-6361/201015186) (cit. on pp. 1, 31).
- Asvany, O. (2004). "Experiments with Ions and Clusters in a variable temperature 22-pole ion trap." PhD thesis. TU Chemnitz (cit. on p. 40).
- Asvany, O. and S. Schlemmer (2009). "Numerical simulations of kinetic ion temperature in a cryogenic linear multipole trap." In: *International Journal of Mass Spectrometry* 279.2-3, pp. 147–155. DOI: [10.1016/j.ijms.2008.10.022](https://doi.org/10.1016/j.ijms.2008.10.022) (cit. on pp. 31, 59).
- Ayouz, M., O. Dulieu, R. Guerout, J. Robert, and V. Kokoouline (2010). "Potential energy and dipole moment surfaces of H_3^- molecule." In: *The Journal of Chemical Physics* 132.19, DOI: [10.1063/1.3424847](https://doi.org/10.1063/1.3424847) (cit. on p. 44).
- Ayouz, M., R. Lopes, M. Raoult, O. Dulieu, and V. Kokoouline (2011). "Formation of H_3 by radiative association of H_2 and H^- in the interstellar medium." In: *Physical Review A* 83.5, p. 052712. DOI: [10.1103/PhysRevA.83.052712](https://doi.org/10.1103/PhysRevA.83.052712) (cit. on p. 45).
- Beamson, G., H. Q. Porter, and D. W. Turner (1980). "The collimating and magnifying properties of a superconducting field photoelectron spectrometer." In: *Journal of Physics E: Scientific Instruments* 13.1, p. 64. DOI: [doi:10.1088/0022-3735/13/1/018](https://doi.org/10.1088/0022-3735/13/1/018) (cit. on p. 49).
- Beatty, E. C. and P. L. Patterson (1965). "Mobilities and Reaction Rates of Ions in Helium." In: *Physical Review* 137.2A, A346–A357. DOI: [10.1103/PhysRev.137.A346](https://doi.org/10.1103/PhysRev.137.A346) (cit. on p. 28).
- Beu, S. C., C. L. Hendrickson, and A. G. Marshall (2011). "Excitation of Radial Ion Motion in an rf-Only Multipole Ion Guide Immersed in a Strong Magnetic Field Gradient." en. In: *Journal of The American Society for Mass Spectrometry* 22.3, pp. 591–601. DOI: [10.1007/s13361-010-0057-9](https://doi.org/10.1007/s13361-010-0057-9) (cit. on p. 49).
- Bohringer, H., W. Glebe, and F. Arnold (1983). "Temperature dependence of the mobility and association rate coefficient of He^+ ions

- in He from 30-350 K." en. In: *Journal of Physics B: Atomic and Molecular Physics* 16.14, p. 2619. DOI: [10.1088/0022-3700/16/14/022](https://doi.org/10.1088/0022-3700/16/14/022) (cit. on pp. [27](#), [28](#)).
- Borodi, G., A. Luca, and D. Gerlich (2009). "Reactions of CO_2^+ with H, H_2 and deuterated analogues." In: *International Journal of Mass Spectrometry* 280.1-3, pp. 218–225. DOI: [10.1016/j.ijms.2008.09.004](https://doi.org/10.1016/j.ijms.2008.09.004) (cit. on pp. [22](#), [25](#), [31](#), [35](#)).
- Bruhns, H., H. Kreckel, K. A. Miller, X. Urbain, and D. W. Savin (2010). "Absolute energy-resolved measurements of the $\text{H}^- + \text{H} \rightarrow \text{H}_2 + \text{e}^-$ associative detachment reaction using a merged-beam apparatus." In: *Physical Review A: General Physics* 82.4, p. 042708. DOI: [10.1103/PhysRevA.82.042708](https://doi.org/10.1103/PhysRevA.82.042708) (cit. on pp. [38](#), [39](#)).
- Brünken, S., H. Gupta, C. A. Gottlieb, M. C. McCarthy, and P. Thaddeus (2007). "Detection of the Carbon Chain Negative Ion C_8H^- in TMC-1." en. In: *The Astrophysical Journal Letters* 664.1, p. L43. DOI: [10.1086/520703](https://doi.org/10.1086/520703) (cit. on p. [33](#)).
- Cernicharo, J., M. Guélin, M. Agúndez, K. Kawaguchi, M. McCarthy, and P. Thaddeus (2007). "Astronomical detection of C_4H^- , the second interstellar anion." In: *Astronomy & Astrophysics* 467, pp. L37–L40. DOI: [10.1051/0004-6361:20077415](https://doi.org/10.1051/0004-6361:20077415) (cit. on p. [33](#)).
- Chen, F. F. (1974). *Introduction to Plasma Physics*. New York: Plenum Press (cit. on p. [3](#)).
- Chun-Sing, O. and H. A. Schuessler (1981). "Confinement of ions created externally in a quadrupole ion trap operated in the combined Penning and radio-frequency mode." In: *Journal of Applied Physics* 52.4, pp. 2601–2607. DOI: [10.1063/1.329069](https://doi.org/10.1063/1.329069) (cit. on p. [52](#)).
- Čížek, M., J. Horáček, and W. Domcke (1998). "Nuclear dynamics of the H collision complex beyond the local approximation: associative detachment and dissociative attachment to rotationally and vibrationally excited molecules." In: *Journal of Physics B: Atomic, Molecular and Optical Physics* 31, pp. 2571–2583. DOI: [10.1088/0953-4075/31/11/018](https://doi.org/10.1088/0953-4075/31/11/018) (cit. on pp. [38](#), [47](#), [71](#)).
- Claydon, C. R., G. A. Segal, and H. S. Taylor (1971). "Theoretical Interpretation of the Optical and Electron Scattering Spectra of H_2O ." In: *The Journal of Chemical Physics* 54.9, pp. 3799–3816. DOI: [10.1063/1.1675431](https://doi.org/10.1063/1.1675431) (cit. on pp. [47](#), [48](#)).
- Daly, N. R. (1960). "Scintillation Type Mass Spectrometer Ion Detector." In: *Review of Scientific Instruments* 31.3, pp. 264–267. DOI: [10.1063/1.1716953](https://doi.org/10.1063/1.1716953) (cit. on p. [20](#)).
- Darling, T. W., F. Rossi, G. I. Opat, and G. F. Moorhead (1992). "The fall of charged particles under gravity: A study of experimental

- problems." In: *Reviews of Modern Physics* 64.1, pp. 237–257. DOI: [10.1103/RevModPhys.64.237](https://doi.org/10.1103/RevModPhys.64.237) (cit. on p. 56).
- Dehmelt, H. G. and F. L. Walls (1968). "'Bolometric" Technique for the rf Spectroscopy of Stored Ions." In: *Physical Review Letters* 21 (3), pp. 127–131. DOI: [10.1103/PhysRevLett.21.127](https://doi.org/10.1103/PhysRevLett.21.127) (cit. on p. 13).
- Dodin, I. Y. and N. J. Fisch (2005). "Approximate integrals of radio-frequency-driven particle motion in a magnetic field." In: *Journal of Plasma Physics* 71.03, pp. 289–300. DOI: [10.1017/S0022377804003174](https://doi.org/10.1017/S0022377804003174) (cit. on p. 52).
- Dodin, I. and N. Fisch (2006). "Nonadiabatic ponderomotive potentials." In: *Physics Letters A* 349.5, pp. 356–369. DOI: [10.1016/j.physleta.2005.09.049](https://doi.org/10.1016/j.physleta.2005.09.049) (cit. on p. 52).
- Eichelberger, B., T. Snow, and V. Bierbaum (2003). "Collision rate constants for polarizable ions." In: *Journal of The American Society for Mass Spectrometry* 14.5, pp. 501–505. DOI: [10.1016/S1044-0305\(03\)00134-X](https://doi.org/10.1016/S1044-0305(03)00134-X) (cit. on p. 44).
- Esaulov, V. A., R. L. Champion, J. P. Grouard, R. I. Hall, J. L. Montmagnon, and F. Penent (1990). "Reactive scattering and electron detachment in O^- collisions with H_2 . Nascent product energy distributions." In: *Journal of Chemical Physics* 92.4, pp. 2305–2309. DOI: [10.1063/1.457971](https://doi.org/10.1063/1.457971) (cit. on pp. 48, 66, 68, 69, 72).
- Fehsenfeld, F. C. and E. E. Ferguson (1971). "Rate constants for the reactions of $CO_2^+ + H$ and $H^+ + CO_2$." en. In: *Journal of Geophysical Research* 76.34, pp. 8453–8454. DOI: [10.1029/JA076i034p08453](https://doi.org/10.1029/JA076i034p08453) (cit. on p. 24).
- Fehsenfeld, F. C., C. J. Howard, and E. E. Ferguson (1973). "Thermal energy reactions of negative ions with H atoms in the gas phase." In: *The Journal of Chemical Physics* 58.12, pp. 5841–5842. DOI: [10.1063/1.1679215](https://doi.org/10.1063/1.1679215) (cit. on pp. 38, 39).
- Gerlich, D. (1992). "Inhomogeneous RF fields: a versatile tool for the study of processes with slow ions." In: *Advances in Chemical Physics* 82.1. DOI: [10.1002/9780470141397.ch1](https://doi.org/10.1002/9780470141397.ch1) (cit. on pp. 3, 13, 17, 31).
- (1995). "Ion-neutral collisions in a 22-pole trap at very low energies." In: *Physica Scripta* 1995.T59, p. 256 (cit. on pp. 31, 32).
- Gerlich, D., G. Borodi, A. Luca, C. Mogo, and M. A. Smith (2011). "Reactions between Cold CH_x^+ and Slow H and H_2 ." In: *Zeitschrift für Physikalische Chemie* 225, pp. 475–492. DOI: [10.1524/zpch.2011.0118](https://doi.org/10.1524/zpch.2011.0118) (cit. on p. 31).
- Gerlich, D. and S. Horning (1992). "Experimental investigation of radiative association processes as related to interstellar chemistry."

- In: *Chemical Reviews* 92.7, pp. 1509–1539. DOI: [10.1021/cr00015a003](https://doi.org/10.1021/cr00015a003) (cit. on pp. [31](#), [32](#)).
- Gerlich, D., P. Jusko, Š. Roučka, I. Zymak, R. Plašil, and J. Glosík (2012). “Ion Trap Studies of $\text{H}^- + \text{H} \rightarrow \text{H}_2 + \text{e}^-$ between 10 and 135 K.” In: *The Astrophysical Journal* 749, 22, p. 22. DOI: [10.1088/0004-637X/749/1/22](https://doi.org/10.1088/0004-637X/749/1/22) (cit. on pp. [34–38](#), [47](#), [71](#)).
- Ghosh, P. (1995). *Ion Traps*. Oxford Science Publications (cit. on p. [3](#)).
- Gilmore, I. and M. Seah (2000). “Ion detection efficiency in SIMS Dependencies on energy, mass and composition for microchannel plates used in mass spectrometry.” In: *International Journal of Mass Spectrometry* 202.1-3, pp. 217–229. DOI: [10.1016/S1387-3806\(00\)00245-1](https://doi.org/10.1016/S1387-3806(00)00245-1) (cit. on p. [20](#)).
- Glosík, J., A. Luca, S. Mark, and D. Gerlich (2000). “Guided ion beam studies of electron and isotope transfer in $^{14}\text{N}^+ + ^{15}\text{N}_2$ collisions.” In: *The Journal of Chemical Physics* 112.16, pp. 7011–7021. DOI: [10.1063/1.481322](https://doi.org/10.1063/1.481322) (cit. on p. [52](#)).
- Glosík, J., P. Hlavenka, R. Plašil, F. Windisch, D. Gerlich, A. Wolf, et al. (2006). “Action spectroscopy of and D_2H^+ using overtone excitation.” In: *Philosophical Transactions of the Royal Society A: Mathematical, Physical and Engineering Sciences* 364.1848, pp. 2931–2942. DOI: [10.1098/rsta.2006.1866](https://doi.org/10.1098/rsta.2006.1866) (cit. on p. [31](#)).
- Glover, S. (Mar. 2008). “Chemistry and Cooling in Metal-Free and Metal-Poor Gas.” In: *First Stars III*. Ed. by B. O’Shea and A. Heger. Vol. 990. American Institute of Physics Conference Series, pp. 25–29. DOI: [10.1063/1.2905558](https://doi.org/10.1063/1.2905558) (cit. on p. [34](#)).
- Glover, S. C., D. W. Savin, and A. Jappsen (2006). “Cosmological Implications of the Uncertainty in H^- Destruction Rate Coefficients.” In: *The Astrophysical Journal* 640.2, pp. 553–568. DOI: [10.1086/500166](https://doi.org/10.1086/500166) (cit. on pp. [1](#), [31](#), [33](#), [47](#)).
- Haxton, D. J., C. W. McCurdy, and T. N. Rescigno (2007). “Dissociative electron attachment to the H_2O molecule I. Complex-valued potential-energy surfaces for the $^2\text{B}_1$, $^2\text{A}_1$, and $^2\text{B}_2$ metastable states of the water anion.” In: *Physical Review A: General Physics* 75 (1), p. 012710. DOI: [10.1103/PhysRevA.75.012710](https://doi.org/10.1103/PhysRevA.75.012710) (cit. on p. [47](#)).
- Heap, S. and T. Stecher (1974). “Two New Physical Processes in the Far-Ultraviolet Spectrum of Zeta Tauri.” In: *The Astrophysical Journal* 187, p. L27. DOI: [10.1086/181384](https://doi.org/10.1086/181384) (cit. on p. [33](#)).
- Hlavenka, P., R. Otto, S. Trippel, J. Mikosch, M. Weidemuller, and R. Wester (2009). “Absolute photodetachment cross section measurements of the O^- and OH^- anion.” In: *Journal of Chemical Physics* 130.6, 061105, p. 061105. DOI: [10.1063/1.3080809](https://doi.org/10.1063/1.3080809) (cit. on p. [58](#)).

- Huang, Y., G.-Z. Li, S. Guan, and A. G. Marshall (1997). "A Combined Linear Ion Trap for Mass Spectrometry." In: *Journal of the American Society for Mass Spectrometry* 8.9, pp. 962–969. DOI: [10.1016/S1044-0305\(97\)82945-5](https://doi.org/10.1016/S1044-0305(97)82945-5) (cit. on p. 52).
- Johnsen, R., A. Chen, and M. A. Biondi (1980). "Three-body association reactions of He⁺, Ne⁺, and Ar⁺ ions in their parent gases from 78 to 300 K." In: *The Journal of Chemical Physics* 73.4, pp. 1717–1720. DOI: [10.1063/1.440307](https://doi.org/10.1063/1.440307) (cit. on pp. 27, 28).
- KATRIN collaboration (2005). *KATRIN Design Report 2004*. Tech. rep. NPI ASCR Řež (cit. on p. 49).
- Kivelson, M. G. and C. T. Russell (1995). *Introduction to Space Physics*. Cambridge University Press (cit. on p. 3).
- Kreckel, H., H. Bruhns, M. Čížek, S. C. O. Glover, K. A. Miller, X. Urbain, et al. (2010). "Experimental Results for H₂ Formation from H⁻ and H and Implications for First Star Formation." In: *Science* 329.5987, pp. 69–71. DOI: [10.1126/science.1187191](https://doi.org/10.1126/science.1187191) (cit. on pp. 2, 39, 47, 71).
- Lee, S. T. and J. M. Farrar (1999). "Vibrational state-resolved study of the O⁻ + H₂ reaction: Isotope effects on the product energy partitioning." In: *Journal of Chemical Physics* 111.16, pp. 7348–7358. DOI: [10.1063/1.480057](https://doi.org/10.1063/1.480057) (cit. on pp. 48, 69).
- Lehmann, A., A. Britting, W. Eylich, and F. Uhlig (2009). "Studies of MCP properties." en. In: *Journal of Instrumentation* 4.11, P11024. DOI: [10.1088/1748-0221/4/11/P11024](https://doi.org/10.1088/1748-0221/4/11/P11024) (cit. on p. 20).
- Lepp, S., P. C. Stancil, and A. Dalgarno (2002). "Atomic and molecular processes in the early Universe." en. In: *Journal of Physics B: Atomic, Molecular and Optical Physics* 35.10, R57. DOI: [10.1088/0953-4075/35/10/201](https://doi.org/10.1088/0953-4075/35/10/201) (cit. on p. 33).
- Li, G. (1989). "Combined Trap and Related Experiments." In: *Communications in Theoretical Physics* 12.4, pp. 355–366 (cit. on p. 52).
- Logg, A., K. A. Mardal, G. N. Wells, et al. (2012). *Automated Solution of Differential Equations by the Finite Element Method*. Springer. DOI: [10.1007/978-3-642-23099-8](https://doi.org/10.1007/978-3-642-23099-8) (cit. on p. 53).
- Logg, A. and G. N. Wells (2010). "DOLFIN: Automated finite element computing." In: *ACM Transactions on Mathematical Software* 37 (2), 20:1–20:28. DOI: [10.1145/1731022.1731030](https://doi.org/10.1145/1731022.1731030) (cit. on p. 53).
- Lucy, L. (1974). "An iterative technique for the rectification of observed distributions." In: *The Astrophysical Journal* 79, p. 745. DOI: [10.1086/111605](https://doi.org/10.1086/111605) (cit. on p. 66).
- Martinez, O., Z. Yang, N. B. Betts, T. P. Snow, and V. M. Bierbaum (2009). "Experimental Determination of the Rate Constant for the

- Associative Detachment Reaction $\text{H}^- + \text{H} \rightarrow \text{H}_2 + \text{e}^-$ at 300 K." In: *The Astrophysical Journal* 705.2, p. L172. DOI: [10.1088/0004-637X/705/2/L172](https://doi.org/10.1088/0004-637X/705/2/L172) (cit. on pp. [24](#), [38](#), [39](#), [47](#)).
- Massey, H. (1976). *Negative Ions*. Cambridge University Press (cit. on pp. [17](#), [18](#)).
- Mauer, J. L. and G. J. Schulz (1973). "Associative Detachment of O^- with CO , H_2 , and O_2 ." In: *Physical Review A: General Physics* 7 (2), pp. 593–605. DOI: [10.1103/PhysRevA.7.593](https://doi.org/10.1103/PhysRevA.7.593) (cit. on pp. [48](#), [69](#), [72](#)).
- McCarthy, M. C., C. A. Gottlieb, H. Gupta, and P. Thaddeus (2006). "Laboratory and Astronomical Identification of the Negative Molecular Ion C_6H^- ." In: *The Astrophysical Journal* 652.2, p. L141. DOI: [10.1086/510238](https://doi.org/10.1086/510238) (cit. on pp. [1](#), [31](#), [33](#)).
- McFarland, M., D. Albritton, F. Fehsenfeld, E. Ferguson, and A. Schmeltekopf (1973). "Flow-drift technique for ion mobility and ion-molecule reaction rate constant measurements. III. Negative ion reactions of O^- with CO , NO , H_2 , and D_2 ." In: *Journal of Chemical Physics* 59, pp. 6629–6635. DOI: [10.1063/1.1680043](https://doi.org/10.1063/1.1680043) (cit. on pp. [39](#), [43](#), [64](#), [65](#), [67](#), [71](#)).
- Milenko, Y., L. Karnatsevich, and V. Kogan (1972). "On temperature dependence of the polarizability of H_2 and D_2 molecules." In: *Physica* 60, pp. 90–96. DOI: [10.1016/0031-8914\(72\)90223-6](https://doi.org/10.1016/0031-8914(72)90223-6) (cit. on p. [44](#)).
- Morenzoni, E., K. Oba, E. Pedroni, and D. Taqqu (1988). "Performance of microchannel plates in high magnetic fields." In: *Nuclear Instruments and Methods in Physics Research Section A: Accelerators, Spectrometers, Detectors and Associated Equipment* 263.2-3, pp. 397–400. DOI: [10.1016/0168-9002\(88\)90977-1](https://doi.org/10.1016/0168-9002(88)90977-1) (cit. on p. [20](#)).
- Moruzzi, J. L. and A. V. Phelps (1966). "Survey of Negative-Ion-Molecule Reactions in O_2 , CO_2 , H_2O , CO , and Mixtures of These Gases at High Pressures." In: *The Journal of Chemical Physics* 45.12, pp. 4617–4627. DOI: [10.1063/1.1727545](https://doi.org/10.1063/1.1727545) (cit. on p. [39](#)).
- Moseler, M., B. Huber, H. Häkkinen, U. Landman, G. Wrigge, M. A. Hoffmann, et al. (2003). "Thermal effects in the photoelectron spectra of Na_N^- clusters ($N = 4-19$)." In: *Physical Review B* 68 (16), p. 165413. DOI: [10.1103/PhysRevB.68.165413](https://doi.org/10.1103/PhysRevB.68.165413) (cit. on p. [49](#)).
- Otto, R., J. Mikosch, S. Trippel, M. Weidemuller, and R. Wester (2008). "Nonstandard Behavior of a Negative Ion Reaction at Very Low Temperatures." In: *Physical Review Letters* 101.6, p. 063201. DOI: [10.1103/PhysRevLett.101.063201](https://doi.org/10.1103/PhysRevLett.101.063201) (cit. on p. [71](#)).
- Plašil, R., I. Zymak, P. Jusko, D. Mulin, D. Gerlich, and J. Glosík (2012). "Stabilization of H^+-H_2 collision complexes between 11 and 28

- K." en. In: *Philosophical Transactions of the Royal Society A: Mathematical, Physical and Engineering Sciences* 370.1978, pp. 5066–5073. DOI: [10.1098/rsta.2012.0098](https://doi.org/10.1098/rsta.2012.0098) (cit. on p. 29).
- Plašil, R., T. Mehner, P. Dohnal, T. Kotrík, J. Glosík, and D. Gerlich (2011). "Reactions of cold trapped CH^+ ions with slow H atoms." In: *The Astrophysical Journal* 737.2, p. 60. DOI: [10.1088/0004-637X/737/2/60](https://doi.org/10.1088/0004-637X/737/2/60) (cit. on p. 31).
- Rellergert, W. G., S. T. Sullivan, S. Kotochigova, A. Petrov, K. Chen, S. J. Schowalter, et al. (2011). "Measurement of a Large Chemical Reaction Rate between Ultracold Closed-Shell ^{40}Ca Atoms and Open-Shell $^{174}\text{Yb}^+$ Ions Held in a Hybrid Atom-Ion Trap." In: *Physical Review Letters* 107 (24), p. 243201. DOI: [10.1103/PhysRevLett.107.243201](https://doi.org/10.1103/PhysRevLett.107.243201) (cit. on p. 49).
- Richardson, W. H. (1972). "Bayesian-Based Iterative Method of Image Restoration." In: *Journal of the Optical Society of America* 62.1, pp. 55–59. DOI: [10.1364/JOSA.62.000055](https://doi.org/10.1364/JOSA.62.000055) (cit. on p. 66).
- Rossi, F. and G. I. Opat (1992). "Observations of the effects of adsorbates on patch potentials." In: *Journal of Physics D: Applied Physics* 25.9, p. 1349. DOI: [10.1088/0022-3727/25/9/012](https://doi.org/10.1088/0022-3727/25/9/012) (cit. on p. 56).
- Ross, T., E. Baker, T. Snow, J. Destree, B. Rachford, M. Drosback, et al. (2008). "The Search for H^- in Astrophysical Environments." In: *The Astrophysical Journal* 684, pp. 358–363. DOI: [10.1086/590242](https://doi.org/10.1086/590242) (cit. on pp. 1, 33).
- Roučka, Š. (2012). "Laboratory Astrochemistry and Applications of Computer Simulations." PhD thesis. Charles University in Prague, Faculty of Mathematics and Physics (cit. on pp. 29, 52, 53, 57, 68).
- Sakimoto, K. (1989). "Ion-molecule reactions at extremely low energies: $\text{H}^- + \text{H} \rightarrow \text{H}_2 + \text{e}^-$." In: *Chemical Physics Letters* 164.2-3, pp. 294 – 298. DOI: [10.1016/0009-2614\(89\)85032-8](https://doi.org/10.1016/0009-2614(89)85032-8) (cit. on p. 38).
- Schmeltekopf, A., F. Fehsenfeld, and E. Ferguson (1967). "Laboratory measurement of the rate constant for $\text{H}^- + \text{H} \rightarrow \text{H}_2 + \text{e}^-$." In: *The Astrophysical Journal* 148, p. L155. DOI: [10.1086/180035](https://doi.org/10.1086/180035) (cit. on pp. 38, 39).
- Scott, G. B., D. A. Fairley, C. G. Freeman, M. J. McEwan, P. Spanel, and D. Smith (1997). "Gas phase reactions of some positive ions with atomic and molecular hydrogen at 300 K." In: *The Journal of Chemical Physics* 106.10, pp. 3982–3987. DOI: [10.1063/1.473116](https://doi.org/10.1063/1.473116) (cit. on p. 24).
- Slevin, J. and W. Stirling (1981). "Radio frequency atomic hydrogen beam source." In: *Review of Scientific Instruments* 52.11, pp. 1780–1782. DOI: [10.1063/1.1136497](https://doi.org/10.1063/1.1136497) (cit. on p. 21).

- Smith, I. W. M. and D. Gerlich (2008). "The Study of Cold Collisions Using Ion Guides and Traps." In: *Low Temperatures And Cold Molecules*. Imperial College Press London, pp. 121–174. DOI: [10.1142/9781848162105_0003](https://doi.org/10.1142/9781848162105_0003) (cit. on pp. 27, 28).
- Smith, M. A. and S. R. Leone (1983). "Product vibrational state distributions in thermal energy associative detachment reactions: $F^- + H, D \rightarrow HF(v), DF(v) + e^-$." In: *Journal of Chemical Physics* 78.3, pp. 1325–1334. DOI: [10.1063/1.444870](https://doi.org/10.1063/1.444870) (cit. on pp. 47, 69).
- Tawara, H., Y. Itikawa, H. Nishimura, and M. Yoshino (1989). "Cross Sections and Related Data for Electron Collisions with Hydrogen Molecules and Molecular Ions." In: *Journal of Physical and Chemical Reference Data* 19, pp. 617–636. DOI: [10.1063/1.555856](https://doi.org/10.1063/1.555856) (cit. on p. 17).
- Tosi, P., S. Iannotta, D. Bassi, H. Villinger, W. Dobler, and W. Lindinger (1984). "The reaction of CO_2^+ with atomic hydrogen." In: *The Journal of Chemical Physics* 80.5, pp. 1905–1906. DOI: [10.1063/1.446951](https://doi.org/10.1063/1.446951) (cit. on p. 24).
- Wang, W., A. K. Belyaev, Y. Xu, A. Zhu, C. Xiao, and X.-F. Yang (2003). "Observations of H_3^- and D_3^- from dielectric barrier discharge plasmas." In: *Chemical Physics Letters* 377.5-6, pp. 512–518. DOI: [10.1016/S0009-2614\(03\)01210-7](https://doi.org/10.1016/S0009-2614(03)01210-7) (cit. on pp. 44, 45).
- Werner, H. J., U. Manz, and P. Rosmus (1987). "On the structure and stability of the H_2O^- ion." In: *The Journal of Chemical Physics* 87.5, pp. 2913–2918. DOI: [10.1063/1.453079](https://doi.org/10.1063/1.453079) (cit. on p. 47).
- Živanov, S., M. Čížek, J. Horáček, and M. Allan (2003). "Electron spectra for associative detachment in low-energy collisions of Cl^- and Br^- with H and D." In: *Journal of Physics B: Atomic, Molecular and Optical Physics* 36.16, p. 3513. DOI: [10.1088/0953-4075/36/16/312](https://doi.org/10.1088/0953-4075/36/16/312) (cit. on pp. 47, 69).

LIST OF PUBLICATIONS

PUBLICATIONS IN PREPARATION

Jusko, P., Š. Roučka, R. Plašil, and J. Glosík (2013). "Determining the energy distribution of electrons produced in associative detachment: The Electron Spectrometer with Multipole Trap." In: *International Journal of Mass Spectrometry*. Submitted.

PUBLICATIONS IN JOURNALS WITH IMPACT FACTOR

Gerlich, D., P. Jusko, Š. Roučka, I. Zymak, R. Plašil, and J. Glosík (Apr. 2012). "Ion Trap Studies of $H^- + H \rightarrow H_2 + e^-$ between 10 and 135 K." In: *The Astrophysical Journal* 749, 22, p. 22. DOI: [10.1088/0004-637X/749/1/22](https://doi.org/10.1088/0004-637X/749/1/22).

Gerlich, D., R. Plašil, I. Zymak, M. Hejduk, P. Jusko, D. Mulin, et al. (2013). "State specific stabilization of $H^+ + H_2(j)$ collision complex." In: *The journal of Physical Chemistry A*. Online. DOI: [10.1021/jp400917v](https://doi.org/10.1021/jp400917v).

Kotrík, T., P. Dohnal, Š. Roučka, P. Jusko, R. Plašil, J. Glosík, et al. (Mar. 2011). "Collisional-radiative recombination $Ar^+ + e + e$: Experimental study at 77–180 K." In: *Physical Review A: General Physics* 83 (3), p. 032720. DOI: [10.1103/PhysRevA.83.032720](https://doi.org/10.1103/PhysRevA.83.032720).

Plašil, R., I. Zymak, P. Jusko, D. Mulin, D. Gerlich, and J. Glosík (Nov. 2012). "Stabilization of $H^+ - H_2$ collision complexes between 11 and 28 K." en. In: *Philosophical Transactions of the Royal Society A: Mathematical, Physical and Engineering Sciences* 370.1978, pp. 5066–5073. DOI: [10.1098/rsta.2012.0098](https://doi.org/10.1098/rsta.2012.0098).

Zymak, I., P. Jusko, Š. Roučka, R. Plašil, P. Rubovič, D. Gerlich, et al. (Nov. 2011). "Ternary association of H^+ ion with H_2 at 11 K, experimental study." In: *European Physical Journal—Applied Physics* 56.2. DOI: [10.1051/epjap/2011110172](https://doi.org/10.1051/epjap/2011110172).

PUBLICATIONS IN WOS REGISTERED PROCEEDINGS

Plašil, R., I. Zymak, P. Jusko, D. Mulin, D. Gerlich, and J. Glosík (2012). "Radiative association of H^+ and H_2 – experimental study." In:

Journal of Physics Conference Series 388, 012041 (6 pp.) DOI: [10.1088/1742-6596/388/1/012041](https://doi.org/10.1088/1742-6596/388/1/012041).

Roučka, Š., P. Jusko, I. Zymak, D. Mulin, R. Plašil, D. Gerlich, et al. (2012). "Interactions of H^- Anions with Atomic Hydrogen-Ion Trap study at 10-100 K." In: *Journal of Physics Conference Series* 388, 082057 (1 pp.) DOI: [10.1088/1742-6596/388/8/082057](https://doi.org/10.1088/1742-6596/388/8/082057).

LIST OF FIGURES

Figure 1	Particle motion in $E \perp B$ field	5
Figure 2	Particle motion in magnetic field $\nabla B \parallel B$	6
Figure 3	Magnetic mirror trap and the escape cone	8
Figure 4	Dirichlet problem for the Laplace's equation	11
Figure 5	Effective potential and adiabaticity parameter in an octopole	14
Figure 6	Mathieu stability diagram	15
Figure 7	Ion source (schematic diagram)	18
Figure 8	Ion mass selecting quadrupole characteristics	19
Figure 9	MCP electrical connection	19
Figure 10	MCP Pulse Height Distribution	21
Figure 11	MCP detection efficiency in various magnetic fields	22
Figure 12	H atom source (schematic diagram)	23
Figure 13	Time of flight spectra of atomic H in the beam	24
Figure 14	Dissociation ratio α in the H/H ₂ beam	25
Figure 15	H beam density calibration	26
Figure 16	He association – apparent binary rate coefficient	27
Figure 17	Temperature dependence of He ternary association coefficient	28
Figure 18	22-pole trap apparatus (cut)	32
Figure 19	AB-22PT apparatus (schematic diagram)	34
Figure 20	Relative number of H ⁻ as a function of storage time	36
Figure 21	Measured H ⁻ + H rate coefficient as a function of temperature	37
Figure 22	Comparison of measured H ⁻ + H rate coefficient with previous works	38
Figure 23	Relative number of O ⁻ and OH ⁻ as a function of storage time	39
Figure 24	Measured O ⁻ + H ₂ rate coefficient as a function of temperature	40
Figure 25	Measured O ⁻ + D ₂ rate coefficient as a function of temperature	41
Figure 26	Measured O ⁻ + D ₂ reaction rate as a function of D ₂ number density.	42

Figure 27	Comparison of measured $O^- + H_2$ rate coefficient with previous works	43
Figure 28	Isotope effect in the reaction of O^- with H_2 and D_2	44
Figure 29	Relative number of D^- as a function of storage time – hypothetical D_3^- production	45
Figure 30	ES-MPT apparatus (schematic diagram)	48
Figure 31	ES-MPT magnetic field configuration (model)	53
Figure 32	Measured magnetic field in the ES-MPT	54
Figure 33	The measured spectra of electrons produced by thermionic emission from hot filament	56
Figure 34	Resolution of the MAC-E filter as a function of electron energy	57
Figure 35	Influence of the rf field to the measured electron spectra	58
Figure 36	Influence of the magnetic field to the measured electron spectra	59
Figure 37	Influence of the magnetic field intensity to ion storage time	60
Figure 38	Laser O^- photodetachment experiment	61
Figure 39	Measured spectra of electrons photodetached from O^- anions	63
Figure 40	Spectra of electrons produced from O^- and OH^-	64
Figure 42	Indirect method of trapped anions detection	66
Figure 43	Measured electron energy spectra in the reactions of $O^- + H_2, D_2$ and CO	68
Figure 44	AB-22-pt CAD drawing	75
Figure 45	ES-MPT CAD drawing	76

LIST OF TABLES

Table 1	Ionization cross sections for precursor gases	17
Table 2	Diameter of an ion cloud in 22-pole trap	35
Table 3	Overview of the laser wavelengths used in the photodetachment experiments	62
Table 4	Comparison of measured $O^- + H_2, D_2$ reaction rate coefficient	67
Table 5	Electron affinities of the elements in eV	77

LISTINGS

Listing 1	Script for evaluation of quadrupole transmission properties	79
Listing 2	Script for effective potential evaluation	80

ACRONYMS

AB 22-pt *Atomic beam – 22-pole trap*

22-pt *22-pole trap*

SIS *Storage Ion Source*

QMS *Quadrupole Mass Spectrometer*

TOF *Time of Flight*

ES-MPT *Electron Spectrometer with Multipole Trap*

MCP *Micro Channel Plate*

MCS *Multi Channel Scaler*

HAS *H Atom Source*

AD *Associative Detachment*

ISM *Interstellar Medium*

RA *Radiative Association*

PTFE *Polytetrafluoroethylene – Teflon*

Part II

ATTACHED ARTICLES

ARTICLE I

TITLE: Ion trap studies of $\text{H}^- + \text{H} \rightarrow \text{H}_2 + \text{e}^-$ between 10 and 135 K

AUTHORS: Dieter Gerlich, Pavol Jusko, Štěpán Roučka, Illia Zymak,
Radek Plašil, and Juraj Glosík

JOURNAL: The Astrophysical Journal, 749:22 (6 pp)

DATE: 19. March 2012

DOI: [10.1088/0004-637X/749/1/22](https://doi.org/10.1088/0004-637X/749/1/22)

ION TRAP STUDIES OF $\text{H}^- + \text{H} \rightarrow \text{H}_2 + e^-$ BETWEEN 10 AND 135 K

DIETER GERLICH^{1,2}, PAVOL JUSKO¹, ŠTĚPÁN ROUČKA¹, ILLIA ZYMAK¹, RADEK PLAŠIL¹, AND JURAJ GLOŠÍK¹

¹ Faculty of Mathematics and Physics, Charles University, 18000 Prague, Czech Republic

² Faculty of Natural Science, Technical University, 09107 Chemnitz, Germany

Received 2011 December 7; accepted 2012 January 26; published 2012 March 19

ABSTRACT

Thermal rate coefficients for forming H_2 via associative detachment in $\text{H}^- + \text{H}$ collisions were determined using the combination of a 22-pole ion trap (22PT) with a skimmed effusive beam of atomic hydrogen penetrating the ion cloud. The temperature of both reactants have been varied independently (ion trap: $T_{22\text{PT}} = 10\text{--}150$ K, neutral beam accommodator $T_{\text{ACC}} = 10, 50, 120$ K). Using various combinations, the temperature range between 10 and 135 K has been accessed for the first time experimentally. The effective number density of H (typically some 10^8 cm^{-3}) is determined in situ via chemical probing with CO_2^+ ions. With decreasing temperature, the measured thermal rate coefficients decrease slowly from $5.5 \times 10^{-9} \text{ cm}^3 \text{ s}^{-1}$ at 135 K to $4.1 \times 10^{-9} \text{ cm}^3 \text{ s}^{-1}$ at 10 K. The relative error is 10%, while the absolute values may deviate systematically by up to 40%, due to uncertainties in the calibration reaction. Significant improvements of the versatile and sensitive experiment are possible, e.g., by using electron transfer from H to D^+ as calibration standard.

Key words: astrochemistry – atomic processes – early Universe – methods: laboratory – molecular processes

Online-only material: color figures

1. INTRODUCTION

The evolution of matter in the early universe toward the formation of the first stars is determined by atomic and molecular processes involving mainly hydrogen (H, D), helium (^3He , ^4He), electrons, and radiation. Traces of lithium and beryllium are assumed to play only a minor role. Since the elemental composition remains unchanged during this period, one could expect that primordial chemistry is rather simple. However, up to 200 reactions can contribute to the abundance of 23 atomic and molecular species as pointed out by Lepp et al. (2002). Important for star formation is the role of molecules as coolants, i.e., the conversion of translational energy into internal degrees of freedom via inelastic or reactive collisions, followed by radiative transitions.

There has been significant progress in improving the models which predict abundances of molecules and their role as coolants; however, in all these models, most chemical reactions are described just by simple temperature-dependent rate coefficients whereas, in principle, one would need state-to-state cross sections (or elementary rate coefficients) for describing the non-equilibrium chemistry. An example of central importance is the scrambling reaction of H^+ with H_2 and isotopic variants. This collision system is very efficient in converting kinetic energy into internal excitation of the product molecule. Important for the spectrum of the emitted radiation is that not only does vibration play a role but that also rotational states are populated very efficiently to the limit given by the available energy. A recent extensive comparison between theoretical and experimental results for collisions of $\text{H}^+ + \text{D}_2$ and $\text{D}^+ + \text{H}_2$ corroborates this statement (Jambrina et al. 2012).

Several specific uncertainties in the reaction network describing the primordial chemistry have been discussed in recent years. A special problem is the efficiency to form H_2 , the most abundant molecule, and HD, which is important because it has a dipole moment (Glover et al. 2006). But also molecules such as H_3^+ and its isotopic variants or HeH^+ are considered to be important trace molecules and coolants (Glover & Abel 2008; Puy &

Signore 2007). An interesting case is the HeH^+ ion. This ion (or He_2^+) is the first molecule ever formed in the primordial universe and, in sequential collisions with H atoms, first H_2^+ and then H_2 is formed. A new ab initio calculation for the proton transfer rate coefficient in $\text{HeH}^+ + \text{H}$ recently led to the conclusion that the abundance of HeH^+ is more than one order of magnitude higher than previously predicted (Bovino et al. 2011).

Formation of a hydrogen molecule from two H atoms under early universe conditions requires a catalytic gas phase reaction such as $\text{H}^+ + \text{H} \rightarrow \text{H}_2^+ + h\nu$ followed by $\text{H}_2^+ + \text{H} \rightarrow \text{H}_2 + \text{H}^+$. Besides the proton, an efficient catalyst is the electron, as soon as conditions are such that the lifetime of H^- gets long enough. The sequence is radiative attachment $e^- + \text{H} \rightarrow \text{H}^- + h\nu$ followed by associative detachment (AD)



Due to bound-free, free-bound, and free-free transitions, the ($\text{H}-e^-$) system plays an important role in the universe, for example for the continuum opacity of late-type stars or in establishing a thermal equilibrium in the photosphere of a star. Despite its abundance, H^- not yet has been observed directly via a specific transition (in the UV; see Ross et al. 2008 and references therein).

The central role of H^- in the primordial chemistry and consequences of uncertainties in several rate coefficients have been discussed by Glover et al. (2006) and Glover & Abel (2008). Theoretical calculations for reaction (1) disagreed among each other in the range of $(1\text{--}5) \times 10^{-9} \text{ cm}^3 \text{ s}^{-1}$ (Sakimoto 1989; Launay et al. 1991; Cizek et al. 1998). A few years ago, the only experimental results have been from flow tubes operated at room temperature and using two different schemes for producing the H atoms (Schmeltekopf et al. 1967; Fehsenfeld et al. 1973; Martinez et al. 2009).

Meanwhile, the situation has changed due to new experimental and theoretical activities. At Columbia University, D. W. Savin and coworkers have constructed a dedicated instrument based on the merged beams principle. Using a 10 keV fast H^- beam and converting a fraction of the ions into neutral atoms

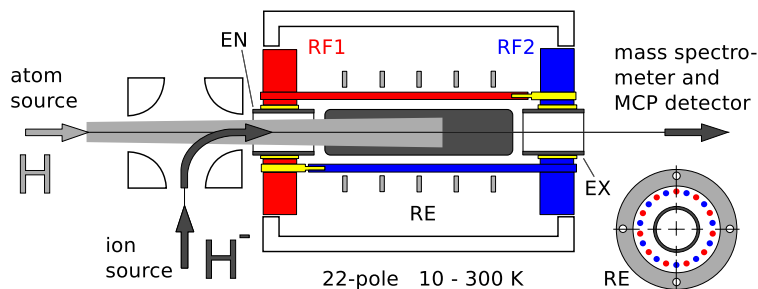


Figure 1. Detailed drawing of the central part of the 22-pole ion trap apparatus. H^- ions are injected into the trap via the electrostatic quadrupole bender. To the right, ions move via the quadrupole mass spectrometer towards the detector. The cold effusive H-atom beam comes from the left. The gray shaded areas indicate the overlap between the ion cloud and the neutral beam. For photodetachment studies, a laser beam is injected from the right.

(A color version of this figure is available in the online journal.)

via photodetachment (PD), reaction (1) could be studied at collision energies between 4 meV and 1 eV (Bruhns et al. 2010). Recently an extension to 4.8 eV has been reported by Miller et al. (2011). Despite the fact that the merged beams technology is rather complex and that the precise detection of the neutral H_2 products from reaction (1) is a challenge, rate coefficients have been determined with rather high accuracy, the total systematic error has been estimated to be only $\pm 24\%$ (Kreckel et al. 2010; Bruhns et al. 2010; Miller et al. 2011).

The merged beams results are in very good agreement with calculated cross sections (Cizek et al. 1998) but there is still a discrepancy, not only with the above-mentioned old flow tube measurements but also with recent rate coefficients determined at the University of Colorado, Boulder, with a tandem flowing afterglow–selected ion flow tube (Martinez et al. 2009). The old and new flow tube measurements agree with each other; however, they are a factor of 2.2 ± 0.9 smaller than the recently slightly correct merged beams results (Miller et al. 2011). It has been suspected in Bruhns et al. (2010) that the discrepancy may be due to an error in the AD calibration reaction $\text{Cl}^- + \text{H}$ used for determining the H-atom density in the flow tube. Looking at the recent activities related to the specific reaction (1) and realizing that there are certainly more uncertainties in the models simulating the processes in the pregalactic era, it becomes obvious that more dedicated experimental activities are needed.

In the following, we report first results for reaction (1) obtained with an ion trapping instrument, a versatile method which is complementary to the two experimental methods mentioned above and which allows us to extend the temperature range down to 10 K. After a short description of the ion trap and the effusive H-atom beam, new data are presented with emphasis on the accuracy of the absolute values, achieved so far and on planned improvements, especially concerning the determination of the effective number density of the reactants. In the outlook we will mention other primordial reactions which can be studied using temperature variable ion traps and give a short summary to ongoing activities for detecting the electrons produced by reaction (1).

2. EXPERIMENTAL

2.1. 22PT Ion Trap

The instrument used in this study was developed at the Chemnitz University of Technology and is now operated

successfully at the Charles University in Prague. It is based on the combination of a radio-frequency (rf) 22-pole ion trap with an effusive beam source for atomic hydrogen (AB-22PT). The method of using inhomogeneous rf fields for storing ions has been summarized in Gerlich (1992). Technical details of the present experimental setup can be found in Borodi (2008) and Borodi et al. (2009). Previous studies of the interaction of stored CH_n^+ ions with H atoms have been reported in Gerlich et al. (2011) and Plasil et al. (2011).

The geometry of the region where the trapped ion cloud and the neutral beam interact is shown in some detail in Figure 1. The importance of determining the effective volume where the reactants overlap is discussed below. Primary H^- ions are produced by electron bombardment of H_2 precursor gas in a storage ion source (Gerlich 1992). After prethermalization in the source, the ions are mass selected using a quadrupole filter, bent by 90° using an electrostatic quadrupole and injected into the 22-pole trap. In the radial direction, the ions are confined by the rf field created by two sets of 11 poles (RF1 and RF2) precisely mounted on both sides. The potential inside the trap can be corrected locally using the five ring electrodes (RE). The entrance and exit electrode (EN and EX) are used to open and close the trap with electrostatic barriers of some tens of meV. After various storage times the exit electrode is opened, the ions leave the trap, pass through the QP mass spectrometer, and they are converted into a short current pulse using a micro channel plate detector (MCP assembly F4655-12, Hamamatsu). The pulses are accumulated in a 100 MHz counter.

The standard sequence (1) filling the trap repetitively with a well-defined number of primary ions, (2) storing them for various times, and (3) detecting them is averaged over many iterations, for reducing the statistical errors. For comparison, the number of ions, $N_i(t)$, is normalized to one iteration or normalized to the total number of ions. In general, there is no loss of ions, i.e., the total number per filling remains constant. In the present experiment, the charged products from the AD reaction are electrons which cannot be detected in the current experimental setup. A method to guide them out from the rf field by superimposing a suitable magnetic field is under development.

The temperature of the ion trap, T_{22PT} , can be varied between 10 K and 300 K. Ions are cooled to the trap temperature by collisions with H_2 buffer gas. For relaxing the kinetic energy of H^- , a few collisions are sufficient. As discussed by Gerlich (1992) and emphasized in Gerlich (2008a), the influence of the micromotion driven by the oscillating confining field—effects referred to as radio frequency heating—is negligible if high

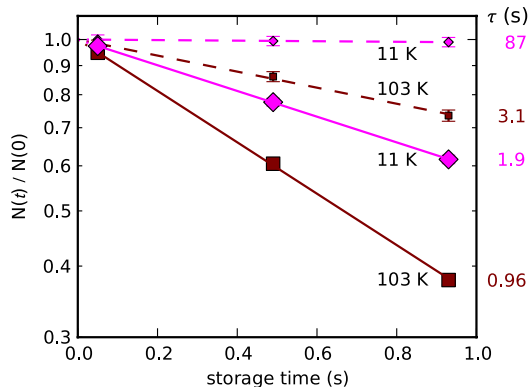


Figure 2. Relative number of H^- ions per filling as a function of storage time (ion trap temperature: $T_{22\text{PT}} = 11$ and 103 K, hydrogen beam temperature $T_{\text{ACC}} = 50$ K, small and large symbols correspond to H-atom beam OFF and ON, respectively). The statistical errors are in the order of or smaller than the size of the symbols. Fitting the data with $\exp(-t/\tau)$ (solid and dashed lines) leads to the time constants τ shown on the right.

(A color version of this figure is available in the online journal.)

enough frequencies are used. Problems may be caused by potential distortions or parasitic low frequency fields.

2.2. Atomic Beam

H atoms are produced by dissociation of H_2 in an rf discharge operating at 0.2 mbar and a gas flow of 5×10^{-3} mbar 1 s^{-1} . For slowing down the gas emerging from the hot discharge, an accommodator is used the temperature of which can be tuned to $6 \text{ K} < T_{\text{ACC}} < 300 \text{ K}$. It consists of a channel in a copper block (2 mm diameter, length 22 mm) which is coated with a $\sim 50 \mu\text{m}$ thick layer of PTFE for reducing recombination. A mechanical shutter can block the H beam (beam ON or OFF). The geometrical arrangement of apertures and differential pumping ensures that a well-collimated beam (divergence $< 1^\circ$) passes through the trap without hitting any surface. The gray shaded areas in Figure 1 indicate the overlap between the ion cloud and the neutral beam. The volume of the ion cloud is $\sim 1.5 \text{ cm}^3$, the interaction volume is about one quarter.

The actual velocity distributions of atoms and molecules emerging from the accommodator have been determined using time-of-flight measurements. The obtained distributions are in a good agreement with Maxwellians the actual temperatures of which are very close to the accommodator temperature. Deviations are less than 2 K or a few percent, whichever is larger. In deviation from the description in Borodi et al. (2009), all measurements of this study have been performed without hexapole magnets for focusing the beam of H atoms. Although this leads to a much lower effective number density in the trap (about one order of magnitude; see Borodi et al. 2009), it has the advantage that one can use flux conservation for absolute calibration, i.e., the total number of H flowing through the accommodator (as atom or in a molecule) remains unchanged if the discharge is switch on or off.

2.3. Typical Raw Data

Figure 2 shows a typical set of raw data. Plotted is the relative number of H^- ions per filling, $N(t)/N(0)$, as a function of trapping time. The repetition period was set to 1 s. The number of initially injected ions, typically 100 H^- per filling, is checked after 20 ms, when most of them have already been thermalized

Table 1
Diameter of the Ion Cloud (d_1 for H^- and d_2 for CO_2^+ for Different Kinetic Energies E of the Ions Calculated from the Effective Potential (Gerlich 1992)

E (meV)	d_1 (mm)	d_2 (mm)	$(d_1/d_2)^2$
100	9.21	8.17	1.271
10	8.21	7.28	1.272
1	7.32	6.49	1.272

Notes. The 22-pole has been operated with $\Omega/2\pi = 18$ MHz and $V_0 = 50$ V and 25 V for mass 44 and 1, respectively. Note that the inner free diameter of the 22-pole is 10 mm. Assuming that the kinetic energy distributions of CO_2^+ and H^- are the same, the volume of the CO_2^+ cloud is about 1.27 times the volume of the H^- ions as can be seen from $(d_1/d_2)^2$, the ratio of the areas.

in collisions with ambient hydrogen. Typically H_2 densities have been 10^{12} cm^{-3} , mainly from the ion source gas. Higher densities have also been tested without any effect. Extracting the ions at later times reveals a more or less slow loss, depending on the temperature of the trap and on the presence of the H-atom beam (small symbols and dashed lines: beam OFF, large symbols and solid lines: beam ON). The data have been fitted with exponential functions, resulting in time constants τ longer than 1 minute and shorter than 1 s (see numbers on the right side of Figure 2). Without H atoms the slow loss of primary ions is caused by reactions with ambient background gas. At 11 K, cryopumping inside the trap leads to long storage times. For extending the measurements toward higher temperatures, better vacuum conditions are needed. The rate coefficients for reaction (1) are simply determined from the difference of the rates with the H beam ON and OFF and the effective number density of the H atoms.

2.4. Effective Number Density

In order to extract absolute rate coefficients from the experiment, one has to account for the spatial distribution of the reactants and for their velocity distributions. Special aspects concerning kinematic averaging in neutral beam-ion trap arrangements can be found in Gerlich (2008a, 2008b) and Gerlich & Borodi (2009). For determining the distribution of the relative velocity, it is safe to assume in the present arrangement that we have two ensembles, thermalized to $T_{22\text{PT}}$ and T_{ACC} . In such a case the temperature (in the center-of-mass frame) is the mass-weighted average of the two temperatures. For reaction (1) one gets

$$T = (T_{22\text{PT}} + T_{\text{ACC}})/2. \quad (2)$$

Note that in our beam-trap arrangement reactions occur only in the nearly field-free region, since the target density goes to zero in regions of large amplitude micromotion. As indicated in Figure 1, it is straightforward to account for the spatial overlap, at least under ideal conditions, i.e., a well-skimmed neutral beam with a diameter of 4 mm, an angular divergence of 0.7° and a homogeneous density in the region of overlap, and an ion cloud the distribution of which is determined by the effective potential and the temperature of the ions. Some parameters relevant for trapping H^- can be found in Table 1. In the axial direction, the electrodes EN and EX are used to close the trap with dc voltages. A few tens of mV are sufficient for confining the ions.

In reality the potential of the ion trap may be influenced by geometrical effects, by perturbations of the surface potential, or by other stray fields. Related experimental tests and strategies to avoid or reduce such effects have been discussed in Gerlich

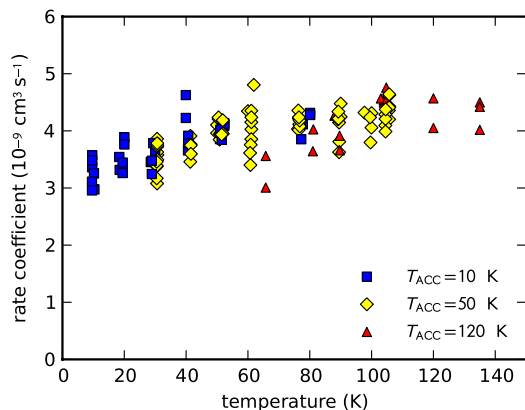


Figure 3. Measured rate coefficients, shown as a function of the translational temperature. The data shown as squares, diamonds, and triangles have been measured at $T_{\text{ACC}} = 10, 50,$ and 120 K, respectively. Variation of $T_{22\text{PT}}$ between 10 and 150 K covers each time a range of 70 K (in the center-of-mass system). (A color version of this figure is available in the online journal.)

(1992, 2008a). An odd situation has been reported by Otto et al. (2009). The spatial distribution of the ion cloud on a 22-pole, imaged by PD, showed 10 intensity maxima close to the rods. The origin of this effect can be explained by the superposition of a dipolar field, caused by a misalignment of the two sets of electrodes against each other. In our trap (see Figure 1), all 22 rods are localized rather precisely on each end. Nonetheless we observed that, at lower temperatures, the ions spend more time close to the rods than predicted from calculations. Some tests have been performed via PD with a 660 nm laser beam. Going from 100 to 10 K the PD rate dropped by 20% instead of an increase of 30% expected from the fact that colder ions are confined closer to the axis of the trap. This indicates that there are some forces attracting the ions toward the electrodes. Improvements are possible by cleaning or also by using the RE (see Figure 1), if the perturbations are localized. An alternative solution is to use a reaction for calibrating the effective overlapping volume as described in the following.

Since it cannot be excluded that the ion distribution is affected by perturbations or that some H atoms were hitting the surface of the entrance or exit electrode in the present experiment, we decided to determine the effective number density via chemical probing with CO_2^+ . This method has the advantage that it accounts automatically for the real overlap integral of the spatial distributions of ions and neutrals. As described by Borodi et al. (2009), collisions of CO_2^+ with molecular hydrogen lead to HCO^+ while collisions with H atoms produce HCO^+ . The rate coefficients for the last reaction are independent on the temperature of the CO_2^+ ions and on the velocity of the atoms. Borodi et al. (2009) recommend a value of $k(T) = 4.6 \times 10^{-10} \text{ cm}^3 \text{ s}^{-1}$ for H as target, and $2.2 \times 10^{-10} \text{ cm}^3 \text{ s}^{-1}$ for D. The uncertainty was conservatively estimated to be 40%.

In the present experiment the H-atom density was measured routinely between several runs at an accommodator temperature $T_{\text{ACC}} = 50$ K, using the probing reaction. Depending on the conditions of the discharge tube, typical values of some 10^8 cm^{-3} have been obtained. The results have been corrected for the mass dependence of the effective potential which scales with $V_0^2/(m\Omega^2)$. Selected ion trap parameters used for CO_2^+ and H^- are given in Table 1.

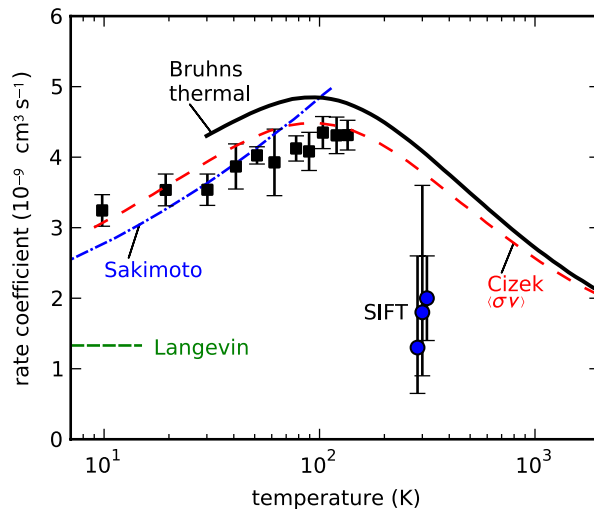


Figure 4. Comparison of our ion trap results (squares; bars indicate the statistical errors; the systematic uncertainty is larger; see the text) with previous measurements and results from theory. The solid line indicates the thermal rate coefficient $k(T)$, derived from the merged beams data published by Bruhns et al. (2010). The theoretical results of Sakimoto (1989) and Cizek et al. (1998) are in good overall accord agreement, while the Langevin limit and the 300 K flow tube measurements are significantly smaller (from left to right: Schmeltekopf et al. 1967; Fehsenfeld et al. 1973; Martinez et al. 2009; shifted for better readability). (A color version of this figure is available in the online journal.)

3. RESULTS AND DISCUSSION

Rate coefficients for reaction (1) have been measured in several iterations and under various conditions as described above. Usually data were collected by holding the accommodator temperature fixed and by varying the 22-pole temperature between 10 and 150 K. Higher trap temperatures could not be used because of ion loss due to reactions with gas impurities. Figure 3 shows a collection of typical sets of data as a function of translational temperature, each of them covering a range of 70 K. As indicated, the different symbols correspond to $T_{\text{ACC}} = 10, 50,$ and 120 K. The 50 K values are absolute based on the calibration reaction while the two other sets of measurements have been matched to them using the region where the data overlap. Higher temperatures T_{ACC} are possible; however, the dissociation degree of the H-atom source decreases (Borodi 2008). The overall trend is well reproduced accounting for the statistical uncertainties of each data point. All individual data were reduced by binning leading to the result plotted in Figure 4. The error bars represent the standard deviation of each data point. Not shown is the fact that there is a systematic uncertainty of 40%. As discussed above it is caused by the calibration reactions. Below 20 K the actual ion temperature may be higher by up to 5 K, at higher temperatures the error is less than 2%.

In the overlapping regime, our results are in good accordance with the results from Bruhns et al. (2010). For better comparison, their experimental results which have a total systematic uncertainty of 24% are represented just by the solid curve taken from Figure 10 of Bruhns et al. (2010). Note that this curve, showing the derived thermal rate coefficients, should be shifted up by 8.6% according to a recent new evaluation (Miller et al. 2011). For solving the discrepancy with the flow measurements, it is mandatory to extend the ion trap experiments to higher temperatures. This is possible by improving the vacuum conditions,

e.g., by mounting the trap on a different support such that it can be baked. Alternatively, there is the possibility to create a fast beam of H atoms.

Inspection of Figure 4 reveals the good agreement of our data with the low temperature prediction of the two theories (Sakimoto 1989; Cizek et al. 1998). They are both based on the same interaction potential from Senekowitsch et al. (1984) which is significantly more attractive than the polarization potential. A recent new calculation of the potential curve (Pichl 2005) agrees well and it is stated that further improvements have to account for correlation effects in the electron and proton motion. Sakimoto (1989) discussed convincingly the fact that at energies below 0.1 eV the rate coefficient for reaction (1) is determined just by a simple capture condition at large distances. During the succeeding approach of the two atoms, the probability to detach the electron is close to unity. From this point of view, our data may indicate that the potential is even more attractive at distances which are probed by 1 meV collisions (partial waves up to $l = 10$, turning point at distances larger than $10 a_0$).

For such conclusions, we have to reduce the uncertainties in the determination of absolute rate coefficients and in our temperature scale. This is possible by better characterizing the flux of the H-atom beam (see discussion by Borodi et al. 2009) and by characterizing the ion cloud using PD. The ions can be influenced by varying the effective potential and shifted with the correction electrodes. Cleaning the electrodes (stainless steel) always has some effect on potential distortions. Since a calibration reaction has a lot of advantages, it is also planned to establish the exothermic electron transfer from H to D^+ as one. Since this one-electron system is much better understood from first principles than the three-electron reaction (1), it is ideal for determining the effective H density. Also the reverse process, the 3.70 meV endothermic electron transfer from D to H^+ is well characterized by theory (Esry et al. 2000). The threshold onset is a critical test of the instrument.

A final remark has to be made regarding reaction (1). Measured absolute integral cross sections (or rate coefficients) are in general a critical test for theory; however, in the present case the outcome of the $H^- + H$ collision is rather insensitive to the actual AD process occurring at distances of a few a_0 . A more sensitive experiment is to observe the competition between electron transfer and AD in $H^- + D$ and $D^- + H$ collisions. Corresponding work is in progress. Most information on the details of the dynamics can be obtained by determining how the exothermicity of 3.724 eV is distributed among the degrees of freedom of the products, i.e., the kinetic energy of the electron and the rovibrational population of H_2 . The population of the rotational states is mainly determined by conservation of total angular momentum since only p -electrons are ejected. From this it can be concluded that, for example at a collision energy of a few meV (corresponding to $J_{MAX} \sim 20$), more than 1 eV goes into rotation of H_2 . The actual population of the vibrational states depends on the coupling in the collision complex. Interesting predictions already have been made by Cizek et al. (1998; see Figure 5). Such information is certainly also of importance for cooling early universe matter.

4. CONCLUSION AND OUTLOOK

Using the rf ion trapping technique and by exposing an H^- ion cloud to a cold effusive beam of hydrogen atoms, thermal rate coefficients for reaction (1) have been measured in a temperature range so far unexplored. The temperature dependence is in

accordance with simple theoretical predictions based on capture via the long-range attraction. In the overlapping energy range, there is good agreement with the merged beams results reported by Kreckel et al. (2010), Bruhns et al. (2010), and Miller et al. (2011). Due to our rather large systematic uncertainty, caused by the calibration reaction, our present results cannot solve the discrepancy between merged beams and flow tube results at 300 K (Martinez et al. 2009). Improving the accuracy of our instrument and going to higher temperatures will solve this problem. Work is in progress to use the electron transfer in $D^+ + H$ collisions as calibration standard.

The versatile instrument opens up new possibilities to study reactions which are of interest for early universe chemistry or which are of central importance for testing fundamental theories. The need to determine state specific rate coefficients for HeH^+ ($v = 0, j$) + H, which was mentioned in Section 1. Radiative association of two atoms, especially with H, is an experimental challenge. With today's technologies, it should be possible to detect HeH^+ from $H^+ + He$. Storing H^- and operating the beam source with deuterium will allow us to study the competition between electron transfer and AD in $H^- + D$. Also mutual neutralization of H^- and H^+ can be studied in a trap since the effective potential is proportional to the square of the charge, i.e., the rf field confines simultaneously positive and negative ions.

A challenge for theoretical predictions for reaction (1) is an experiment which can determine the kinetic energy of the detached electrons and which provides information on the rovibrational population of the H_2 product. Simulations show that one can superimpose an rf field and a suitable magnetic field such that electrons are guided out of the trap and that one can detect them. Moreover, the integration of an electron spectrometer using magnetic adiabatic collimation should be possible. Corresponding work is in progress.

The AB-22PT instrument has been developed in Chemnitz with contributions from S. Schlemmer, G. Borodi, and A. Luca and the help from many other people. Financial support of the Deutsche Forschungsgemeinschaft (DFG) via the Forschergruppe FOR 388 "Laboratory Astrophysics" is gratefully acknowledged. Since 2010 the instrument has been operated in the Faculty of Mathematics and Physics of the Charles University in Prague, also within the COST Action CM0805 (The Chemical Cosmos). We thank the Chemnitz University of Technology and the DFG for making this transfer possible. This work is a part of the research plan MSM 0021620834 and grant OC10046 financed by the Ministry of Education of the Czech Republic. It was also partly supported by GACR (202/07/0495, P209/12/0233, 205/09/1183, 202/09/0642) and by GAUK 25709, GAUK 406011, GAUK 388811.

REFERENCES

- Borodi, G. 2008, PhD thesis, TU Chemnitz, <http://nbn-resolving.de/urn:nbn:de:bsz:chl-200900932>
- Borodi, G., Luca, A., & Gerlich, D. 2009, *Int. J. Mass Spectrom.*, **280**, 218
- Bovino, S., Tacconi, M., Gianturco, F. A., & Galli, D. 2011, *A&A*, **529**, A140
- Bruhns, H., Kreckel, H., Miller, K. A., Urbain, X., & Savin, D. W. 2010, *Phys. Rev. A*, **82**, 042708-1
- Cizek, M., Horacek, J., & Domcke, W. 1998, *J. Phys. B: At. Mol. Opt. Phys.*, **31**, 2571
- Esry, B. D., Sadehpour, H. R., Wells, E., & Ben-Itzhak, I. 2000, *J. Phys. B: At. Mol. Opt. Phys.*, **33**, 5329
- Fehsenfeld, F. C., Howard, C. J., & Ferguson, E. E. 1973, *J. Chem. Phys.*, **58**, 5841
- Gerlich, D. 1992, *Adv. Chem. Phys.*, **82**, 1

- Gerlich, D. 2008a, in *Low Temperatures and Cold Molecules*, ed. I. W. M. Smith (Singapore: Imperial College Press), 121
- Gerlich, D. 2008b, in *Low Temperatures and Cold Molecules*, ed. I. W. M. Smith (Singapore: Imperial College Press), 295
- Gerlich, D., & Borodi, G. 2009, *Faraday Discuss.*, **142**, 57
- Gerlich, D., Borodi, G., Luca, A., Mogo, C., & Smith, M. 2011, *Z. Phys. Chem.*, **252**, 475
- Glover, S., & Abel, T. 2008, *MNRAS*, **388**, 1627
- Glover, S., Savin, D. W., & Jappsen, A.-K. 2006, *ApJ*, **640**, 553
- Jambrina, P. G., Alvarino, J. M., Gerlich, D., et al. 2012, *Phys. Chem. Chem. Phys.*, **14**(10), 3346
- Kreckel, H., Bruhns, H., Čížek, M., et al. 2010, *Science*, **329**, 69
- Launay, J. M., Le Dourneuf, M., & Zeippen, J. 1991, *A&A*, **252**, 842
- Lepp, S., Stancil, P. C., & Dalgarno, A. 2002, *J. Phys. B: At. Mol. Opt. Phys.*, **35**, R57
- Martinez, O., Yang, Z., Betts, N. B., Snow, T. P., & Bierbaum, V. M. 2009, *ApJ*, **705**, L172
- Miller, K. A., Bruhns, H., Eliasek, J., et al. 2011, *Phys. Rev. A*, **84**, 052709
- Otto, R., Hlavenka, P., Trippel, S., et al. 2009, *J. Phys. B: At. Mol. Opt. Phys.*, **42**, 154007-1
- Pichl, L. 2005, *Czech. J. Phys.*, **55**, 167
- Plasil, R., Mehner, T., Dohnal, P., et al. 2011, *ApJ*, **737**, 60
- Puy, D., & Signore, M. 2007, *New Astron.*, **51**, 411
- Ross, T., Baker, E., Snow, T. P., et al. 2008, *ApJ*, **684**, 358
- Sakimoto, K. 1989, *Chem. Phys. Lett.*, **164**, 294
- Schmeltekopf, A. L., Fehsenfeld, F. C., & Ferguson, E. E. 1967, *ApJ*, **118**, L155
- Senekowitsch, J., Rosmus, P., Domcke, W., & Werner, H.-J. 1984, *Chem. Phys. Lett.*, **111**, 211

ARTICLE II

TITLE: Determining the energy distribution of electrons produced in associative detachment: The Electron Spectrometer with Multipole Trap

AUTHORS: Pavol Jusko, Štěpán Roučka, Radek Plašil, and Juraj Glosík

JOURNAL: International Journal of Mass Spectrometry

DATE: Submitted 28. May 2013

Determining the energy distribution of electrons produced in associative detachment: The Electron Spectrometer with Multipole Trap

P. Jusko^a, Š. Roučka^{a,*}, R. Plašil^a, J. Glosík^a

^a Charles University in Prague, Faculty of Mathematics and Physics, Department of Surface and Plasma Science, V Holešovičkách 2, 18000, Prague, Czech Republic

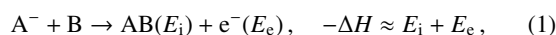
Abstract

Design of a novel instrument for the analysis of the kinetic energy of the detached electrons is presented. The Electron Spectrometer with Multipole Trap combines a radiofrequency ion trap with a magnetic adiabatic collimation filter and is capable of measuring the energy of electrons produced in the trap. The theory of operation and numerical simulations of the instrument are presented together with a proof of concept measurements using three different mechanisms of electron production – thermionic emission from a tungsten filament; laser photodetachment from O⁻ anions; associative detachment of O⁻ + H₂, D₂, and CO.

Keywords: associative detachment, multipole trap, electron energy spectrum, reaction rate coefficient

1. Introduction

The associative detachment (AD) is an anion-neutral reaction which can be formally described as



where E_i is the energy of the internal excitation of the molecule and E_e is the kinetic energy of the electron. Thanks to the high mass of the molecule compared to the electron, the kinetic energy of the produced molecule can be neglected. The reaction proceeds via a compound state AB^- , which decays by autodetachment. The redistribution of the internal energy of AB^- between E_i and E_e is – within the kinematic constraints – determined by the internal structure of the AB^- complex [1, 2].

The aim of this work is to study the dynamics of the associative detachment by measuring the energy distribution of the produced electrons. The reactions of O⁻ with H₂ (theoretical description [3, 4, 5])



their isotopic variants with D₂, and the reaction of O⁻ with CO



are used in this work as a model systems to demonstrate the capabilities of the presented experimental setup. The exothermicities of the reactions with H₂ are given by Claydon et al. [3] and the exothermicity of the reaction with CO by Abouaf et al.

[6]. The uncertainty of these values is smaller than 0.1 eV. The product energy distributions of reactions (2) and (3) have been studied by Mauer and Schulz [7] and partly by Esaulov et al. [8] with contradicting results. Furthermore, strong unexpected isotopic effects have been observed in the product energy distribution of reaction (3) with H₂/D₂ as reactants [9]. Therefore we aim to search for possible isotopic effects in the H₂O⁻/D₂O⁻ collision system. It has also been demonstrated by Zivanov et al. [10] that the measurements of the energy of the detached electrons are a useful tool for benchmarking of the theoretical description of the AD process.

The importance of AD reaction studies especially in the field of astrophysics has been emphasized recently by Glover et al. [11]. Since then several experimental setups were used to measure the AD reaction rate coefficient [12, 13, 14] exclusively.

For the purpose of studying the AD reactions, we have developed a novel experimental technique, which is capable of measuring the energy distribution of electrons produced in the AD reaction of ions stored in an ion trap. The subject of this article is the description of the *Electron Spectrometer with Multipole Trap* (ES-MPT) instrument. Computer models, experimental characterization, calibration, and selected experimental results will be presented.

2. Radiofrequency ion trap with MAC-E filter

The ES-MPT is a combination of an electron spectrometer with an rf ion trap. These two devices are combined in such a way that the ion trap is located inside the input region of the electron spectrometer (see schematic diagram in Fig. 1).

Thanks to the high mass ratio and different energies of the anions and electrons, we can choose such operating conditions that the anions are governed mainly by the rf field of the trap

*Corresponding author. Tel.: +420 22191 2344
Email address: Stepan.Roucka@mff.cuni.cz (Š. Roučka)

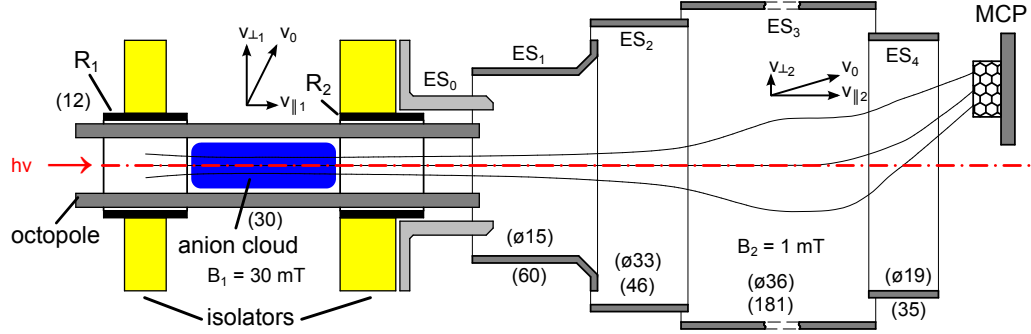


Figure 1: Schematic diagram of the ES-MPT apparatus (not to scale). The principle of combination of the radiofrequency ion trap (octopole on the left side) and the MAC-E filter (right side). Anions are injected into the octopole trap from the left and confined axially using the electrostatic ring electrodes (R_1, R_2). Laser radiation can be applied along the axis, reactant gas can be introduced into the trap between R_1, R_2 . Produced electrons are magnetically guided to the region with lower magnetic field (B_2) and refocused to the MCP detector. Cylindrical electrodes ES0–ES4 create the electrostatic barrier (diameter and length in parentheses are in mm).

and the produced electrons mainly by the magnetic field of the electron spectrometer.

Although the rf ion traps in magnetic field have been used in experiments such as Fourier transform mass spectrometers [15], magneto-optical traps [16], and photoelectron spectrometers [17] before, we believe that our instrument is unique in its ability to extract and analyze the electrons produced in the rf ion trap.

2.1. MAC-E filter

One of the principal components of the ES-MPT setup is the MAC-E filter – *Magnetic Adiabatic Collimation combined with an Electrostatic filter*. This device guides the produced electrons using magnetic field and filters them according to their energy with good resolution regardless of their initial velocity direction. This type of instrument was first described by Beamsom et al. [18] and is used in many particle physics experiments [19], where the produced electrons have random initial velocity direction. In such cases, filtering of the electrons by a retarding potential barrier is not directly applicable, because the barrier measures only the randomly distributed projection of the velocity parallel to the electric field.

The principle lies in the adiabatic invariance of magnetic moment μ of electrons with mass m_e :

$$\mu = \frac{1}{2} \frac{m_e v_{\perp}^2}{B} = \frac{E_{\perp}}{B}, \quad (5)$$

where B is the magnitude of the magnetic field, v_{\perp} is the projection of the particle velocity perpendicular to the magnetic field vector and E_{\perp} is the kinetic energy associated with the perpendicular motion. The magnetic field configuration of the MAC-E filter consists of two regions with magnetic field intensities $B_1 \gg B_2$. We will denote these regions as strong- B and weak- B in the text. The electrons are produced in the strong- B region (B_1) and guided along the magnetic field lines into the weak- B region (B_2). Thanks to the conservation of magnetic moment μ , the initial energy of the perpendicular motion $E_{\perp 1}$ is reduced to

$$E_{\perp 2} = E_{\perp 1} \frac{B_2}{B_1} \quad (6)$$

in the weak- B region and because of the energy conservation, the energy of the perpendicular motion E_{\perp} must be transformed into the energy of motion parallel to the magnetic field (E_{\parallel} , associated with parallel velocity v_{\parallel}). The electron velocities become collimated and their energies can be analysed simply by placing a variable retarding potential barrier into the weak- B region.

Assume that an electron with charge q_e is produced in the strong- B region with velocity v_0 , energy E_0 , and velocity projection parallel to magnetic field $v_{\parallel 1}$ (Fig. 1). To pass through the potential barrier $E_B = q_e U_B$ in the weak- B region, the energy of the parallel motion must satisfy $E_{\parallel 2} > E_B$ (we set the reference zero potential in the center of the trapping area). This condition can be rewritten in terms of the initial values using eq. (6) and the law of energy conservation:

$$\frac{v_{\parallel 1}}{v_0} > \sqrt{1 - \left(1 - \frac{E_B}{E_0}\right) \frac{B_1}{B_2}}. \quad (7)$$

The response of the MAC-E filter to a monoenergetic isotropic source of electrons is calculated analytically below in order to understand the transmission properties of the MAC-E filter relevant for our experiment. In this case, the probability distribution of the velocity component $v_{\parallel 1}$ is uniform in the interval $[-v_0, v_0]$. Therefore, the fraction of particles satisfying (7) is simply calculated as

$$P_T \left(\frac{E_B}{E_0} \right) = \frac{1}{2} \left(1 - \sqrt{1 - \left(1 - \frac{E_B}{E_0}\right) \frac{B_1}{B_2}} \right). \quad (8)$$

The factor 1/2 accounts for the particles initially receding from the spectrometer. We neglect it in the further discussion, since these particles can be reflected back to the spectrometer by placing a high electrostatic barrier on their escape path. Evaluating also the extreme cases leads to the transmission function of the spectrometer

$$P_T \left(\frac{E_B}{E_0} \right) = \begin{cases} 1 & \frac{E_B}{E_0} \leq 1 - \frac{B_2}{B_1} \\ 1 - \sqrt{1 - \left(1 - \frac{E_B}{E_0}\right) \frac{B_1}{B_2}} & 1 > \frac{E_B}{E_0} > 1 - \frac{B_2}{B_1} \\ 0 & \frac{E_B}{E_0} \geq 1. \end{cases} \quad (9)$$

The electron spectrum is obtained by differentiating the retarding curve. Hence the relative resolution ΔE of the filter can be calculated by differentiating the transmission curve for monoenergetic electrons (9). We define the relative resolution as the width of the support of the obtained peaks

$$\Delta E = E_0 \frac{B_2}{B_1}. \quad (10)$$

The expression (9) is also useful in estimating the efficiency of extracting the electrons from the ion trap. A small potential barrier $U_T \approx -0.3$ V, which is used to trap the anions, can prevent some electrons from leaving the trap. Since the magnetic field in the trap is nearly constant, we can evaluate the extraction probability P_E by setting $B_1/B_2 = 1$ in equation (9). Expressing the result in terms of the electron energy E_e and trapping potential U_T leads to

$$P_E(E_e, U_T) = 1 - \sqrt{\frac{q_e U_T}{E_e}} \quad (11)$$

for $E_e > q_e U_T$, otherwise the probability is zero.

2.2. Radiofrequency ion trap

The radiofrequency (rf) multipole traps are well understood and widely used for trapping of charged particles [20]. In this work a linear radiofrequency octopole is used to guide and trap the anions in the radial direction. In the axial direction, the ions are trapped by electrostatic barriers. To trap an anion of mass M and charge q , the rf field of an amplitude V_0 creating an effective potential V^* greater than the particle kinetic energy E is needed. In the adiabatic approximation [20], the effective potential of a linear multipole as a function of the reduced radius $\hat{r} = r/r_0$ is given by

$$V^*(\hat{r}) = \frac{n^2}{4} \frac{q^2}{M\Omega^2} \frac{V_0^2}{r_0^2} \hat{r}^{2n-2}, \quad (12)$$

where Ω is the rf field angular frequency, r_0 is the inscribed radius of the multipole (3 mm in our case), r is the radial coordinate, and $2n = 8$ is the number of rods for the octopole.

The minimal rf amplitude V_0 necessary for trapping of the ions is given by a requirement that the turning radius of the ions must be within a safe distance from the rods, typically smaller than $0.8 \cdot r_0$. That is, $V^*(0.8) \geq E$. Under the typical operating conditions in our experiments with trapped O^- anions, $\Omega/2\pi = 4.4$ MHz, $V_0 = 10$ V, and the effective potential at the safe turning radius is $V^*(0.8) = 0.05$ V. These conditions are just sufficient for trapping of thermal anions at 300 K and significant lowering of the rf amplitude is not possible at this frequency. The adiabatic theory is not applicable to the interaction of electrons with rf fields in our conditions. The residence time of electrons in the rf field is comparable to the rf period and no simple analytic description is available. Therefore we are using a computer model of the spectrometer described in section 3.1 to study this interaction.

In the particular case of the ES-MPT instrument, the ion trap is operated in magnetic field. The problem of ion motion in such combined fields has been studied theoretically [21, 22,

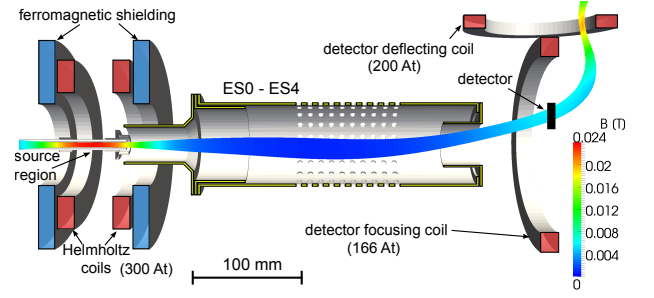


Figure 2: Configuration of the electrodes, coils, and ferromagnetic elements of the electron spectrometer. The calculated color-coded magnetic field intensity is projected on the calculated magnetic flux tube emanating from the ion trap. The flux tube approximately represents the possible electron trajectories. The number of ampere-turns (At) used for producing the magnetic field is indicated for each coil.

23, 24, 25]. In our experimental conditions, the magnetic field is relatively weak, i.e., the cyclotron frequency is much smaller than the rf frequency. We have verified by numerical simulations that in such cases the adiabatic theory and equation (12) remain valid. The experimental confirmation is presented in section 3.3.

3. Experimental methods

The ES-MPT (Fig. 1) is an UHV apparatus with background pressures $< 1 \cdot 10^{-7}$ Pa. The storage ion source, trapping area, and MAC-E filter vacuum vessels are each pumped by its respective magnetic suspension turbomolecular pump (total of 3).

The anion part of the apparatus consists of the anion source, quadrupole mass spectrometer, guiding octopole, and the trapping octopole area [26]. The O^- anions are produced in the storage ion source [20] by electron bombardment of the precursor gas (N_2O) and are mass selected in the quadrupole before injection into the trap.

The trapping area is enclosed in a scattering cell with a separate gas inlet system for introduction of a reactant gas. The octopole rods are 2 mm thick ($r_r = 1$ mm), spaced on a circle with 6 mm inner diameter ($r_0 = 3$ mm). The lowest usable rf amplitude for O^- is 10 V as discussed in section 2.2. The axial trapping barriers are created using ring electrodes R_1, R_2 located outside of the octopole (rings with inner radius 12 mm and length 10 mm). No cooling or heating of the reaction area is implemented, the experiments are conveyed at room temperature.

The apparatus is optically transparent along the axis of the octopole so that laser radiation can be used to photodetach the trapped anions. A microchannel plate (MCP) detector is used for detection of ions and electrons. The detector is located off axis in order to retain the optical transparency of our setup.

The strong- B region of the MAC-E filter is coincident with the ion trap location and the field is parallel to the trap axis in order to extract the produced electrons. The magnetic field for the MAC-E filter is produced with standard enamelled copper wire coils (4 in total) located outside of the vacuum chamber. Two

coils in approximately Helmholtz configuration are used to generate the strong magnetic field in the trapping area. These coils are surrounded by ferromagnetic steel rings, which enhance the gradient of the magnetic field between the strong- and weak- B regions, thus reducing the dimensions of the filter. The other two coils are used to focus and deflect the filtered electrons to the off-axis detector.

The suitable configuration of coils and ferromagnets was designed using computer simulations with the FEniCS software [27, 28] and verified by measurements with a Hall probe. The highest magnetic field intensity (in the trapping area) is $B_1 = 30$ mT, the lowest magnetic field in the electrostatic barrier region is $B_2 = 1$ mT. The theoretical resolution of the MAC-E filter is thus approximately 3 %.

All electrodes are made from austenitic (non-magnetic) stainless steel. The MAC-E filter parts were newly designed for this setup. The shape of the electrodes ES0–ES4 was optimized to provide an accurate potential barrier coincident with the minimum of the magnetic field intensity. The calculated inhomogeneity of the barrier is smaller than 1 %. The optimization was carried out using the Elmer software¹.

The measurement of electron spectrum proceeds by measuring the electron flux I_e (number of detected electrons per second) as a function of the electrostatic barrier height U_B . This way we directly measure the integral spectrum and the differential spectrum is obtained by numerical differentiation with smoothing using the Savitzky-Golay filter. Unless stated otherwise, the differential spectra are always normalized to unit area.

The ES-MPT is highly modular and several configurations have been used to obtain the results presented. These modifications are going to be described in the text when relevant.

A number of test measurements in different configurations were performed in order to properly understand the properties of this unique instrument and computer models of the instrument were used to analyse the results. The following subsections document these models and auxiliary measurements.

3.1. Computer model of the ES-MPT

A three dimensional computer model of the ES-MPT was used to verify our design and to explain the observed results. All parts of the instrument relevant for the electron dynamics are included in the model (i.e., the electric field of the octopole rf trap, the electrostatic filter electrodes, and the MCP detector and the magnetic field of the coils and ferromagnets). The model geometry is illustrated by Fig. 2. This model was used to investigate the influence of rf field imperfection in the trap on the measured electron spectrum. In our simulations, the initial positions of electrons are chosen randomly with a spatial distribution approximating the distribution of the trapped ions. The initial phase of the rf field is also randomized and the electron trajectories are obtained by numerically integrating the equations of motion. The number of electrons reaching the detector was then calculated as a function of the retarding potential U_B . Three different scenarios were studied in the model: 1) model

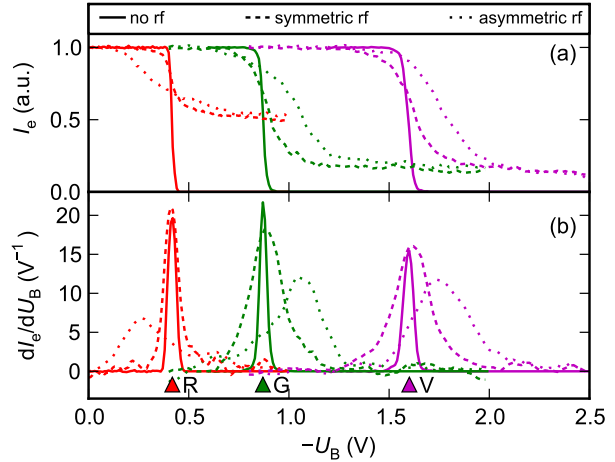


Figure 3: Simulated spectra of monoenergetic isotropically distributed electrons with energies corresponding to the photodetached electrons from O^- using 660 nm (R), 532 nm (G), and 405 nm (V) lasers (see Table 1). Panel (a) – Integral spectra of electrons normalized to unity at zero retarding barrier. Panel (b) – Differential spectra obtained by differentiation of the spectra in panel (a). The spectra calculated without rf field (full lines), with ideal symmetric rf field (dashed lines), and with non-ideal asymmetric rf field (dotted lines) are shown.

without rf trapping field; 2) model with symmetric rf trapping field; 3) model with disturbed rf trapping field (20 % higher rf amplitude on one of the rods). The 20 % increase of the amplitude approximates the effect of moving the rod by 0.2 mm towards the octopole axis, which is plausible in our configuration. The simulated differential and integral spectra are shown in Fig. 3. The results of the model support our hypothesis that the resolution of the ES-MPT apparatus is limited due to the interaction of electrons with the rf field of the octopole ion trap. The model also demonstrates that imperfections of the rf field penetrating into the trap center can lead to shifting of the observed peaks on the energy scale – the stray rf field in the trap accelerates the produced electrons.

3.2. Thermionic emission as electron source

In order to analyze the resolution of the MAC-E filter without the influence of the rf field, the electrons produced by thermionic emission were used. The anion producing part was disconnected and a thin tungsten filament was placed into the center of the octopole (radially and axially with respect to the ring electrodes). The potential of the ring electrodes was set to 0 V with respect to the reference DC potential of the octopole rods.

The filament was heated by ohmic heating and the heating current was turned on and off with repetition frequency ≈ 100 Hz and duty ratio 0.5. We ensure by gating of the detector that the electrons are counted only in the phase with zero heating current. In this way the filament surface potential is well defined and can be biased to desired value without the influence of voltage drop due to the filament resistance.

The electrons emitted from the hot filament originate from the high-energy tail of the Fermi-Dirac distribution of electrons in the metal, which can be approximated by the Boltzmann dis-

¹URL: <http://www.csc.fi/english/pages/elmer>

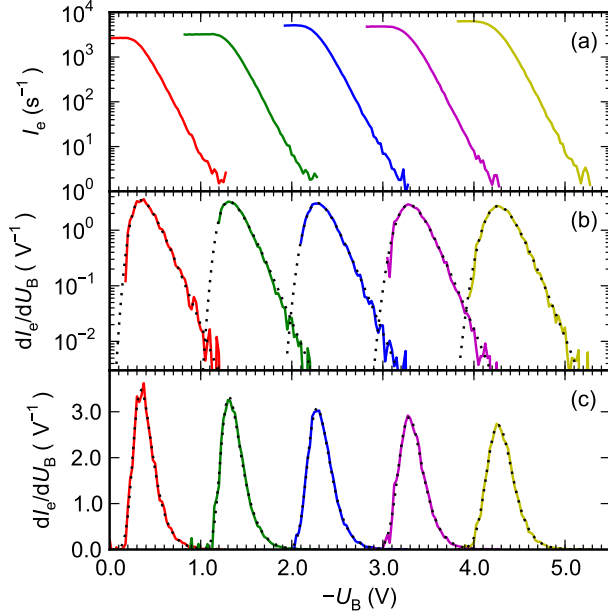


Figure 4: The measured spectra of electrons produced by thermionic emission from hot filament. Panel (a) – Integral recorded spectra. Panels (b), (c) – Differential spectra (normalized) obtained from the integral spectra in logarithmic and linear scales respectively. Cathode bias voltages -0.1 , -1.1 , -2.1 , -3.1 and -4.1 V were used to provide electrons of 5 different energy distributions (full lines). Fits of the theoretical spectrum (13) convolved with a gaussian function and offset by the bias voltage are indicated by the dotted lines.

tribution. The electron flux distribution is obtained by multiplying the Boltzmann velocity distribution with electron velocity component perpendicular to the metal surface. After integration over the angular coordinates this leads to the energy distribution of the emitted electrons

$$f(E_c) dE_c = (k_B T)^{-2} E_c \exp\left(-\frac{E_c}{k_B T}\right) dE_c, \quad (13)$$

where k_B is the Boltzmann constant and T is the filament temperature. The offset on energy scale of the measured spectrum is determined by the bias voltage applied to the filament and by the difference of work functions between the spectrometer electrodes and the filament. Several measurements were performed at different bias voltages with respect to the trap potential and the obtained integral and differential spectra are shown in Fig. 4. The differential spectra were analyzed by fitting with a convolution of the theoretical spectrum (13) and a gaussian function. The position μ , standard deviation σ , and temperature T were used as free parameters. We have determined that the work function of the filament is approximately 0.1 eV higher than the work function of the electrodes. The effective potential barrier is approximately 2 % higher than the applied electrode potential with respect to the octopole due to the filtering properties of the MAC-E filter in combination with the inhomogeneities of the electrostatic field, which is in agreement with our numerical calculations. The temperature of the filament is evaluated as

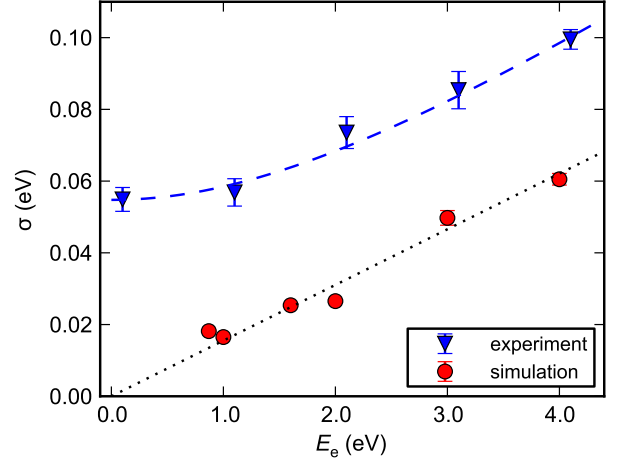


Figure 5: Resolution of the MAC-E filter as a function of electron energy. Triangles correspond to the resolution determined from the measurements with electrons from thermionic emission (see Fig. 4). Circles represent the computer simulation of the spectra (see Fig 3). The instrument function is approximated with a gaussian and its standard deviation σ is shown on the y-axis.

$T = (1080 \pm 40)$ K. The fitted standard deviation as a function of electron energy is shown in Fig. 5. The same analysis was also carried out on simulated data under equivalent conditions and the results are also shown in Fig 5. The figure demonstrates the broadening of the peaks at higher electron energies, which is also apparent in Fig. 4(c). This observation is in accordance with equation (10), since the MAC-E filter resolution is proportional to the energy. The broadening σ , which consists of a constant part σ_c and a proportional part $\sigma_p E_e$, can be expressed as $\sigma^2 = \sigma_c^2 + (\sigma_p E_e)^2$. The constant part is comparable to the expected variation of the work function on the filament surface (between 0.01 and 0.1 eV according to [29, 30]) and it is not relevant for our analysis. The proportional part determined by fitting of the experimental data is $\sigma_p = (2.0 \pm 0.1)$ % and it is compatible with value determined from the simulation $\sigma_p = (1.6 \pm 0.1)$ %. The measured value is of the same magnitude as the theoretical peak width $B_2/B_1 = 3.3$ % (equation (10)), although it is not directly comparable, because the peak is not gaussian and other effects such as potential inhomogeneity contribute to the experimental and simulated values.

The electrons from the thermionic emission can also be used to investigate the influence of the octopole rf field on the measured spectra. The distortion of the measured spectra for bias voltage -1.1 V and rf amplitude 10 V applied to the octopole is indicated in Fig. 6. The figure shows that the effect of the rf field on the undistorted spectrum can be approximated as a convolution with a sum of two gaussians – the instrument function. The parameters of the gaussians were determined by least squares fitting the convolved undistorted spectrum to the distorted spectrum. This effect of the rf field on the electrons from the filament is not directly comparable to the effect on electrons from the trapped anions, because the potential of the filament is well defined by the applied bias in contrast to the potential at which the electron is detached from the anion. The actual

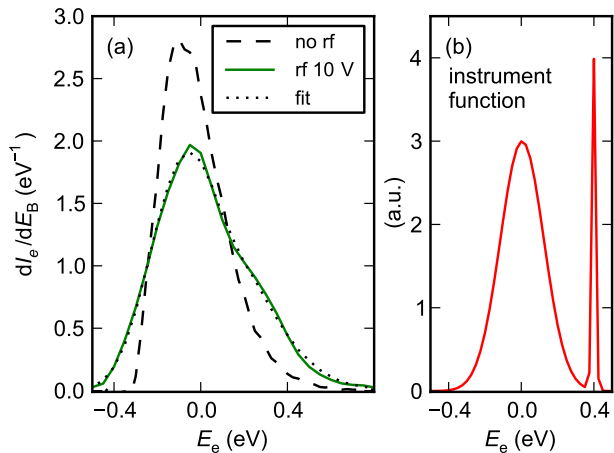


Figure 6: Influence of the rf field to the measured spectra of filament emitted electrons. Panel (a) – spectrum measured with and without rf field present (filament bias is -1.1 V, this corresponds to 0 eV energy on the abscissa). Panel (b) – instrument function which represents the effect of rf field on the undistorted spectrum.

position of the detaching anion in the rf field determines the potential. We deduce that the effects presented in Fig. 6 are caused by rf multipole field interacting with the electrons flying through the octopole after leaving the filament surface.

3.3. Anion photodetachment

For further tests with trapped O^- anions, the MCP detector was placed closer to the trap replacing the ES2 electrode in order to allow simultaneous detection of ions (focused by electrostatic fields) and electrons (focused by magnetic fields directly to the detector without collimation). The experiment was operated in two distinct modes:

1) The ions were repeatedly injected into the trap, stored for a certain trapping time, then extracted to the detector and counted. In this mode the detector was gated in order to detect only the ions after the trap opening. A similar technique was previously used by Hlavenka et al. [31] to measure absolute photodetachment cross sections of O^- and OH^- anions.

2) A long fixed trapping time was used and the detector gate was open continuously between the ion injection and extraction. In this mode, the electrons produced in the trap were detected and their arrival times were recorded using a multi-channel scaler.

In this configuration, in mode 1), we have verified that the presence of the magnetic field of the spectrometer does not influence the confinement time τ (the time constant of the ion loss from the trap). The confinement time in our experiment is limited by reactions with background gas and by eventual evaporation of anions due to the rf heating. For numerical simulations of the latter phenomena see Asvany and Schlemmer [32].

Irradiating the trap with laser with photon energy ($h\nu$) higher than the electron affinity E_A of the atomic oxygen causes photodetachment

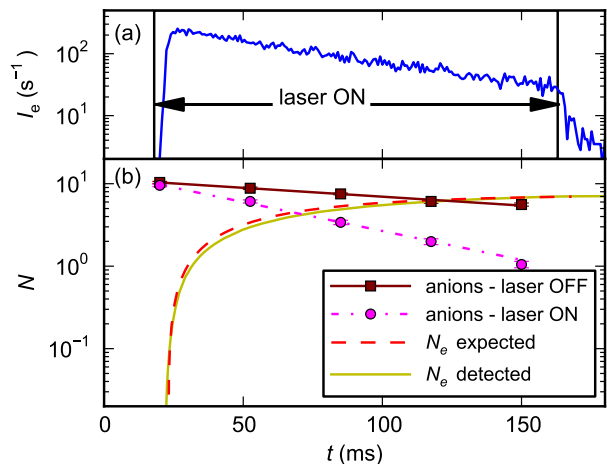
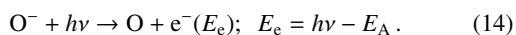


Figure 7: Number of detected electrons and O^- anions as a function of storage time (t) during a pulsed laser photodetachment experiment (using red laser, see Table 1). Panel (a) – the measured electron production rate with the laser pulse ON. The duration of the laser pulse is indicated. Panel (b) – squares and circles indicate the number of O^- with the laser pulse OFF and ON respectively. Exponential fits of the ions counts are also indicated. The dashed line shows the expected number of produced electrons calculated from the fits. The expected number is in good agreement with the measured number (solid line) obtained by integrating the electron production rate corrected for the differences in electron and ion detection efficiencies.

color	λ (nm)	$h\nu$ (eV)	E_e (eV)
red	660	1.88	0.42
green	532	2.33	0.87
blue	445	2.79	1.33
violet	405	3.06	1.60

Table 1: Overview of the laser wavelengths and corresponding photon energies used in the photodetachment experiments. The right column shows the energy E_e of electrons produced by photodetachment of O^- . The electron affinity of O is $E_A = 1.4610$ eV [33].

The loss of ions due to photodetachment was observed in the mode 1) of our measurement. In the mode 2) we were able to detect the photodetached electrons under the same conditions. The results of these measurements with a pulsed laser beam with 660 nm wavelength are summarized in Fig. 7. The laser wavelengths and photon energies used in this work and corresponding energies of the photodetached electrons are summarized in Table 1. The Fig. 7 clearly indicates the increased rate of electron production related to the laser pulse. Order of magnitude smaller flux of electrons is observed even after the laser is switched off. This is caused by trapping of a fraction of the photodetached electrons in the ion trap as explained in section 2.1. These electrons reside in the trap until their velocity is sufficiently disturbed by the rf field and they leave the trap towards the detector or to the octopole rods.

In Fig. 7 we compare the measured total number of produced electrons (integral of the electron flux in time) and the expected number of electrons calculated from the decrease of

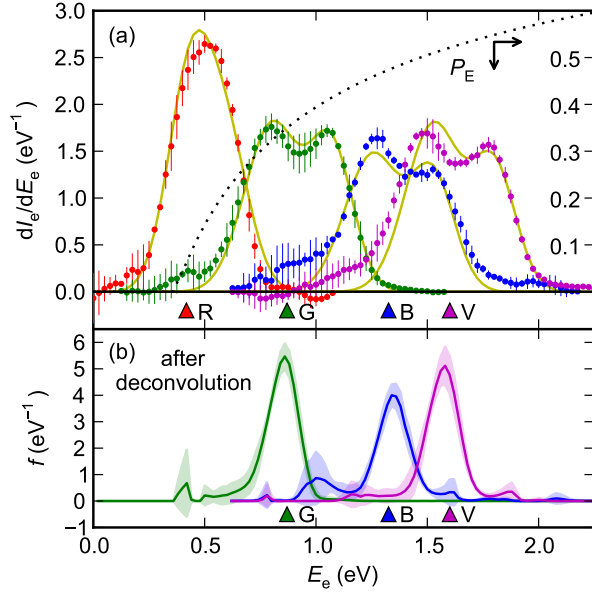


Figure 8: Measured spectra of electrons photodetached from O^- anions. Photon wavelengths used are 660 nm (R), 532 nm (G), 445 nm (B) and 405 nm (V) (see Table 1). Panel (a) – points correspond to measured data with wavelengths red, green, blue, and violet respectively (from left). Triangles indicate the expected electron energies according to Table 1. The smooth full lines represents the fitted convolution of the theoretical spectrum with the instrument function (equation (15)). The right axis corresponds to the extraction probability $P_E(U_T)$ (dotted line), where the trapping potential U_T is determined from the fit. Panel (b) – the spectra obtained from the measured data after deconvolution with the instrument function.

the number of O^- anions as a function of storage time. The lines are in a remarkably good agreement after introducing normalization due to different overall detection efficiency for electrons and O^- anions.

3.4. Spectra of the photodetached electrons

The spectra of photodetached electrons were measured in the full ES-MPT setup (Fig. 1). The integral spectra are obtained by measuring the electron count rate on the detector as a function of the retarding potential U_B . The laser is switched on after filling the trap with approximately 20 ms time delay, during which the ions are cooled by collisions with the helium buffer gas. The spectra of photodetached electrons were measured with four lasers, the wavelengths and corresponding electron energies are summarized in Table 1. The differential spectra obtained with the Savitzky-Golay smoothing filter are plotted in Fig. 8. The standard deviation of the measured data is indicated by the error bars.

A similar experiment was carried out also with a mixture of H_2 and He in the trap. In this case, only the violet (405 nm) laser was used. The number of Langevin collisions between O^- and H_2 before switching on the laser was varied by changing the H_2 concentration in the trap and the delay of the laser pulse after trap filling. The obtained spectra are shown in Fig. 9. Depending on the average number of Langevin collisions between O^- and H_2 before switching on the laser, we can observe

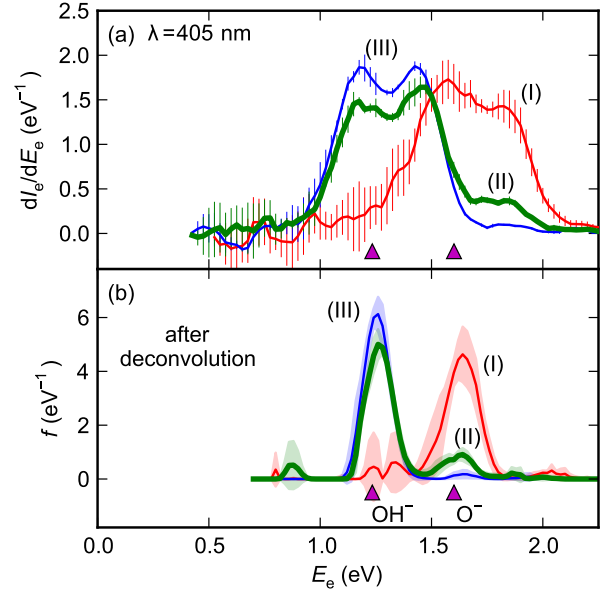


Figure 9: Panel (a) – measured spectra of the photodetached electrons from O^- and OH^- using the violet laser. The trapped O^- ions interact with H_2 in the trap. The average number of Langevin collision of O^- with H_2 before the laser is switched ON is 0, 2, and 7 for the curves (I), (II), and (III) respectively. The peaks in the spectrum, obtained from the measured data after deconvolution, can be attributed to the electrons produced from OH^- and O^- (panel (b)). The expected positions of the peaks are indicated by the triangles.

two peaks with varying intensities in the spectra. These peaks can be attributed to the electrons produced by photodetachment of O^- and OH^- , the anion product of the reaction (3). The peak positions are in good agreement with the electron energies expected from the O and OH electron affinities [33].

3.5. Analysis of the instrument function

Based on the test measurements described in the previous paragraphs, we can deduce a complete description of the transmission properties of our instrument. It follows from the measurements with the hot filament that the relative resolution of the electron spectrometer is in approximate agreement with the designed resolution of $\approx 3\%$ (see Fig. 5). The interaction of electrons with the rf field of the trap causes a splitting of the peaks in the observed spectrum (see Fig. 6). A qualitatively same behavior is observed in the measurements with electrons produced by laser photodetachment of O^- . The absence of splitting in the low energy region (red laser photodetachment in Fig. 8) indicates that the splitting occurs inside the trap and one of the peaks is filtered by the trap potential barrier (11). The energy of the electrons is then further disturbed during the ejection from the octopole, because the onset of the spectrum at the low energy does not follow the steep shape of function (11). We have found that the spreading of the spectrum is well approximated by a gaussian functions. Therefore we can describe the instrument effect as a convolution with two gaussians $\mathcal{N}(\mu_1, \sigma_1)$, $\mathcal{N}(\mu_2, \sigma_2)$; followed by multiplication with the extraction probability P_E (equation 11) followed by convolution

with another gaussian $\mathcal{N}(0, \sigma_3)$. This operator is parametrized by the positions μ and standard deviations σ of the gaussians, by the relative intensity of the gaussians r , and by the trapping potential U_T . The measured electron energy distribution f' is obtained from the initial energy distribution f by the following transformation

$$f' = (P_E(U_T) \cdot [f * \{r \cdot \mathcal{N}(\mu_1, \sigma_1) + (1-r) \cdot \mathcal{N}(\mu_2, \sigma_2)\}]) * \mathcal{N}(0, \sigma_3), \quad (15)$$

where $*$ denotes convolution. The seven parameters of this transformation were determined by least squares fitting of the laser photodetachment spectra. The theoretical spectrum consisting of delta functions at the expected energies of photodetached electrons was transformed by function (15). A good fit of the measured data was obtained as shown in Fig. 8. The extraction probability P_E corresponding to the fitted value of the trapping potential U_T is also indicated in the graph. Figures 8 and 9 demonstrate that deconvolving the data with the transmission function can be used to significantly improve the resolution of the measured spectra.

4. Results

The ES-MPT apparatus is primarily designed to study the energy distribution of the electrons produced from the associative detachment reaction. It can also be used to measure the reaction rate coefficients as will be demonstrated below. The reactions were studied by adding a mixture of helium buffer gas with the reactant into the scattering cell. The typical ratio of the reactant to the buffer gas number densities was $[\text{H}_2]/[\text{He}] \approx [\text{D}_2]/[\text{He}] \approx [\text{CO}]/[\text{He}] \approx 1/3$.

4.1. Reaction rate coefficient

The electron production rate dN_e/dt in the presence of a reactant gas is proportional to the number of ions in the trap and to the number density of the reactant. For example in the case of trapping N_O of O^- ions in the trap with reactant H_2 (concentration $[\text{H}_2]$), we can write

$$I_e = s \frac{dN_e}{dt} = sk_1[\text{H}_2]N_O, \quad (16)$$

where I_e is the number of detected electrons per unit time (electron flux) and s the detection efficiency of our instrument for electrons. The detection efficiency is constant for a given electron energy distribution. Therefore we can observe the disappearance of O^- after filling the trap by recording the electron flux using the multichannel scaler. Examples of the measured I_e are shown in Fig. 10. In this measurement the retarding potential U_B is set to zero.

When the reactant gas is not present in the trap, the number of ions in the trap as a function of time can be probed using short laser pulses (≈ 10 ms). The number of observed photodetached electrons is proportional to the number of ions in the trap. The results of these measurements are shown in Fig. 10.

The number density of the reactant is estimated from the geometrical configuration, pumping speed and ion gauge pressure measurement. Our estimates account for the differences in

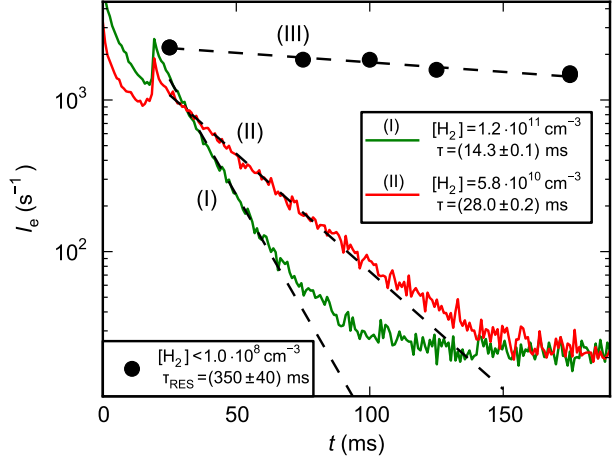


Figure 10: Measured electron production rate in reaction (2) as a function of trapping time measured at two H_2 number densities (full lines (I) and (II)). The trap is filled with O^- at $t = 0$ ms. At $t = 20$ ms, the axial trapping barrier is lowered to allow the low energy electrons to escape. The circles indicate a data proportional to the number of trapped ions without added H_2 . The number of ions is probed by illuminating the ions with short laser pulses and detecting the photodetached electrons. Dashed lines correspond to exponential decay fits in form $\exp(-t/\tau)$, obtained τ at given $[\text{H}_2]$ are indicated (τ_{RES} corresponds to confinement time without added reactant).

the ion gauge sensitivities and vacuum conductivities between different gases. The calculated total reaction rate coefficients $k = k_1 + k_2$ for reactions of $\text{O}^- + \text{H}_2$ and $\text{O}^- + \text{D}_2$ are compared with the previous measurement [34] in Table 2. Despite of the

Reaction	k (this work) ($10^{-10} \text{ cm}^3 \text{ s}^{-1}$)	k (McFarland et al. [34]) ($10^{-10} \text{ cm}^3 \text{ s}^{-1}$)
$\text{O}^- + \text{H}_2$	5.4 ± 0.2	6.4
$\text{O}^- + \text{D}_2$	3.2 ± 0.1	4.6

Table 2: Total reaction rate coefficient estimated from temporal evolutions of electron production at 300 K (see Fig. 10). Only the statistical error is shown. The results are accurate within a factor of 2 due to systematic errors.

good agreement with the results of McFarland et al. [34], we estimate that the error of the calculated number density could be up to a factor of 2 because of the simplifications in the geometric model of the instrument and because of the limited accuracy of the ionization pressure gauge. However, the geometric factors cancel if we calculate the ratio of the isotopic variants of the reaction coefficients $k(\text{H}_2)/k(\text{D}_2) = 1.7 \pm 0.1$, where only the statistical error is given. This value is slightly higher than the isotopic effect observed by McFarland et al. [34], $k(\text{H}_2)/k(\text{D}_2) = 1.4$.

4.2. Energy distribution of detached electrons

The technique of acquiring the energy distribution of electrons from the associative detachment reaction is the same as for the photodetached electrons. The difference is that the electrons are produced continuously. The electrons are selected by gating of the detector, so that only the electrons produced from

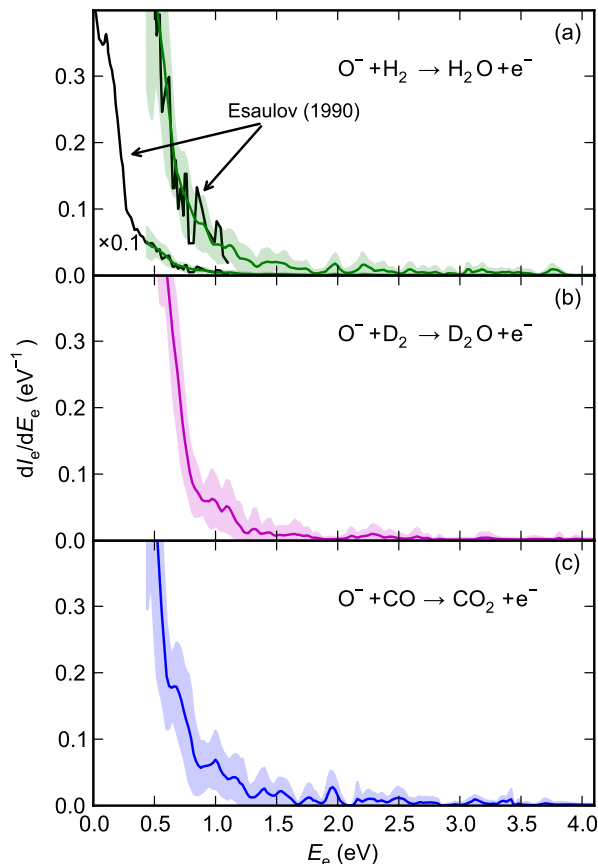


Figure 11: Measured electron energy spectra in the reactions of $\text{O}^- + \text{H}_2$, D_2 and CO (solid lines in panels (a), (b), and (c) respectively). The data of Esaulov et al. [8] are shown for comparison and are used to normalize the spectra. The standard deviation of multiple measurements is indicated in the graph. At electron energies above 1.5 eV, the signal intensity is below the noise level and the results should be interpreted as an upper bound of the actual probability.

cold O^- (thermalized by collisions with He buffer gas) are accounted.

Fig. 11 shows the measured electron energy distributions for the associative detachment reactions of O^- with H_2 , D_2 , and CO . The energy distributions have been investigated up to the maximum energy allowed by the reaction exothermicity, which was given in section 1. The differential spectra were obtained by differentiating and smoothing the integral spectra using the Savitzky-Golay filter with the same parameters as the photodetachment spectra in Figs. 8 and 9. The differential spectra were deconvolved with the gaussian kernel $\mathcal{N}(0, \sigma_3)$ using the Lucy Richardson algorithm [35, 36] with a constraint on the positive value of the data and then divided by the extraction probability P_E (equation (11)). The data measured by Esaulov et al. [8] are used as a reference for the normalization of our data with H_2 reactant. The same normalization factor was then used for the data measured with D_2 and CO reactants, assuming a similar behavior in the inaccessible low-energy part of the spectrum. For the AD with H_2 , there is a good agreement between our re-

sults and the spectra obtained by Esaulov et al. [8] in the overlapping region, despite the fact that his measurement was carried out at 1 eV collision energy. The measured spectra of electrons from the three studied reactions show similar features – we can conclude that the excess energy of the reactions is stored mainly in the internal excitation of the produced molecule. In Fig. 11 one can observe that there is no significant structure in the electron spectrum at energies above approximately 1.5 eV.

5. Discussion and summary

We presented a viable concept of an electron spectrometer for investigation of the associative detachment reactions. Despite the use of a low-order multipole, which reduces the resolution of the spectrometer, the accuracy is sufficient to characterise the produced electrons. The measurements of the reaction rate coefficients are also possible.

5.1. ES-MPT properties

Our measurements with the electrons produced by thermionic emission (Fig. 4 and 5) demonstrate that the properties of the spectrometer itself are in accordance with the design. The measurements with electrons produced by thermionic emission and by photodetachment with applied rf trapping field indicate that the rf field influences the electrons and causes splitting of initially monoenergetic electron energy distribution (Fig. 6 and 8). According to our numerical models (Fig. 3), such effects are not expected in the rf field of an ideal octopole. However, slight asymmetry of the rf field results shifts of the simulated energy distribution. We deduce that such asymmetry is present in a certain part of the trap, which results splitting of the electron energy distribution depending on the location of origin of the electrons. The observed effect can be attributed to a misalignment of the octopole rods on the order of 100 μm , which is conceivable in our design.

Nevertheless, the resolution of the instrument is sufficient to obtain the general characteristics of the energy distribution of electrons produced from the associative detachment reaction as demonstrated in section 4.2. We have also demonstrated that we are able to resolve the composition of the trapped anions by measuring the spectra of the photodetached electrons (Fig. 9).

Since further lowering of the rf amplitude V_0 is not possible because of the requirements on the effective potential for trapping of the anions, the best way to improve the spectrometer resolution is to use a higher order multipole. The field decreases much faster towards the axis thus eliminating the variances in V_0 . Furthermore, the construction of higher order multipoles, such as the 22-pole used in our laboratory [14], allows more accurate alignment of the rods, thus further reducing the possible influence of the rf field asymmetry. On the other hand, constructing a 22-pole trap with the electron spectrometer will be much more complicated compared to the present experiment due to the size of the 22-pole construction, which has to fit into the entrance region of the MAC-E filter.

The spectrometer low energy threshold can in principle be improved by cooling the trap. If the O^- anions have lower temperature, their kinetic energy is also lowered. Hence, a smaller axial barrier would be needed to confine them.

5.2. O^- associative detachment

We have demonstrated that the ES-MPT instrument is capable of measuring the absolute reaction rate coefficients. We have measured the ratio of the rate coefficients between the isotopic variants of the reaction O^- with H_2 and D_2 to be slightly higher than the result of McFarland et al. [34]. The accuracy of these measurements can be improved by accurate determination of reactant number density in the trap using an absolute pressure gauge.

The spectra of electrons produced from the AD of O^- with H_2 , D_2 , and CO were measured at 300 K. In case of the reaction with H_2 , our results agree with the results of Esaulov et al. [8], providing a supporting evidence in favor of Esaulov et al. against the results of Mauer et al. [7]. To our knowledge, the spectra for the reaction with D_2 and CO were not measured in the corresponding energy range up to now.

Our results indicate that for the studied AD reactions, the excess energy is stored mainly in the internal excitation of the molecule. There are two mechanisms responsible for this result. Firstly, a high rotational excitation is expected due to simple kinematic constraints – a collision system with nonzero impact parameter has nonzero angular momentum and this angular momentum is stored mainly in the molecular rotation because of the low mass of the ejected electron. Higher rotational excitation is statistically favored [2, 10] up to a certain J_m , which is limited by the energy conservation and by the corresponding centrifugal barrier. Secondly, the vibrational product distribution depends on the coupling between the bound and continuum states of the detaching electron. If this coupling is strong and the electron detaches early during the interaction at higher internuclear separation, the product will have high vibrational excitation according to the Franck-Condon principle [2, 10, 9].

6. Conclusion

A reliable technique for detection and energy analysis of electrons produced in an ion trap has been presented. This technique is ideally suited for studying of associative detachment reactions. In contrast to previous experimental setups measuring the energy of the detached electrons, the ES-MPT uses cold trapped anions and allows the use of beams (e.g., atomic H) not only molecular gas as a neutral reactant in the associative detachment. With small improvements also temperature dependence of the measured spectra can be investigated.

The deduction from the study of all three associative detachment processes is that molecules produced by associative detachment are highly internally excited and only small part of total energy is stored in the kinetic energy of the electron.

Acknowledgements

The storage ion source, quadrupole and guiding octopole have been developed in the group of prof. Dieter Gerlich at the Technical University in Chemnitz. We thank the Chemnitz University of Technology and the DFG for lending us these parts of the instruments. We want to thank prof. Gerlich for fruitful discussions.

This work was partly supported by the Czech Grant Agency under Contract no. P209/12/0233 and no. 205/09/1183 and by SV 267 302 and by GAUK 659112, GAUK 406011, GAUK 388811.

- [1] M. Čížek, J. Horáček, W. Domcke, *J. Phys. B: At. Mol. Opt. Phys.* 31 (1998) 2571–2583. doi:10.1088/0953-4075/31/11/018.
- [2] M. A. Smith, S. R. Leone, *J. Chem. Phys.* 78 (1983) 1325–1334. doi:10.1063/1.444870.
- [3] C. R. Claydon, G. A. Segal, H. S. Taylor, *J. Chem. Phys.* 54 (1971) 3799–3816. doi:10.1063/1.1675431.
- [4] H. J. Werner, U. Manz, P. Rosmus, *J. Chem. Phys.* 87 (1987) 2913–2918. doi:10.1063/1.453079.
- [5] D. J. Haxton, C. W. McCurdy, T. N. Rescigno, *Phys. Rev. A* 75 (2007) 012710. doi:10.1103/PhysRevA.75.012710.
- [6] R. Abouaf, R. Paineau, F. Fiquet-Fayard, *J. Phys. B: At. Mol. Opt. Phys.* 9 (1976) 303. doi:10.1088/0022-3700/9/2/017.
- [7] J. L. Mauer, G. J. Schulz, *Phys. Rev. A* 7 (1973) 593–605. doi:10.1103/PhysRevA.7.593.
- [8] V. A. Esaulov, R. L. Champion, J. P. Grouard, R. I. Hall, J. L. Montmagnon, F. Penet, *J. Chem. Phys.* 92 (1990) 2305–2309. doi:10.1063/1.457971.
- [9] S. T. Lee, J. M. Farrar, *J. Chem. Phys.* 111 (1999) 7348–7358. doi:10.1063/1.480057.
- [10] S. Živanov, M. Čížek, J. Horáček, M. Allan, *J. Phys. B: At. Mol. Opt. Phys.* 36 (2003) 3513. doi:10.1088/0953-4075/36/16/312.
- [11] S. C. Glover, D. W. Savin, A. Jappsen, *Astrophys. J.* 640 (2006) 553–568. doi:10.1086/500166.
- [12] O. Martinez, Z. Yang, N. B. Betts, T. P. Snow, V. M. Bierbaum, *Astrophys. J.* 705 (2009) L172. doi:10.1088/0004-637X/705/2/L172.
- [13] H. Kreckel, H. Bruhns, M. Čížek, S. C. O. Glover, K. A. Miller, X. Urbain, D. W. Savin, *Science* 329 (2010) 69–71. doi:10.1126/science.1187191.
- [14] D. Gerlich, P. Jusko, Š. Roučka, I. Zymak, R. Plašil, J. Glosík, *Astrophys. J.* 749 (2012) 22. doi:10.1088/0004-637X/749/1/22.
- [15] S. Beu, C. Hendrickson, A. Marshall, *J. Am. Soc. Mass Spectrom.* 22 (2011) 591–601. doi:10.1007/s13361-010-0057-9.
- [16] W. G. Rellergert, S. T. Sullivan, S. Kotochigova, A. Petrov, K. Chen, S. J. Schowalter, E. R. Hudson, *Phys. Rev. Lett.* 107 (2011) 243201. doi:10.1103/PhysRevLett.107.243201.
- [17] M. Moseler, B. Huber, H. Häkkinen, U. Landman, G. Wrigge, M. A. Hoffmann, B. v. Issendorff, *Phys. Rev. B* 68 (2003) 165413. doi:10.1103/PhysRevB.68.165413.
- [18] G. Beamson, H. Q. Porter, D. W. Turner, *J. Phys. E: Sci. Instrum.* 13 (1980) 64. doi:10.1088/0022-3735/13/1/018.
- [19] KATRIN collaboration, KATRIN Design Report 2004, Technical Report, NPI ASCR Řež, 2005. URL: <http://bibliothek.fzk.de/zb/berichte/FZKA7090.pdf>.
- [20] D. Gerlich, *Adv. Chem. Phys.* 82 (1992). doi:10.1002/9780470141397.ch1.
- [21] O. Chun-Sing, H. A. Schuessler, *J. Appl. Phys.* 52 (1981) 2601–2607. doi:10.1063/1.329069.
- [22] Y. Huang, G.-Z. Li, S. Guan, A. G. Marshall, *J. Am. Soc. Mass Spectrom.* 8 (1997) 962–969. doi:10.1016/S1044-0305(97)82945-5.
- [23] G. Li, *Commun. Theor. Phys.* 12 (1989) 355–366. URL: <http://ctp.itp.ac.cn/EN/abstract/abstract14551.shtml>.
- [24] I. Y. Dodin, N. J. Fisch, *J. Plasma Phys.* 71 (2005) 289–300. doi:10.1017/S0022377804003174.
- [25] I. Dodin, N. J. Fisch, *Phys. Lett. A* 349 (2006) 356–369. doi:10.1016/j.physleta.2005.09.049.
- [26] J. Glosík, A. Luca, S. Mark, D. Gerlich, *J. Chem. Phys.* 112 (2000) 7011–7021. doi:10.1063/1.481322.

- [27] A. Logg, G. N. Wells, *ACM Trans. Math. Soft.* 37 (2010) 20:1–20:28. doi:10.1145/1731022.1731030.
- [28] A. Logg, K. A. Mardal, G. N. Wells, et al., *Automated Solution of Differential Equations by the Finite Element Method*, Springer, 2012. doi:10.1007/978-3-642-23099-8.
- [29] T. W. Darling, F. Rossi, G. I. Opat, G. F. Moorhead, *Rev. Mod. Phys.* 64 (1992) 237–257. doi:10.1103/RevModPhys.64.237.
- [30] F. Rossi, G. I. Opat, *J. Phys. D: Appl. Phys.* 25 (1992) 1349. doi:10.1088/0022-3727/25/9/012.
- [31] P. Hlavenka, R. Otto, S. Trippel, J. Mikosch, M. Weidemuller, R. Wester, *J. Chem. Phys.* 130 (2009) 061105. doi:10.1063/1.3080809.
- [32] O. Asvany, S. Schlemmer, *Int. J. Mass Spectrom.* 279 (2009) 147 – 155. doi:10.1016/j.ijms.2008.10.022.
- [33] J. Bartmess, *NIST Chemistry WebBook*, NIST Standard Reference Database Number 69, National Institute of Standards and Technology, Gaithersburg MD, 20899, 2012. URL: <http://webbook.nist.gov>, retrieved May 28, 2012.
- [34] M. McFarland, D. L. Albritton, F. C. Fehsenfeld, E. E. Ferguson, A. L. Schmeltekopf, *J. Chem. Phys.* 59 (1973) 6629–6635. doi:10.1063/1.1680043.
- [35] L. B. Lucy, *Astrophys. J.* 79 (1974) 745. doi:10.1086/111605.
- [36] W. H. Richardson, *J. Opt. Soc. Am.* 62 (1972) 55–59. doi:10.1364/JOSA.62.000055.

COLOPHON

This document was typeset using L^AT_EX with the typographical look-and-feel `classicthesis`. Figures were created using the python programming language with the plotting library `matplotlib`:

<http://www.matplotlib.org/>

The text was written in ViM.

Printed June 19, 2013.